

**Influence of operating conditions on the aging of  
large-format lithium iron phosphate battery cells:  
From laboratory conditions to a home storage  
system**

Zur Erlangung des akademischen Grades eines  
DOKTORS DER INGENIEURWISSENSCHAFTEN (DR.-ING.)

von der KIT-Fakultät für Chemieingenieurwesen und Verfahrenstechnik des  
Karlsruher Instituts für Technologie (KIT)  
genehmigte

DISSERTATION

von  
M.Sc. Mehmet Can Yagci  
aus Beyoglu, Türkei

Tag der mündlichen Prüfung: 30.09.2024

Erstgutachter: Prof. Dr. Wolfgang G. Bessler

Zweitgutachter: Prof. Dr. Thomas Wetzel



## ACKNOWLEDGEMENTS

---

I would like to thank Prof. Dr. Wolfgang G. Bessler for giving me the opportunity to pursue my Ph.D. under his supervision. His guidance and support have always encouraged me throughout my doctoral studies. I learned a lot about science and beyond during our friendly discussions. I am grateful to Prof. Dr. Thomas Wetzels for accepting to be the second examiner of my Ph.D. thesis. I appreciate the positive communication each time I get in contact with him. I thank Prof. Dr. Dirk Velten for supporting my Ph.D. application.

All the experiments, data analysis, and writing of this thesis were performed at the Institute of Sustainable Energy Systems (INES) of Hochschule Offenburg. Specifically, I thank Pascale Müller for her help during microscopic measurements. I acknowledge the following agencies for funding the research projects that this study is based on: the German Ministry of Education and Research (BMBF), the European Regional Development Fund and the Land Baden-Württemberg. Our industrial project partners, ASD Automatic Storage Device and W-Quadrat, are greatly acknowledged for their support.

It was a pleasure to work at the INES throughout this Ph.D. study. I must thank my colleagues, Prof. Dr. Michael Schmidt, Elmar Bollin, Thomas Feldmann, and Michael Wirwitzki, for their valuable support during microgrid aging tests. I would also like to express my gratitude to my friends in the AG Bessler research group. They all contributed to the friendly atmosphere I was happy to work in. Especially for their essential contributions to this thesis, I must thank David Schmider for the German version of the abstract, René Behmann for performing aging tests, Viktor Daubert for cell opening, and Jonas Braun and Oliver Richter for degradation modes analysis. I acknowledge Manik Mayur, Serena Carelli, and Michael Quarti for our joint publications.

Finally, I would like to express my heartfelt thanks to my family: to Joachim Merih for patiently waiting for his father to “*écrire son livre*” and making my life colorful in the process, and to Ségolène for her infinite support and understanding, none of this would be possible without her.

“All that is gold does not glitter,  
Not all those who wander are lost;  
The old that is strong does not wither,  
Deep roots are not reached by the frost.”

—J. R. R. Tolkien, *The Fellowship of the Ring*

# ABSTRACT

---

The installed energy capacity of renewable energy generation systems is increasing globally due to the implementation of decarbonization policies. Due to the unpredictable nature of renewable energy sources, there is frequently a mismatch between load demand and energy supply. Stationary energy storage systems act as a buffer that stores excessive energy to balance future energy shortcomings. For residential applications, battery energy storage systems (BESS) are an attractive solution to realize the self-sufficiency of a household equipped with photovoltaics. Despite the decrease in prices, battery costs are still the most significant part of the investment cost of battery energy storage systems. Therefore, estimating battery lifetime and developing operation strategies to hinder aging is essential for improving the feasibility of BESS.

Lithium iron phosphate (LFP) lithium-ion batteries are widely used for residential BESS because of their low cost, long life, and safety. Despite extensive research in the laboratory of small-capacity cells, there are few full-scale field investigations on the lifetime and aging characteristics of commercial BESS equipped with LFP cells. This Ph.D. thesis investigates the realistic aging behavior of a residential-scale BESS equipped with large-format (180 Ah) LFP cells. We aim to create and implement a method to investigate the practical aging on cell, stack, and system levels. The experimental data is also processed by degradation modes analysis to identify the underlying mechanisms of capacity loss.

Each cell underwent primarily detailed electrical characterization, which consists of measuring characteristic charge/discharge curves and internal resistances at different current rates and temperatures. After electrical characterization, exemplary cells were opened in an inert atmosphere glove-box for structural investigation, consisting of size and weight measurements of cell components. The morphology and chemical composition of electrode samples from opened cells were investigated with light microscopy (LM) and scanning electron microscopy (SEM). The results of the detailed initial characterization of single cells were used to create a complete and self-consistent parameter set for each cell. The initial dataset was also used to compare periodical performance test results with the initial aging state of single cells throughout aging experiments.

The realistic aging experiment was carried out by investigating for 1000 days the changes in aging indicators of two commercial, residential scale BESS integrated into a microgrid. The battery stacks of both systems were built with LFP cells from the same batch of detailed characterization cells but installed with different (serial and parallel) configurations. Thus,

we could investigate the effect of stack architecture on aging comparatively. At the end of the measurements, it was observed that no stack architecture is superior to another despite different operating voltages and current levels. In parallel, two LFP cells (identical to the battery stack cells) were tested at constant ambient temperature (20 °C) with continuous complete charge/discharge cycles at a constant current higher than the maximum current exhibited by BESS cells. Regarding capacity retention by equivalent full cycles, both cells outperformed BESS stacks. The comparative cell, stack, and system-level aging investigations indicate that good thermal management can provide a better lifetime even under harsher operating conditions.

The individual effects of temperature and load profile on aging were investigated via single-cell experiments in controlled ambient temperature. For this purpose, six test groups of single cells were tested to represent three realistic aging scenarios (continuous cycling, fully charged storage, and partially charged storage) at two different ambient temperatures (35 °C and 50 °C). All cells tested at 50 °C aged faster than those tested at 35 °C according to periodical performance diagnostics. Continuous cycling increased capacity loss among the cells tested at the same ambient temperature compared to fully or partially charged storage.

Single-cell experiment data was analyzed using degradation mode analysis algorithms. The results demonstrate that the loss of lithium inventory, attributed to the irreversible loss of lithium due to continuous growth of the solid electrolyte interface (SEI) layer, is the primary aging mode in all cases.

# KURZFASSUNG

---

Die installierte Energiekapazität erneuerbarer Energieerzeugungssysteme nimmt weltweit zu aufgrund der Umsetzung von Dekarbonisierungsmaßnahmen. Infolge der Unbeständigkeit der erneuerbaren Energiequellen kommt es häufig zu einem Ungleichgewicht zwischen Lastnachfrage und Energieangebot. Stationäre Energiespeichersysteme dienen als Puffer, um überschüssige Energie zu speichern und somit eventuelle Energiedefizite auszugleichen. Für private Anwendungen sind Batteriespeichersysteme (BESS) eine attraktive Lösung, um die Autarkie eines mit Photovoltaik ausgestatteten Haushalts zu erreichen. Trotz des Preisrückgangs machen die Batteriekosten jedoch immer noch den größten Teil der Investitionskosten für BESS aus. Daher sind die Abschätzung der Batterielebensdauer und die Entwicklung von Betriebsstrategien zur Verhinderung von Alterungsprozessen von entscheidender Bedeutung für die Verbesserung der Wirtschaftlichkeit von BESS.

Lithium-Eisenphosphat (LFP) Lithium-Ionen-Batterien werden aufgrund ihrer geringen Kosten, langen Lebensdauer und Sicherheit häufig für BESS in Privathaushalten verwendet. Während zahlreiche Forschungsarbeiten mit Zellen geringer Kapazität im Labor durchgeführt werden, gibt es nur wenige groß angelegte Untersuchungen zur Lebensdauer und den Alterungseigenschaften kommerzieller BESS mit LFP-Zellen. Diese Doktorarbeit untersucht das realitätsnahe Alterungsverhalten eines haushaltsüblichen BESS, das mit großformatigen (180 Ah) LFP-Zellen ausgestattet ist. Ziel ist es, eine Methode zu entwickeln und zu implementieren, mit der die Alterung auf Zell-, Stack- und Systemebene untersucht werden kann. Die experimentellen Daten werden außerdem im Hinblick auf Degradationsmodi analysiert, um die zugrundeliegenden Mechanismen des Kapazitätsverlustes zu identifizieren.

Jede Zelle wurde zunächst einer detaillierten elektrischen Charakterisierung unterzogen, die aus der Messung der charakteristischen Lade-/Entladekurven und der Innenwiderstände bei unterschiedlichen Stromstärken und Temperaturen bestand. Im Anschluss an die elektrische Charakterisierung wurden einige exemplarische Zellen in einer Glovebox unter Inertgasatmosphäre geöffnet, um ihre Struktur zu untersuchen, wobei Größe und Gewicht der Zellkomponenten gemessen wurden. Die Morphologie und die chemische Zusammensetzung von Elektrodenproben aus den geöffneten Zellen wurden mittels Lichtmikroskopie und Rasterelektronenmikroskopie untersucht. Die Ergebnisse der detaillierten initialen Charakterisierung der Einzelzellen wurden zur Erstellung eines vollständigen und konsistenten Parametersatzes für jede Zelle verwendet. Der Referenzdatensatz wurde außerdem für den Vergleich der Ergebnisse periodisch

durchgeführter Performancetests mit dem anfänglichen Alterungszustand der Einzelzellen während der Alterungsexperimente verwendet.

Das realitätsnahe Alterungsexperiment wurde durchgeführt, indem über einen Zeitraum von 1000 Tagen die Veränderungen der Alterungsindikatoren zweier kommerzieller, haushaltsüblicher BESS untersucht wurden, die in ein Microgrid integriert waren. Die Batteriestacks beider Systeme bestanden aus LFP-Zellen aus derselben Charge von Zellen, die der beschriebenen detaillierten Charakterisierung unterzogen wurden. Allerdings wurden sie in unterschiedlichen Konfigurationen (seriell und parallel) aufgebaut. Durch diesen Vergleich konnten Auswirkungen der Systemarchitektur auf die Alterung untersucht werden. Trotz unterschiedlicher Betriebsspannungen und Stromstärken konnte jedoch am Ende der Messungen keine vorteilhafte Systemarchitektur festgestellt werden. Zusätzlich wurden zwei LFP-Zellen (identisch mit den Batteriestack-Zellen) bei konstanter Umgebungstemperatur (20 °C) mit kontinuierlichen vollständigen Lade-/Entladezyklen mit konstantem Strom getestet, der höher als der maximal auftretende Strom der BESS-Zellen war. Hinsichtlich des Kapazitätserhalts bezogen auf äquivalente Vollzyklen übertrafen beide Zellen die BESS-Stacks. Die vergleichenden Alterungsuntersuchungen auf Zell-, Stack- und Systemlevel zeigen, dass ein gutes Wärmemanagement auch unter härteren Betriebsbedingungen zu einer längeren Lebensdauer führen kann.

Die individuellen Auswirkungen von Temperatur und Lastprofil auf die Alterung wurden anhand von Einzelzellenversuchen bei kontrollierter Umgebungstemperatur untersucht. Zu diesem Zweck wurden sechs Testgruppen von Einzelzellen bei zwei verschiedenen Umgebungstemperaturen (35 °C und 50 °C) getestet, um drei realistische Alterungsszenarien zu repräsentieren (kontinuierliches Zyklieren, vollständig geladene Lagerung und teilweise geladene Lagerung). Alle bei 50 °C getesteten Zellen alterten schneller als die bei 35 °C getesteten Zellen, wie die periodische Leistungsdiagnose ergab. Bei gleichen Umgebungstemperaturen erhöhte kontinuierliches Zyklieren den Kapazitätsverlust im Vergleich zur Lagerung mit vollständiger oder teilweiser Ladung.

Die Daten aus den Einzelzellexperimenten wurden mithilfe von Algorithmen zur Analyse der Degradationsmodi analysiert. Die Ergebnisse zeigen, dass der Verlust an zyklierbaren Lithium-Ionen (LLI), der auf den irreversiblen Verlust von Lithium aufgrund des kontinuierlichen Wachstums der passiven Grenzschicht (SEI) zurückzuführen ist, in allen Fällen der wichtigste Alterungsmodus ist.



# CONTENTS

---

Abbreviations .....	x
List of symbols .....	xii
1 Introduction .....	1
2 Background .....	5
2.1 Residential battery energy storage systems .....	5
2.1.1 Lithium-ion batteries .....	5
2.1.2 Battery stacks .....	6
2.2 Lithium Iron Phosphate (LFP) Lithium-ion batteries .....	7
2.2.1 Definition .....	7
2.2.2 Structure .....	8
2.2.3 Working principle .....	9
2.2.4 Power rating .....	10
2.2.5 Energy density .....	11
2.2.6 Temperature performance .....	11
2.2.7 Safety and sustainability .....	11
2.3 LFP lithium-ion batteries aging .....	12
2.3.1 Investigation method .....	12
2.3.2 Aging indicators .....	13
2.3.3 Operating conditions .....	14
2.3.4 Aging mechanisms and degradation modes .....	16
2.3.5 Computational analysis of degradation modes .....	19
3 Methodology .....	21
3.1 Definition of test parameters .....	21
3.2 Test batteries .....	24
3.3 Experimental procedure .....	27
3.4 Characterization .....	28
3.4.1 Electrical characterization .....	28

3.4.2	Structural characterization .....	36
3.5	Battery energy storage system aging tests with Sinopoly cells .....	38
3.5.1	Aging of commercial LFP cells in microgrid operation.....	38
3.5.2	Continuous temperature-controlled cycling.....	43
3.6	Single-cell calendaric and cyclic aging tests with Calb cells.....	44
3.6.1	Experimental setup.....	44
3.6.2	Periodic reference performance tests (checkups).....	46
3.7	Analysis of degradation modes .....	47
3.7.1	Electrode balances .....	47
3.7.2	Calculation of degradation modes.....	49
4	Results and Discussion .....	54
4.1	Electrical and structural characterization .....	54
4.1.1	Electrical characterization.....	55
4.1.2	Structural characterization .....	60
4.1.3	Electrode balances .....	69
4.1.4	Summary .....	73
4.2	Aging characteristics of commercial battery energy storage systems with serial and parallel cell configurations .....	73
4.2.1	Initial characterization and cell selection .....	74
4.2.2	Microgrid operation .....	76
4.2.3	Comparison of checkup results.....	78
4.2.4	Comparison of microgrid operation with temperature-controlled cycling .....	82
4.2.5	Discussion.....	84
4.2.6	Summary .....	88
4.3	Calendaric and cyclic aging characteristics of single cells .....	88
4.3.1	Initial characterization.....	89
4.3.2	Cyclic aging.....	90
4.3.3	Calendaric aging.....	94
4.3.4	Degradation modes analysis.....	97

4.3.5	Discussion.....	106
4.3.6	Summary.....	108
5	Summary and outlook.....	110
5.1	Summary.....	110
5.1.1	Detailed initial characterization.....	110
5.1.2	Residential BESS aging.....	111
5.1.3	Single-cell calendaric and cyclic aging.....	112
5.2	Conclusion.....	113
5.3	Outlook.....	115
6	Appendices.....	116
6.1	Own publications.....	116
6.1.1	Journal Articles.....	116
6.1.2	Conferences.....	116
6.2	Battery data sheets and documentation.....	117
6.2.1	Sinopoly product brochure.....	118
6.2.2	Sinopoly cell datasheet.....	120
6.2.3	Sinopoly MSDS.....	127
6.2.4	Calb cell datasheet.....	129
6.2.5	Calb cell MSDS.....	136
7	References.....	138

## ABBREVIATIONS

---

AC	Alternating current
AM	Active material
BESS	Battery energy storage system
BMBF	German Ministry of Education and Research
BMS	Battery management system
CC	Constant current
CO <sub>2</sub>	Carbon dioxide
CP	Constant power
CV	Constant voltage
DC	Direct current
DEC	Diethyl carbonate
DMC	Dimethyl carbonate
DOD	Depth of discharge
DVA	Differential voltage analysis
EC	Ethylene carbonate
EDX	Energy dispersive X-Ray
EFC	Cumulated equivalent full cycles
EIS	Electrochemical impedance spectrum
EV	Electric vehicle
EVS	Electrochemical voltage spectroscopies
ICA	Incremental capacity analysis
INES	Institute of Sustainable Energy Systems
IR	Internal resistance
IR <sub>cycle,CC</sub>	Internal resistance calculated by CC cyclic average method
IR <sub>cycle,full</sub>	Internal resistance calculated by full cyclic average method
IR <sub>pulse</sub>	Internal resistance calculated by pulse measurement method
L1	First stack of parallel architecture BESS
L2	Second stack of parallel architecture BESS
LAM	Loss of active material
LAM <sub>NE</sub>	Loss of active material of the negative electrode
LAM <sub>PE</sub>	Loss of active material of the positive electrode

LCO	Lithium Cobalt Oxide
LFP	Lithium iron phosphate
LIB	Lithium-ion battery
LiFePO <sub>4</sub>	Lithium iron phosphate
LiPF <sub>6</sub>	Lithium hexafluorophosphate
LLI	Loss of lithium inventory
LM	Light microscopy
LMO	Lithium Manganese Oxide
MPC	Model-predictive controller
MSDS	Material safety datasheet
NCA	Lithium Nickel Cobalt Aluminum Oxide
NE	Negative electrode
NiCd	Nickel-cadmium
NiMH	Nickel-metal hydride
NMC	Lithium Nickel Manganese Cobalt Oxide
OCV	Open circuit voltage
OECD	Organisation for Economic Co-operation and Development
PE	Positive electrode
PLC	Programmable logic controller
pOCV	Pseudo-open circuit voltage
PP	Polypropylene
PTC	Positive temperature coefficient
PV	Photovoltaics
SEI	Solid electrolyte interface
SEM	Scanning electron microscopy
SOC	State of charge
SOH	State of health

## LIST OF SYMBOLS

---

Symbol	Unit	Meaning
$A_e$	$m^2$	Active electrode area
$C^A$	$mAh/cm^2$	Usable electrode capacity
$C_{AM}^A$	$mAh/cm^2$	Areal capacity
$C_{cell}$	Ah	Full-cell capacity calculated from electrode balances analysis
$C_N$	Ah	Nominal capacity
$C_{NE}$	Ah	Theoretical negative electrode capacity
$C_0$	Ah	Initial (checkup #0) discharge capacity
$C_{PE}$	Ah	Theoretical positive electrode capacity
$C_R$	Ah	Actual capacity
$c(Li)$	$mol/m^3$	Actual lithium concentration
$c_{max}(Li)$	$mol/m^3$	Maximum lithium concentration
$d_e$	m	Electrode thickness
$E_{charge}$	Wh	Charge energy
$E_{discharge}$	Wh	Discharge energy
$I$	A	Electric current
$I(t_0)$	A	Current measured at $t_0$
$I(t_1)$	A	Current measured at $t_1$
$I_{CC}$	A	CC phase current
$\bar{I}_{chg}$	A	Average full charge current
$\bar{I}_{dis}$	A	Average full discharge current
$m_{AM}$	mg	Total active material mass
$m_{AM}^A$	$mg/cm^2$	Area-specific active material loading
$N_{cell}$	1	Number of cells in the stack
$P_{dis}$	W	Discharge power
$Q$	As	Charge throughput
$\dot{Q}$	W	Heating power
$Q_{cell}(t)$	Ah	Total charge throughput of the cell until time $t$
$Q_{charge}$	Ah	Charge throughput during charge
$Q_{discharge}$	Ah	Charge throughput during discharge

<b>Symbol</b>	<b>Unit</b>	<b>Meaning</b>
$Q_{LAM,PE}$	Ah	Loss of active material charge content at the positive electrode
$Q_{LAM,NE}$	Ah	Loss of active material charge content at the neg. electrode
$Q_{LLI}$	Ah	Loss of lithium inventory charge content
$Q_{NE}$	Ah	Charge content of the negative electrode
$Q_{PE}$	Ah	Charge content of the positive electrode
$T_{ambient}$	°C	Ambient temperature
$T_{cell}$	°C	Cell temperature
$t_{dis}$	s	Discharge time
$t_{pulse}$	s	Current pulse time
$t_{rest}$	min	Rest time
$V$	V	Voltage
$V(t_0)$	V	Voltage measured at $t_0$
$V(t_1)$	V	Voltage measured at $t_1$
$V_{AM}$	m <sup>3</sup>	Total volume of active material
$V_{cell}$	V	Cell voltage
$V_{cell}^{eq}$	V	Full-cell pseudo-open circuit voltage
$V_e$	m <sup>3</sup>	Electrode volume
$V^{eq}$	V	Equilibrium voltage
$V_N$	V	Nominal cell voltage
$V_{NE}^{eq}$	V	Negative electrode half-cell potential
$V_{PE}^{eq}$	V	Positive electrode half-cell potential
$\bar{V}_{chg}$	V	Average full charge voltage
$\bar{V}_{chg}$	V	Average full charge voltage
$\bar{V}_{chg[10-90\%]}$	V	Average charge voltage between 10% and 90% SOC
$\bar{V}_{dis}$	V	Average full discharge voltage
$\bar{V}_{dis}$	V	Average full discharge voltage
$\bar{V}_{dis[10-90\%]}$	V	Average discharge voltage between 10% and 90% SOC
$X_{NE}$	1	Negative electrode half-cell lithium stoichiometry
$X_{NE}^{max}$	1	Maximum negative electrode half-cell lithium stoichiometry
$X_{NE}^{min}$	1	Minimum negative electrode half-cell lithium stoichiometry
$X_{PE}$	1	Positive electrode half-cell lithium stoichiometry

<b>Symbol</b>	<b>Unit</b>	<b>Meaning</b>
$X_{PE}^{\max}$	1	Maximum positive electrode half-cell lithium stoichiometry
$X_{PE}^{\min}$	1	Minimum positive electrode half-cell lithium stoichiometry
$\Delta X_{Li}$	1	Lithium stoichiometry range during cycling
$\varepsilon_{AM}$	1	Volume fraction of active material
$\eta$	V	Overpotential
$\eta_{\text{energy}}$	1	Energy efficiency
$\rho_{AM}$	kg/m <sup>3</sup>	Active material density



# 1 INTRODUCTION

---

Climate change is an urgent and catastrophic threat to humans and nature. Worldwide reduction of greenhouse gas emissions must be accelerated to avoid irreversible ecological damage. For this purpose, the Paris Agreement was signed in 2015 by 196 countries at the United Nations Climate Change Conference to limit the global temperature increase to 1.5 °C above pre-industrial levels [1]. According to the Intergovernmental Panel on Climate Change Report 2018, the 1.5 °C target is achievable if global carbon dioxide (CO<sub>2</sub>) emissions reach net zero in 2055 [2].

In 2019, residential energy consumption accounted for 11 % of global CO<sub>2</sub> emissions [3]. Thus, the generation of carbon-free energy in households is a significant contribution to limiting global warming. Harvesting solar energy by using photovoltaic (PV) panels is the most popular carbon-free residential electricity generation technology. Between 2015 and 2022, the installed global capacity of residential solar PV power increased 400 % from 38.9 GW to 195.2 GW [4]. Contrary to the energy generated from fossil fuels, renewable energy sources suffer from supply-demand mismatch. Particularly for residential systems, the demand is relatively higher in the mornings and evenings when power output is relatively lower. As a result, battery energy storage systems (BESS) have become an indispensable element of household renewable energy generation for improving self-sufficiency.

Germany is the largest residential solar PV and battery market, with a consistent increase in installed capacity [5]. In 2022, the annual installed residential energy storage capacity was 52 % higher than in 2021. Lithium-ion batteries (LIB) are the dominant battery type, with a 98 % share of the new installations [6]. By 2040, stationary storage requirements are expected to rise to almost 3 TWh, owing to the rapid increase in renewable energy sources [7].

Globally, despite a consistent annual increase in unit installations, only 17 % of households installed BESS from a potential of 64 % of households with adequate technical infrastructure, according to a 2022 survey in Organisation for Economic Co-operation and Development (OECD) countries [3]. According to the respondents, affordability is the main reason for not installing a BESS.

Between 2013 and 2020, the cost of stationary lithium-ion battery systems reduced drastically by 50 % [8], mainly due to the decreasing single battery cell prices [8,9]. However, battery cells remain the most expensive element of residential BESS [10].

The financial feasibility analysis of BESS investments is based on the estimated lifetime of battery cells. Therefore, accurate estimation of battery lifetime is essential for precise feasibility analysis. Moreover, identification of the effects of operational conditions such as temperature, voltage, and current on battery lifetime can be used to develop technical strategies to prolong the lifetime of the BESS, which in return will make the BESS more affordable. In this thesis, our motivation is to identify aging indicators and the influence of operating conditions on the aging of a commercial BESS.

Residential BESS generally consists of a battery stack, an inverter to regulate voltage, and a battery management system (BMS) to control the operation and ensure the safety of batteries. The systems are typically constructed modularly, consisting of battery modules with multiple battery cells connected in series or parallel [11]. LIB became the standard BESS cell type due to continuously decreasing cell prizes and growing energy densities [12].

Photovoltaic home-storage systems have typical energy capacities of 5–15 kWh. Lithium-ion batteries with graphite negative electrodes and  $\text{LiFePO}_4$  (lithium iron phosphate) positive electrodes are widely used as battery cells in domestic PV systems due to relative cost advantage, high cyclic lifetime, and safety compared to chemistries like nickel manganese cobalt oxide (NMC) [13–15]. Despite widespread application, one of the leading technical challenges of using lithium iron phosphate (LFP) lithium-ion batteries (from now on referred to as “LFP cell”) for stationary BESS is the uncertain lifetime. Additionally, knowing and understanding the performance characteristics of single cells in terms of electrical, thermal, and aging properties is of utmost importance for designing and operating reliable and long-living systems. These characteristics are often not well known to the system manufacturer, as the cells are typically provided by external suppliers, with only limited information from data sheets. Moreover, even the manufacturers have had no field test data for over ten years because this technology was not commercially available before 2013.

In the literature, there have been many studies on LFP cell aging at the single-cell level [16–22]. Data for different cell types (chemistries and cell geometries) and cycling conditions (temperature, C-rate) are available. The main conclusion of these studies is that aging is a highly complex and nonlinear phenomenon, depending strongly on the operation conditions, mainly temperature, cycle depth, current rate, and resting times between operations [23–26]. Physicochemical models have been used to support understanding the origins of this behavior [27–29]. However, the typical energy capacities of residential BESS are 5–15 kWh, constructed usually with cells with a nominal capacity higher than 100 Ah. The published literature on such large-format cells is limited. The terms “large cell” or “large-format cell” are

used inconsistently in literature, recent studies including comparatively small cell capacities of 9 Ah [30], 10 Ah [31], 20 Ah [32], 25 Ah [33] or around 50 Ah [34–36]. There is very little literature available on cells with capacities beyond 100 Ah. Li et al. [37] presented the fabrication and testing of 100 Ah pouch LFP cells. Bacci et al. [38] performed cycling tests with 100 Ah LFP cells and compared the results with existing capacity fade models. Panchal et al. [39] measured the aging characteristics of 200 Ah LFP/graphite cells used for an electric vehicle. Empirical studies of LFP cell aging as a part of a battery stack are scarce and usually refer only to systems consisting of a single cell or several cells representing only a portion of the capacity of residential BESS [40,41]. To our knowledge, empirical aging data of commercial LFP cells operating on a full-scale commercial residential BESS has not yet been presented in the literature.

The goal of this Ph.D. thesis is to investigate the aging behavior of a commercially available residential BESS on the cell level (single prismatic LFP cell), the stack level (commercial battery systems consisting of multiple cells, inverters, BMS, and housing), and the system level (local grid with battery, photovoltaic panels, controllable sinks, and grid connection) to provide comprehensive insight. For this purpose, the investigation of the aging behavior of commercial large-format (180 Ah) LFP cells from two different Chinese manufacturers, Shenzhen Sinopoly Battery Co. Ltd. and China Aviation Lithium Battery Co. Ltd. (from now on referred to as “Sinopoly cell” and “Calb cell” for brevity) was performed in three different stages.

The first stage consists of detailed electrical and structural characterization of cell properties [42]. The structural properties of all cell components, such as electrodes, current collectors, and separators, were identified by opening exemplary cells and measuring cell geometry. In the following, the determination of cell chemistry and electrode morphology was investigated by microscopic techniques. Finally, rate capability tests and internal resistance (IR) measurements were performed at three different temperatures to characterize electrical properties. As a result, complete and self-consistent sets of cell parameters were derived for both commercial LFP cells.

In the second stage, the aging of Sinopoly cells was monitored during 2.5 years of operation as part of two commercial stationary electrical energy storage systems integrated into a microgrid. The aim of microgrid operation is to investigate cell and battery aging under realistic but well-controlled operating conditions. The analysis of the microgrid operation aging data demonstrated that temperature, rather than cycle number, has a dominating effect on accelerating capacity loss [43].

Following the microgrid aging step results, the final stage was designed to compare the individual effects of calendaric and cyclic aging periods on overall aging at different temperatures. For this purpose, Calb cells were tested at two controlled ambient temperatures (35 °C and 50 °C) undergoing continuous charge/discharge cycles (cyclic aging) or under no load (calendaric aging). In parallel to microgrid operation, high operating temperatures accelerate capacity loss, independent of load profile.

Moreover, the comparative aging test data was analyzed using aging algorithms to analyze the underlying aging mechanisms. The synthetic approach introduced by Dubarry et al. was used for the aging models [44,45]. The results of the aging mode analysis hint that the irreversible loss of cyclable lithium inventory is mainly responsible for capacity loss during aging.

The background information on stationary battery energy storage systems, lithium-ion batteries, lithium iron phosphate lithium-ion batteries, and an outlook on their aging are given in Section 2. The properties of test batteries, experimental setup, test procedures, and data analysis methods are presented in Section 3. The results and discussion are presented in Section 4 under three subchapters corresponding to three investigation stages on initial electrical and structural characterization, microgrid operation, and comparative aging. Finally, the summary of the results and an outlook are given in Section 5.

## 2 BACKGROUND

### 2.1 RESIDENTIAL BATTERY ENERGY STORAGE SYSTEMS

#### 2.1.1 Lithium-ion batteries

Batteries are the most widespread commercial form of electrical energy storage. Because of the various applications such as consumer electronics, power tools, electric vehicles (EV), and stationary storage, batteries have become one of the indispensable technologies of the present day. Figure 1 shows the global battery market size for every five years between 2000-2030. The global battery market has grown annually by 8 % on average between 2010-2020 [46]. The secondary (rechargeable) battery market consists of four main types of batteries: lead-acid, nickel-cadmium (NiCd), nickel-metal hydride (NiMH), and lithium-ion. Lead-acid batteries have the highest market share by 2020 among the battery types. However, lithium-ion batteries are the fastest-growing technology and are expected to have the highest market share in value (estimated 40 billion USD) by 2025.

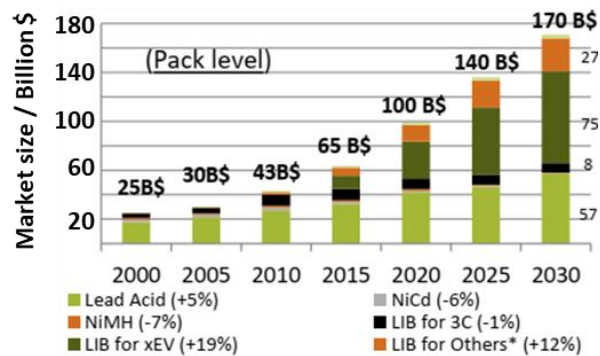


Figure 1: Battery market size between 2000 – 2030 (estimations for 2025, 2030) in billion US dollars by battery type and application. xEV: electric vehicles, 3C: computer, communication, consumer electronics. The percentages in parentheses next to the data labels represent the estimated market size increase between 2025 and 2030. Source: C. Pillot, *The Rechargeable Battery Market and Main Trends 2018-2030*, Avicenne Energy, Lyon, France, 2019 [46].

Lithium-ion batteries have revolutionized portable consumer electronics since their first commercial introduction at the beginning of the 1990s. Ergonomic mobile phones, lightweight laptops, and pocket-size MP3 players emerged into the market because LIBs doubled the energy density (up to 240 Wh/kg) and specific energy (up to 640 Wh/L) of the

state-of-the-art technology of its time [47–50]. Besides high energy density, lithium-ion batteries provide advantages such as low self-discharge rate (2 % to 8 % per month), no memory effect, and deep depth of discharge (DOD) capability compared to other battery technologies. On the other hand, lithium-ion batteries are relatively expensive, inefficient at low temperatures, and can exhibit safety problems like thermal runaway [50,51].

In Figure 1, the highest annual market value growth rate (>12 %) is estimated for lithium-ion battery applications such as forklifts, UPS, medical devices, and residential BESS [46]. The contribution of stationary storage lithium-ion batteries to this rapid growth projection cannot be ignored. Lithium-ion batteries are the most performant and long-lasting battery type for relatively small-scale and short-term residential BESS [52]. Lithium-ion batteries dominated the residential BESS market when the price of high specific energy lithium-ion battery packs became price-competitive compared to existing secondary battery technologies [6].

### **2.1.2 Battery stacks**

Technically, the primary function of the residential BESS is to buffer the energy supply and demand asymmetry of residential renewable energy generation systems such as PV panels. Depending on system design, they can passively store excessive energy or operate according to optimization algorithms depending on provisioned future supply-demand profiles [53]. The commercial residential BESS consists of three main blocks: inverter, battery management system (BMS), and battery stack. In this Ph.D. thesis, we focus on the aging performance of the battery stack and single cells as its building blocks. Thus, inverter and BMS's contributions to aging are left out of our scope.

The battery stack is constructed by installation of single cells according to a cell configuration fitting to design needs such as storage capacity, output voltage, maximum current rating, and power output. Cell configuration refers to the connection of cells within the battery stack according to serial or parallel arrangements. Both serial configurations and parallel configurations have strengths and weaknesses. They are summarized in Table 1 and discussed in the following.

Today, the general tendency is to use serial cell configurations to increase the voltage to a level well-suited for DC/AC inverters (for grid-coupled applications) or high-voltage DC systems (for battery electric vehicles). In the case of serial cell configuration, cell-to-cell capacity variations can influence the overall stack performance. The cell with the lowest capacity and/or highest IR can dominate the overall stack behavior by reaching the end of charge or discharge cut-off voltage earlier than the other cells. In order to avoid this problem,

elaborate cell balancing strategies are required, which add cost and complexity to the battery. Even then, the weakest cell is forced into deeper cycles than the other cells, accelerating aging.

Parallel cell configuration has a significant advantage for using unbalanced cells in the same stack. Cell balancing occurs passively as electrical energy is transferred from cell to cell via the parallel connection. Therefore, this configuration is robust to cell-to-cell capacity variations, and there is no need for active cell-balancing components. Thus, it can be expected that cell cost can be reduced by enabling the usage of cells of different batches or histories together. However, higher ohmic losses occur due to high current through all components (e.g., cables, connectors, sensors, switches), which may increase the overall material cost of the battery. Also, additional safety devices may be needed to rule out possible risks that high passive balancing currents between inhomogeneously charged cells can cause.

Table 1: Properties of serial and parallel cell configurations.

	<b>Serial cell configuration</b>	<b>Parallel cell configuration</b>
Voltage	<ul style="list-style-type: none"> <li>• High voltage</li> </ul>	<ul style="list-style-type: none"> <li>• Low voltage</li> </ul>
Current	<ul style="list-style-type: none"> <li>• Low current</li> </ul>	<ul style="list-style-type: none"> <li>• High current</li> </ul>
Advantages	<ul style="list-style-type: none"> <li>+ Low ohmic losses</li> <li>+ Cheaper circuit components</li> </ul>	<ul style="list-style-type: none"> <li>+ Passive self-balancing</li> <li>+ Robust towards cell variations</li> </ul>
Disadvantages	<ul style="list-style-type: none"> <li>– Active balancing required</li> <li>– Performance prone to single-cell failures</li> </ul>	<ul style="list-style-type: none"> <li>– High ohmic losses</li> <li>– High-current components required</li> </ul>

## 2.2 LITHIUM IRON PHOSPHATE (LFP) LITHIUM-ION BATTERIES

### 2.2.1 Definition

Commercial lithium-ion batteries are generally categorized by their positive electrode (PE) active material: lithium nickel manganese cobalt oxide (NMC), lithium nickel cobalt aluminum oxide (NCA), lithium iron phosphate (LFP), lithium cobalt oxide (LCO), lithium manganese oxide (LMO). For stationary storage applications, LFP is the fastest-growing cell chemistry and is forecasted to overtake NMC as the leader in market share by 2030 [54]. In this Ph.D. thesis, we investigate the aging properties of two large-format 180 Ah commercial LFP batteries commonly used in stationary storage systems.

LFP batteries are considered state-of-the-art commercial lithium-ion battery technology because they ensure high safety standards while still providing high-power capability, flat discharge voltage profile, and sufficiently high specific capacity at low cost (due to the absence of valuable elements like cobalt). On the other hand, LFP batteries also have limitations such as low nominal voltage, low electrical and ionic conductivity, and low capacity density [13,48,49,55,56]. The following sections present the structure, working principle, operational performance, and aging properties of LFP batteries to establish the theoretical background of this Ph.D. thesis.

### **2.2.2 Structure**

In lithium-ion batteries, lithium exists in the cell as  $\text{Li}^+$  ion. The presence of ionic lithium is favorable in terms of safety compared to predecessor pure lithium containing Li-metal batteries, where dendrite formation limits lifetime drastically. Following this modification, transition metal oxides were proposed as PE materials that promise high open circuit cell voltages (*e.g.*, greater than 4 V for LCO), reversible removal/insertion of  $\text{Li}^+$  ion, and stability at room temperature [57]. In 1997, phospho-olivine  $\text{LiFePO}_4$  was introduced by Padhi et al. [58] as a PE material candidate for rechargeable lithium-ion batteries.

The negative electrode (NE) of present-day lithium-ion batteries does not consist of pure Li metal except in some niche applications. Instead, graphite is usually used as an NE active material in commercial LFP batteries. Therefore, in contrast to Li-metal batteries, the source of lithium ions is PE active material  $\text{LiFePO}_4$ . Thus, LFP batteries are manufactured with fully lithiated PE (discharged state). The  $\text{Li}^+$  conducting electrolyte is, in general, prepared by solutions of lithium hexafluorophosphate ( $\text{LiPF}_6$ ) salt in carbonate solvent blends (*e.g.*, ethylene carbonate (EC), dimethyl carbonate (DMC), and diethyl carbonate (DEC)). The porous polymer separators are responsible for separating two electrode compartments from each other to provide stability and safety for the cell by preventing internal short circuits while not interrupting ion flow.



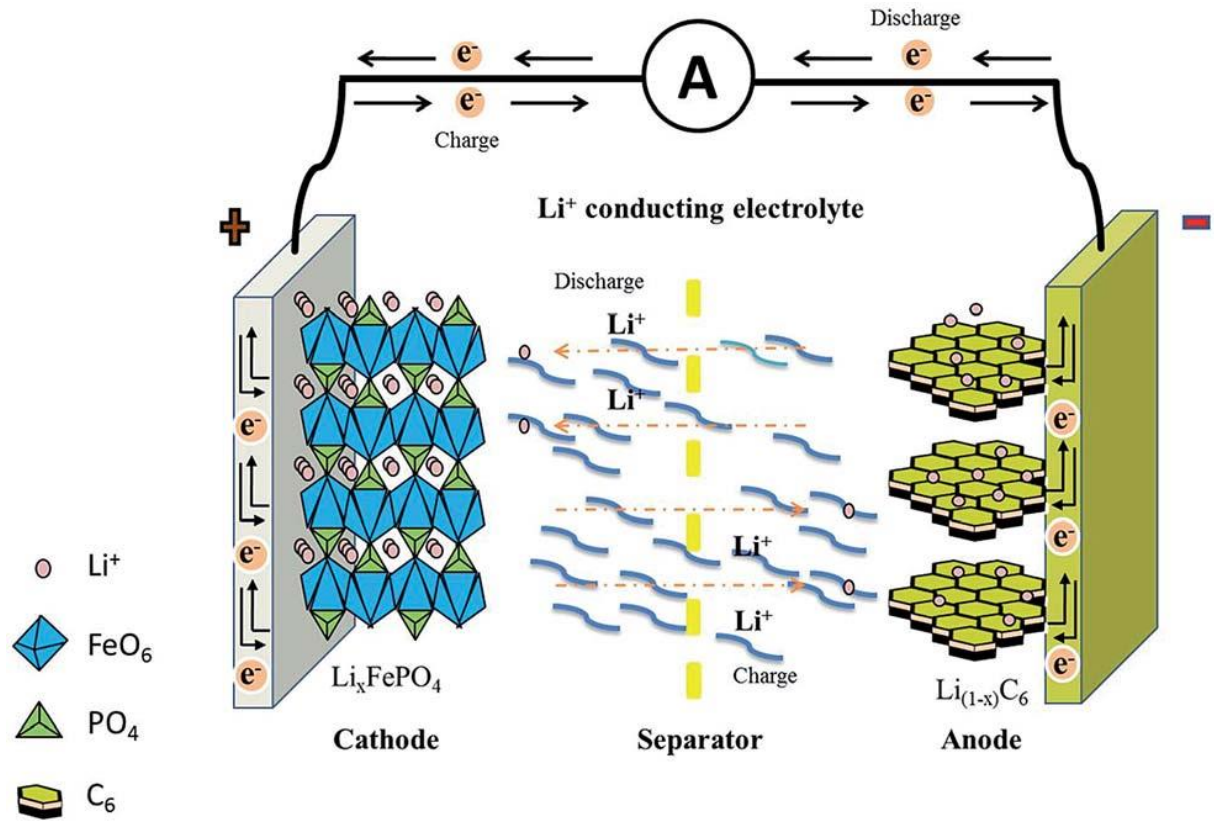
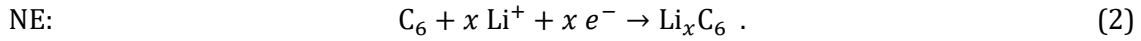
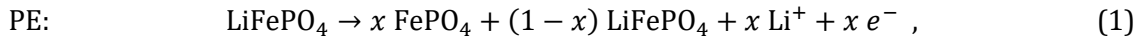


Figure 2: Scheme of LFP battery operation. Source: *H. Lee, M. Yanilmaz, O. Toprakci, K. Fu, X. Zhang, Energy Environ. Sci. 7 (2014) 3857–3886. [59]*

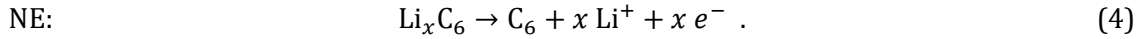
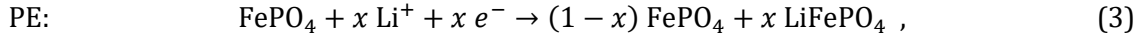
### 2.2.3 Working principle

The operation of secondary (rechargeable) lithium-ion batteries is described by the “rocking-chair” (de)intercalation mechanism, which is the reversible insertion/extraction of lithium ions from layered PE active material. The operation scheme of the LFP cells is given in Figure 2.  $\text{Li}^+$  ions migrate through electrolyte and separator to intercalate between graphite layers during charging and intercalate to octahedral sites in  $\text{LiFePO}_4$  olivine structure during discharge [13]. Electrons supplied from an external current source flow through current collectors to electrodes during charge. In reverse, electrons extracted from NE flow through current collectors to feed the external load.

The overall cell voltage is the potential difference between the redox potentials of electrodes during charge and discharge. During charge, PE oxidation and NE reduction take place according to reactions



During discharge, in reverse, PE reduction and NE oxidation take place according to the reactions



In Equation (3), PE is considered completely delithiated at the beginning of discharge. During charge/discharge, in other words, during oxidation/reduction reactions, two phases ( $\text{FePO}_4$  and  $\text{LiFePO}_4$ ) coexist in PE, forming a mosaic of lithiated and delithiated particles [60].

#### 2.2.4 Power rating

Electrical power is defined as the product of voltage and current:

$$P = I \cdot V , \quad (5)$$

where  $P$  is electrical power,  $I$  is current, and  $V$  is voltage. The manufacturer declares a commercial battery's safe operation voltage window, which is an intrinsic property depending on battery chemistry, in the product datasheet. For example, Sinopoly cells used in this study must be operated between 2.8 V and 3.8 V, and Calb cells must be operated between 2.5 V and 3.65 V according to their datasheets (Appendix 6.2). Because of the fixed operation voltage window, the power rating of a battery is dependent on its nominal operating current according to Eq.(5). The SI definition of the unit of electric current, ampere, is the electric current corresponding to the flow of approximately  $6.242 \times 10^{18}$  electrons per second. By definition, a high current rate translates into a higher number of electron transport per second in the battery. Here, the electron transfer processes within the active material, from active material to the current collector, and within the current collector play a role. In standard LFP cell, the electrical conductivities of graphite NE ( $10^3$  S/cm), Cu current collector ( $5.8 \times 10^5$  S/cm), and Al current collector ( $3.4 \times 10^5$  S/cm) are in order of  $10^{12}$  to  $10^{15}$  higher than  $\text{LiFePO}_4$  ( $10^{-9}$  S/cm) [61]. Thus, for LFP cells, the current limiting factor is the transfer of electrons from  $\text{LiFePO}_4$  to the current collector. As mentioned earlier, the low electrical conductivity of  $\text{LiFePO}_4$  compared to other LIB cathode materials such as LCO ( $10^{-4}$  S/cm) and LMO ( $10^{-6}$  S/cm) is one of the significant disadvantages of LFP cells. However, commercial LFP batteries achieved sufficient current rate capability to be feasible on the market by increasing the electrical conductivity of  $\text{LiFePO}_4$  by conductive carbon coating up to  $10^{-1}$  S/cm (for 4.74 wt. % chemically coated carbon) [56,61,62].

### **2.2.5 Energy density**

The energy density of a commercial lithium-ion battery is dependent on the nominal voltage and specific capacity of the active materials. Although LFP has a relatively high theoretical specific capacity (165 mAh/g) [58] among commercial LIB cathode materials, the theoretical energy density of LFP (379 Wh/kg) is lower than LCO (402 Wh/kg), NMC (399-416 Wh/kg), NCA (445 Wh/kg) due to low average voltage (values are calculated with graphite negative electrode) [55,56,63]. Moreover, using conductive additives and coatings reduces the weight fraction of active LFP down to 76 % in commercial stationary storage cells [42]. As a result, energy density is reduced in exchange for rate capability. For the total cell, the energy density reduces further with the overall weight contributions of the casing, separator, current collectors, and electrolyte. For example, for both cell types used in this study, the specific capacity is 101 Wh/kg in datasheets (Appendix 6.2). High energy density is not the primary objective in stationary storage cells compared to cycling lifetime and safety. Thus, stationary storage is an appropriate application for LFP cells.

### **2.2.6 Temperature performance**

Temperature dependence of cell performance (capacity, current rate capability, energy efficiency) must be considered while selecting batteries for stationary storage systems. Lithium-ion batteries demonstrate drastic capacity loss and poor current rate capability at low temperatures due to slow electrode kinetics. On the contrary, at high temperatures, high capacity and lower overpotentials are observed [13]. In terms of capacity and energy efficiency, higher ambient temperatures are advantageous for LFP cells. On the other hand, possible harmful long-term effects must be considered to assess the temperature performance of LFP cells. The long-term effects of high temperatures will be discussed in Section 2.3.

### **2.2.7 Safety and sustainability**

Safety is a key concern for commercial lithium-ion batteries. There are numerous accidents in which lithium-ion batteries caught on fire because of spontaneous thermal runaway, which results in property damage, commercial losses, and even fatalities in severe cases [64–68]. Thermal runaway results from a series of exothermic reactions of unstable electrodes and the electrolyte when internal cell temperature is elevated beyond 70 °C due to poor heat dissipation [69]. LFP cells are relatively safer compared to LCO cells because of the high-temperature stability of  $\text{LiFePO}_4$  (up to 400 °C) due to the strong covalent bonding of O with both Fe and P [14]. High-temperature stability is a significant advantage of using LFP cells, even though specific energy and energy density are lower than the alternatives.

Mechanical stability is also an essential criterion for the implementation of commercial batteries. The main mechanical stability challenge for lithium-ion batteries is the volume expansion/contraction of electrodes during intercalation reactions. High volume changes can cause loss of active material due to disassociation from the conductive network by crack formation [70–72]. Moreover, on the macro scale, large volume changes can cause deformations in cell casing that may lead to leakages and safety hazards. The advantage of LFP cell PE is that the lithiated ( $\text{LiFePO}_4$ ) and delithiated ( $\text{FePO}_4$ ) states have the same crystal lattice structure (Pnma), so no lattice distortion is present. However, the volume difference between lithiated and delithiated states of LFP (~6.8 %) is higher compared to LCO (~1.9 %) [58,73]. On the other hand, the volume expansion of the fully charged commercial LFP/graphite pouch cell is limited to 1.54 % because of the counteracting contraction of LFP PE to the expansion of graphite NE [74]. Therefore, on the cell level, LFP cells have sufficient mechanical stability for utilization in battery stacks of commercial stationary energy storage systems.

$\text{LiFePO}_4$  is an abundant mineral found in nature [14], and none of the elements in LFP batteries are considered precious. Consequently, the price volatility of precious elements does not affect the material cost of LFP batteries. So, LFP batteries have a cost advantage over other common lithium-ion batterie types that contain precious metals (*e.g.*, LCO, NCA). Besides being abundant, Fe is a nontoxic transition metal. Therefore, the environmental impact of LFP battery production, disposal, and recycling is low. In conclusion, LFP batteries are considered sustainable commercial batteries due to environmental benignity and cost-efficiency.

## **2.3 LFP LITHIUM-ION BATTERIES AGING**

### **2.3.1 Investigation method**

Scientifically investigating LFP cell aging has significance because understanding the influence of operating conditions and dominant aging mechanisms contributes to improving LFP cell performance and developing new battery materials. Moreover, for BESS manufacturers, the aging investigation results can improve the accuracy of the feasibility analysis of BESS. The annual battery investment cost is calculated by dividing the total cost by the battery lifetime. At the moment of calculation, the battery cost is fixed. On the other hand, battery lifetime is a projection into the future. Therefore, the accuracy of the annual cost estimation of residential BESS depends primarily on the precision of battery lifetime

estimation, or in other words, battery aging estimation. LFP cell aging investigation fields and their prospective practical utility can be summarized within three stages:

1. The initial step of the aging investigation is finding quantification methods. For this reason, representative aging indicators must be identified. The aging indicators, in practice, can be used for precise cost-estimation and feasibility analysis.
2. Once it is possible to benchmark aging accurately, the influence of operating conditions, such as temperature and C-rate, can be investigated independently. The results can guide BESS manufacturers in developing life-extending system architectures and operation strategies.
3. The study of aging mechanisms aims to explain how operating conditions affect cell components, resulting in performance loss. Identifying aging mechanisms may lead battery manufacturers to alter cell components or compositions (*e.g.*, by adding conductive additives or doping).

In the following subsections, the aging of LFP cells is presented in the framework of the abovementioned stages.

### **2.3.2 Aging indicators**

In the literature, the possible aging indicators, which are usually measured during periodical performance tests, can be narrowed down to capacity, IR, and electrochemical impedance spectrum (EIS).

There is a consensus, which is also validated by the results of this Ph.D. thesis, that the primary aging indicator of LFP cells is capacity fade. In all the LFP aging studies on commercial cells inspected for this thesis, all LFP cells lost capacity compared to their initial capacity at the end of aging tests. The only exception is the first few activation cycles, during which some batteries undergo an initial capacity increase.

Besides capacity fade, IR is considered a possible aging indicator because several aging mechanisms (*e.g.*, solid electrolyte interface (SEI) formation, loss of active material) can contribute to an overall increase in cell resistance by increasing ohmic and charge-transfer resistance. However, no consistent aging pattern of IR change is observed in the literature. Some tests demonstrated a consistent increase in internal resistance [17,75], while others revealed no significant change in internal resistance during cyclic aging [76,77] or calendaric aging [18,78]. In some cases, internal resistance increases and decreases during different aging stages, hypothetically attributed to enhanced lithium and electrolyte distribution in the first 100 cycles after a long rest period [79]. The IR of a large-format commercial LFP cell is

in the milliohm range, and minor measurement contact position alterations can cause significant deviations in IR values between periodic controls. Thus, using IR as an aging indicator for a residential scale BESS is difficult due to the reproducibility and accuracy of measurement results.

The literature on periodic EIS measurements of aging LFP cells shows no consistent aging indicator pattern. For example, Liu et al. observed only a minor increase in the high-frequency resistance [76] by aging, while Kassem et al. presented up to 60 % increase in high-frequency resistance [80]. EIS measurements are also prone to contact resistance changes and electromagnetic field alterations between sense cables. So, for high precision, effective electromagnetic shielding is necessary. Therefore, as in the case of IR, EIS is not considered a practical and clear indicator of commercial LFP cell aging.

### **2.3.3 Operating conditions**

#### **2.3.3.1 Temperature**

The influence of temperature on commercial LFP cell aging has been observed in several studies [17,18,78,81,82]. The cylindrical 2.3 Ah cells investigated by Omar et al. showed a 15 % decrease in cycle life when ambient temperature was increased from 25 °C to 40 °C [17]. Safari and Delacourt measured 38 % capacity loss of a 2.3 Ah cylindrical cell under cyclic aging at 45 °C, compared to only 11 % at 25 °C [82]. In calendaric aging tests of cylindrical 2.3 Ah cells by Sarasketa-Zabal et al., capacity decreased almost three times as fast at 50 °C compared to 30 °C [18]. Grolleau et al. investigated calendaric aging of 15 Ah cells and measured around 50 % capacity loss after 450 days at 60 °C, compared to less than 5 % capacity loss at 30 °C [78]. The capacity loss during operation or storage above room temperature is up to four times larger compared to room temperature [77,78,83,84]. An investigation of cyclic aging of automotive LFP batteries demonstrated that the capacity loss and power fade are more severe at subzero temperatures than above room temperatures [75]. Several calendaric aging studies demonstrate that high temperatures accelerate capacity loss independent from the storage state of charge (SOC) [79,80,85].

In the literature, the harmful effect of elevated temperature on LFP cell lifetime is explained by different mechanisms. Tan et al. detected that at elevated temperatures, the amount of irreversibly lost lithium from PE increases, and the same amount of lithium deposited at the graphite NE facilitates SEI growth [84]. Besides the irreversible loss of lithium, Amine et al. proposed that at high temperatures, a higher amount of Fe<sup>2+</sup> ions dissolve from PE, migrate to NE, and are reduced at the graphite surface. The reduction of iron metal at NE catalyzes the

growth of passivation film, which increases interfacial impedance [83]. The battery life model developed by Wang et al. demonstrated that the effect of temperature on capacity loss correlates to Arrhenius law, which hints that temperature-activated aging is accompanied by a thermally activated chemical side reaction such as SEI formation [19]. The aging mechanism will be discussed in detail in Section 2.3.4.

### **2.3.3.2 Charge/discharge profile**

In commercial cells, load profile has considerable effects on cell performance. End users are familiar with this phenomenon. For example, using applications that require high processing power (high current) on smartphones shortens discharge duration significantly.

The charge/discharge current of a battery is usually expressed by C-rate, which is defined as the ratio of the charge/discharge current to the nominal capacity (given by the manufacturer) according to the equation:

$$\text{C-rate} = \frac{I \cdot 1 \text{ h}}{C_N} , \quad (6)$$

where  $I$  is the current and  $C_N$  is the nominal capacity. C-rate is proportional to charge/discharge current and inversely proportional to charge/discharge time, so a higher C-rate corresponds to a higher charge/discharge current but a faster charge/discharge. Defining charge/discharge C-rate for residential stationary storage applications is an important design choice for manufacturers. For example, a higher C-rate enables a higher power supply during discharge but shorter battery operation time. Furthermore, the effect of high C-rate operation on battery aging determines system lifetime. Cycle life tests of commercial LFP cells under a dynamic load profile reveal that high C-rates increase cell temperature [17]. So, high C-rates accelerate aging indirectly by increasing overall cell temperature. Moreover, higher current flow induces a higher diffusion rate, creating extra stress and cracks on graphite NE. The cracks on the graphite surface cause the dissociation of the active material from the NE and damage the passivating SEI layer. Consequently, some of the lithium inventory is consumed irreversibly to repair the SEI layer, which results in irreversible capacity loss. [19]. In contrast, Lewerenz et al. demonstrated that high C-rates may lead to a longer lifetime due to a homogenous heat profile within the cell [79]. Similarly, the cycling experiments of 26650 type LFP cells performed by Dubarry et al. showed that high C-rate cycling caused a capacity increase in the first 100 cycles and no C-rate dependence of capacity loss after that [31]. As a result, there is no consensus in the literature that cycling at high C-rates accelerates LFP aging, independent from other operating conditions. Instead, the C-rate dependency of aging must be investigated case by case.

Quantifying the effects of different DOD levels on LFP cell aging may increase the feasibility of BESS by implementing life-extending charge/discharge ranges. Omar et al. observed that low DOD results in more cycles until the end of life [17], while according to Wang et al., the effect of DOD is less prominent at low C-rate [19]. More interestingly, Lewerenz et al. observed significantly faster aging at 10 % DOD (between 45 % SOC – 55 % SOC) than 50 % DOD (between 25 % SOC – 75 % SOC) or even 100 % DOD [79]. The results of Lewerenz et al. point out that LFP cell aging also depends on the SOC region in which the cell operates, besides DOD. The studies on LFP cell aging under storage (calendaric aging) demonstrate that at the same temperature, higher SOC accelerates capacity loss [18,78,80,85].

Unlike the studies mentioned above, during the practical operation of a residential BESS under realistic load profiles, the charge/discharge cycles are mostly asymmetrical (mismatch between charge and discharge C-rate). During asymmetrical cyclic aging, the capacity loss is higher than in symmetrical cycles, even at higher C-rates [82,86]. An exemplary study by Wikner et al. on the aging of LFP cells operated under a realistic load profile showed that avoiding high SOC and using small DOD (little charges) increase lifetime expectancy by more than 40 % [87]. Therefore, the influence of operating conditions must be investigated under realistic load profiles for a precise aging estimation.

### **2.3.3.3 Cell design**

Design-related factors such as cell geometry (*e.g.*, electrode thickness and area), assembly method (*e.g.*, jelly roll, prismatic), and thermal management of cell casing may have an auxiliary effect on cell performance and aging by affecting the abovementioned operating conditions. For example, high-power cells tend to have thinner electrodes to facilitate reaction kinetics with the cost of less active material loading per volume so that specific cell capacity is low, but capacity fade is not rate-dependent [88].

### **2.3.4 Aging mechanisms and degradation modes**

During the lifetime of LFP lithium-ion batteries, chemical (*e.g.*, SEI formation, electrolyte decomposition) and physical (*e.g.*, particle cracking, electrical contact loss) degradation mechanisms are responsible for cell performance loss. For the diagnostics of the aging of commercial lithium-ion cells, the individual contribution of each aging mechanism may not be easily quantified with the limited data recorded throughout the measurements, such as voltage, current, and temperature. Therefore, Birkl et al. proposed grouping mechanisms into degradation modes whose effect can be quantified by changes in the open circuit voltage (OCV) curves [89]. The aging mechanisms can also be grouped according to underlying operating conditions (*e.g.*, temperature, SOC) or associated battery components: PE,



electrolyte, NE [90]. In this Ph.D. thesis, we follow the degradation modes approach and accordingly group the aging mechanisms into two degradation modes: loss of active material (LAM) and loss of lithium inventory (LLI) [31].

#### **2.3.4.1 Loss of active material (LAM)**

The active material comprises the electrode particles participating actively in the electrochemical reactions, excluding binders, conductive additives, and current collectors. The theoretical cell capacity is calculated assuming all active material content is available for charge/discharge reactions. Thus, irreversible LAM reduces cell capacity beneath its initial value.

LAM is caused by different mechanisms, such as the isolation of active material particles due to particle cracking, the formation of fully passivating surface layers [91], or electrode dry-out [27]. One of the proposed pathways to cause loss of active material of the PE ( $LAM_{PE}$ ) is electrochemical milling, which is the process in which LFP particles crack and crumble because of mechanical stress as a result of volumetric change during Li (de)intercalation [31]. Initially, the cracked particles increase total surface area (increasing surface-to-volume ratio), enhancing redox reaction kinetics. On the other hand, it is shown that these cracks increase electrode polarization and poor electric contact between active material and conducting agents [71]. Further cracking may detach active material from the electron-conductive path. The isolation of active material causes LAM and further LLI if the dissociated particles are already lithiated. Moreover, these isolated particles can migrate to the negative electrode to become parasitic reaction sites that promote SEI layer growth, especially at high temperatures [88]. It is proposed by Zhi et al. that higher crystallization of the PE material by high-temperature synthesis can improve the stability and prevent the dislocation of active material from conductive carbon [92].

The loss of active material of the NE ( $LAM_{NE}$ ) is revealed by the post-mortem micrographs of a cylindrical 8 Ah commercial LFP cell. According to the images, a dense passivation layer formed by Li plating deactivates certain areas on the electrode surface by inhibiting the transportation of ions, which causes active material to not participate in electrochemical reactions [79].

#### **2.3.4.2 Loss of lithium inventory (LLI)**

In lithium-ion batteries, lithium is the source of electrons that flow through an external load during discharge (which is the intended usage of the battery). Thus, the amount of charge is

limited with available lithium inventory that can participate in redox reactions. Similar to the LAM, LLI causes irreversible loss of cell capacity.

The most dominant mechanism causing LLI is the formation of the SEI due to the decomposition of the electrolyte [93,94]. The initial formation of the SEI layer is beneficial for cell lifetime by passivating the NE surface from electrolyte decomposition. Ideally, SEI must allow  $\text{Li}^+$  ion transport but insulate electrons to prevent further decomposition. The formation and growth of the SEI layer is a complex process depicted in Figure 3. It is proposed that some unstable components decompose with aging from the initial SEI layer, leaving a porous layer behind. The porosity causes further reduction of the electrolyte, which results in the thickening of the SEI layer [95]. Consequently, cyclable lithium inventory is irreversibly lost during stable inorganic SEI species formation.

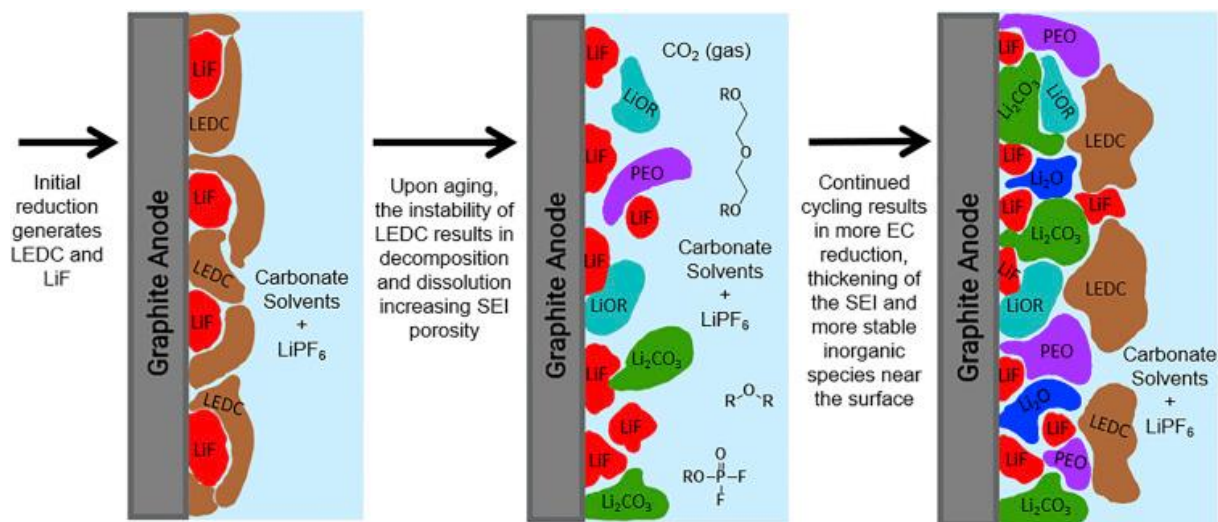


Figure 3: Schematic representation of initial growth, decomposition, and further growth by aging of SEI layer. Source: *S.K. Heiskanen, J. Kim, B.L. Lucht, Joule 3 (2019) 2322–2333 [95]*.

XRD and microscopic analysis of aged LFP cells demonstrate that intercalation of  $\text{Li}^+$  ions changes the crystal structure of the graphite anode and creates cracks on the SEI layer. Then, active Li participates in SEI growth, resulting in LLI [76]. Additionally,  $\text{Fe}^{2+}$  ions released from PE due to dissolution migrate to the SEI layer to facilitate film growth and LLI [13,75,78,83]. The capacity loss models demonstrate that capacity loss has the square root of time dependency, which is interpreted as consistent with 1D diffusion-limited SEI layer growth kinetics [18,19,96].

LLI is proposed to be the dominant capacity loss mechanism, identified by the shortening of the highest charge voltage plateau corresponding to the last lithiation step of graphite NE [18]. Thus, LLI leads to incomplete lithiation of NE at the end of charge [31]. The incremental capacity analysis also concludes that LLI is solely responsible for the irreversible capacity loss due to kinetic-limited SEI layer growth [77,80]. The comprehensive electrochemical and structural analysis of Tan et al. on capacity-fade mechanisms demonstrated that LLI is the primary degradation mechanism, accounting for more than 85 % capacity loss. Furthermore, most of the Li lost at the PE is detected at the NE/electrolyte interface. XRD analysis displays the emergence of FePO<sub>4</sub> peaks after aging as a result of irreversible Li loss [84]. These results again indicate that the primary degradation mode of LFP cells is LLI.

### 2.3.5 Computational analysis of degradation modes

During the standard operation of a commercial residential BESS, advanced measurement techniques such as EIS or time-consuming IR pulse tests may not be practical for detecting battery degradation. Dubarry et al. proposed a mechanistic modeling approach for simple diagnostics of degradation modes [44]. According to their approach, the full-cell voltage response is a convolution of the half-cell voltage responses, depending on the two electrodes' relative capacities ("loading ratio") and a shift of the half-cell curves against each other ("offset"). From a physically-based viewpoint, these properties are directly related to the electrode thicknesses, volume fractions of active materials, and lithium stoichiometry ranges used for cycling. They are also referred to as the *balance* of the electrodes [97]. Time-resolved analysis of the electrode balances demonstrates the effect of different degradation modes (LAM and LLI) on battery aging. This concept has been termed by Dubarry et al. as "mechanistic modeling" and has been widely adopted in the lithium-ion battery aging literature [89].

The practical analysis of electrode balancing and degradation modes is possible with electrochemical voltage spectroscopies (EVS), that is, differential voltage analysis (DVA) [91,93,98] and incremental capacity analysis (ICA) [45]. By examining characteristic slopes and peaks in the differential voltage plot, it is possible to infer the electrode balancing and, with it, the ongoing aging mechanisms of the electrodes. The differential voltage  $dV_{\text{cell}}/dQ$  represents the derivative of the cell voltage  $V_{\text{cell}}$  with respect to the charge  $Q$ . Since the differential voltage curve is a superposition of the half-cell potential derivatives, the characteristics of the PE and NE can be separated according to

$$\frac{dV_{\text{cell}}}{dQ} = \frac{dV_{\text{PE}}}{dQ} - \frac{dV_{\text{NE}}}{dQ} . \quad (7)$$

DVA and ICA require knowledge of the half-cell potential curves of both electrodes, which are usually obtained experimentally in dedicated coin-cell experiments. The analysis of degradation modes requires that the half-cell curves do not change over the lifetime and that the cell aging is homogeneous. If this is not the case, it is not possible to adjust the change in the measured full-cell voltage derivative by simply superimposing the half-cell derivatives from the negative and positive electrodes. The height of the characteristic peak in the DVA plot can qualitatively determine the homogeneity of aging. The flattening or disappearance of this peak indicates heterogeneous aging [93]. DVA peaks are more pronounced at low charge or discharge currents ( $C/20$  and smaller), so test data should be ideally generated at low currents [98]. The DVA analysis is further explained in Section 4.3.4.1 with a DVA plot (Figure 36).

## 3 METHODOLOGY

---

### 3.1 DEFINITION OF TEST PARAMETERS

The consistency of nomenclature and definition of test parameters must be maintained rigorously throughout the text. Therefore, as a first step, all terminology is used in the text as defined in this section unless specified differently.

- **Nominal capacity**

Nominal capacity ( $C_N$ ) is declared by the cell manufacturers as the full discharge capacity measured under the test conditions described in the cell datasheet. It is generally used as a commercial feature of the battery. For example, the LFP cells used in this study are sold as “180 Ah LFP cells.” Here, 180 Ah is given as the nominal capacity of the cells in datasheets.

- **Initial capacity**

The initial capacity ( $C_0$ ) is the as-received full discharge capacity measured by the respective method defined by each experiment individually (cf. Section 3.4.1.2). This value is used as a reference to calculate capacity loss throughout aging experiments.

- **Actual capacity**

The actual capacity ( $C_R$ ) is the last measured full discharge capacity of the cell according to the capacity test protocol of the respective cell.

The initial capacity and actual capacity ( $C_0, C_R$ ) are calculated during full discharge according to

$$C = Q_{\text{discharge}} , \quad (8)$$

where  $Q_{\text{discharge}}$  is the accumulated charge supplied by the battery during discharge.

- **State of Charge**

State of charge (SOC) represents the remaining cell capacity percentage, according to

$$\text{SOC (\%)} = \frac{Q}{C_R} \times 100 , \quad (9)$$

where  $Q$  is the measured charge throughput and  $C_R$  is the actual discharge capacity of the cell.

- **State of Health**

State of health (SOH) is used as a benchmark for capacity retention, defined as the ratio of actual cell capacity to initial capacity according to

$$\text{SOH (\%)} = \frac{C_R}{C_0} \times 100 . \quad (10)$$

The industry standard defines 80 % SOH as the end of life of a battery. In other words, the commercial life of a battery ends when the actual cell capacity reduces more than 20 % of the initial capacity.

- **Coulombic efficiency**

Coulombic efficiency (CE) is the ratio of charge supplied by the cell during discharge to the charge supplied to the cell during charge according to

$$\text{CE} = \frac{Q_{\text{discharge}}}{Q_{\text{charge}}} , \quad (11)$$

where  $Q_{\text{discharge}}$  is charge throughput during discharge and  $Q_{\text{charge}}$  is charge input during charge. Ideally, this value must be unity because the net charge input/output is independent of overpotentials. Throughout the experiments, CE was measured under the conditions (*i.e.*, temperature, C-rate, charge/discharge method) indicated when the results are presented in the Results and Discussion section.

- **Energy efficiency**

The electrical energy efficiency ( $\eta_{\text{energy}}$ ) of the cell is calculated according to

$$\eta_{\text{energy}} = \frac{E_{\text{discharge}}}{E_{\text{charge}}} = \frac{\int_{\text{discharge}} I(t) \cdot V(t) \cdot dt}{\int_{\text{charge}} I(t) \cdot V(t) \cdot dt} , \quad (12)$$

where  $E_{\text{discharge}}$  is the electrical energy supplied from the cell during discharge and  $E_{\text{charge}}$  is the electrical energy supplied to the cell during charge.  $\eta_{\text{energy}}$  is inversely proportional to charge and discharge overpotentials, which means that higher overpotentials result in lower energy efficiency. In other words, low efficiency corresponds to higher energy loss. Thus, it is a helpful benchmark for overall cell performance. Throughout the experiments,  $\eta_{\text{energy}}$  was measured under the conditions (*i.e.*, temperature, C-rate, charge/discharge method) indicated when the results are presented in the Results and Discussion section.

- **Internal resistance**

Internal resistance (IR) of the cells was calculated using two different methods throughout the experiments: pulse measurement and cyclic average.

**Pulse measurement method:** During periodic performance tests, dedicated IR measurements were performed using the pulse measurement method. In this method,  $IR_{\text{pulse}}$  is calculated by applying a current pulse at a given time ( $t_0$ ) during charge/discharge. From voltage response recorded after some time ( $t_1$ ), IR is calculated according to

$$IR_{\text{pulse}} = -\frac{V(t_1) - V(t_0)}{I(t_1) - I(t_0)}, \quad (13)$$

where  $V(t_1)$  corresponds to the voltage measured at  $t_1$ ,  $V(t_0)$  corresponds to the voltage measured at  $t_0$ ,  $I(t_1)$  corresponds to the pulse current measured at  $t_1$ ,  $I(t_0)$  corresponds to regular charge/discharge current measured at  $t_0$ .

**Cyclic average method:** The internal resistance of the cells during cyclic aging was calculated by the cyclic average method. In this method, IR is calculated from the post-process analysis of characteristic charge/discharge curves.

We used two different approaches to calculate IR from charge/discharge curves. In the first approach (*i.e.*, constant current (CC) cyclic average method), we aim to use only the CC part of charge/discharge curves to calculate  $IR_{\text{cycle,CC}}$ . In order to ensure that only the CC part is used, the calculation was made by using test data between 10 % and 90 % SOC according to

$$IR_{\text{cycle,CC}} = \frac{\bar{V}_{\text{chg}[10-90\%]} - \bar{V}_{\text{dis}[10-90\%]} - \Delta V_{\text{hys}}}{2 \cdot I_{\text{CC}}}, \quad (14)$$

where,  $I_{\text{CC}}$  is the constant charge/discharge current,  $\bar{V}_{\text{chg}[10-90\%]}$  is the average charge voltage between 10 % and 90 % SOC, and  $\bar{V}_{\text{dis}[10-90\%]}$  is the average discharge voltage between 90 % and 10 % SOC. In this calculation, we considered the thermodynamic voltage hysteresis known from LFP [99], which we quantified experimentally for our cell to  $\Delta V_{\text{hys}} = 42.9$  mV.

In the second approach (*i.e.*, full cyclic average method), cyclic IR is calculated by using a full charge/discharge curve according to

$$IR_{\text{cycle,full}} = \frac{\bar{V}_{\text{chg}} - \bar{V}_{\text{dis}}}{\bar{I}_{\text{chg}} - \bar{I}_{\text{dis}}}, \quad (15)$$

where  $\bar{V}_{\text{chg}}$  is the average charge voltage,  $\bar{V}_{\text{dis}}$  is the average discharge voltage,  $\bar{I}_{\text{chg}}$  is the average charge current, and  $\bar{I}_{\text{dis}}$  is the average discharge current in full charge/discharge cycle.

- **Charge/discharge procedures**

The practical operation of a battery can be divided basically into three phases: rest, charge, and discharge. During these phases, only voltage, current, time, and sensor data such as temperature can be measured as independent variables via battery cyclers.

During charge and discharge, we can control cell voltage and measure current (constant voltage, CV), control current and measure cell voltage (CC), or control power and measure both voltage and current (constant power, CP). For safety reasons, commercial batteries have an operating voltage window and maximum current limitation. Throughout this study, either CC or CV charge/discharge methods were used.

In full cycles, end of charge and discharge voltages are defined as CC charge/discharge cut-off criteria. However, once the cells have reached these potentials, there is still some capacity that can be used at lower currents that cannot be used at high currents due to high overpotentials. Therefore, it is a generally accepted practice to switch to CV operation once the cell reaches cut-off voltage. The current diminishes continuously under CV operation because cell capacity is limited. To avoid continuing CV mode forever, the operator defines the time or minimum (cut-off) current criteria to keep a reasonable balance between charge/discharge time and extra CV phase capacity. Such a procedure in which CC charge/discharge is followed by a relatively short CV charge/discharge is defined as constant current constant voltage (CCCV) charge/discharge.

## **3.2 TEST BATTERIES**

Throughout the experiments, two different commercial LFP lithium-ion cells from two different Chinese manufacturers, Shenzhen Sinopoly Battery Co. Ltd. (“Sinopoly”) and China Aviation Lithium Battery Co. Ltd. (“Calb”), were used. The main application field of these cells is stationary storage.

All the cells were chosen from the same shipment to reduce inhomogeneities. On the other hand, the cells do not have a regular serial number, production date, or batch number labeled. There is also no information in shipping documentation about production dates or batch numbers. Because of the lack of production date information, identification tags were given to the cells according to their delivery dates. Additionally, we observed different labeling



formats on batteries. It is possible that the cells in the same shipment may contain cells from different production batches. Therefore, as-received cells can already have differences in aging history. Consequently, initial electrical characterization of batteries is essential to observe whether the cells have homogenous electrical properties (*e.g.*, capacity, internal resistance) at the beginning of the experiments. In some instances, when more cells are available than needed, the cells with the closest properties were chosen to eliminate inconsistent results due to inhomogeneous cells.

Primarily, the documentation of the batteries (*i.e.*, datasheets and material safety data sheets (MSDS) (cf. Appendix 6.2)) was investigated in parallel with the visual examination of batteries. Both cell types have a prismatic geometry with polypropylene (PP) housings to enhance mechanical stability, as shown in Figure 4.



Figure 4: Photographs of the studied cells: Sinopoly (left) and Calb (right). Both cells have rigid polypropylene housings. On top of the cells, metal positive and negative connectors are visible.

The cell characteristics from manufacturers' data sheets [100,101] are given in Table 2. Both cell types have a nominal capacity of 180 Ah and a nominal voltage of 3.2 V. The chemistry of active electrode materials is specified as lithium iron phosphate as positive active material and graphite as negative active material for Calb cells. In contrast, the datasheet of Sinopoly informs positive active material as “LiFeYPO<sub>4</sub>”, a yttrium-doped lithium iron phosphate [102], and graphite as negative active material. According to the datasheet, the electrolyte of both cells consists of lithium hexafluorophosphate salt in ethylene carbonate (EC), dimethyl carbonate (DMC), diethyl carbonate (DEC) and ethyl acetate (EA) solvents. The current collectors are copper for the negative and aluminum for the positive electrode [42].

It can be noted that the cut-off voltages are quite different for the two cell types despite the same nominal voltage. The only other difference in specifications is the maximum discharge C-rates of cells: 3C (540 A) for Sinopoly and 2C (360 A) for Calb. Throughout the tests, the maximum discharge current was 1C (180 A); therefore, discharge rate limitations were never tested.

Table 2: Characteristic data of the two studied cells according to the manufacturer’s data sheets [100,101].

	<b>Sinopoly</b>	<b>Calb</b>
<b>Producer</b>	Shenzen Sinopoly Battery	China Aviation Lithium Battery
<b>Model</b>	SP-LFP180AhA	CA180FI
<b>Delivery date</b>	Feb. 2017	Nov. 2018
<b>Number of cells delivered</b>	32	42
<b>Nominal capacity</b>	180 Ah	180 Ah
<b>Nominal voltage</b>	3.2 V	3.2 V
<b>Voltage range</b>	2.8 V – 3.8 V	2.5 V – 3.65 V
<b>Maximum discharge C-rate</b>	3 C	2 C
<b>Nominal weight</b>	5.7 kg	5.7 kg
<b>Size</b>	282 x 182 x 71 mm <sup>3</sup>	280 x 180 x 71 mm <sup>3</sup>
<b>Nominal energy</b>	576 Wh	576 Wh
<b>Nominal energy density</b>	101 Wh/kg	101 Wh/kg

### 3.3 EXPERIMENTAL PROCEDURE

In this Ph.D. thesis, we investigated the aging characteristics of a full-scale commercial residential BESS in four steps. In Figure 5, the experimental procedure is summarized as a flowchart along with the corresponding publications (given with color codes), in which the methodology is explained in detail. In total, 31 Sinopoly and 15 Calb cells underwent the following experimental phases:

1. Initially, activation, cell capacity, and IR tests were performed with all commercial large-format LFP single cells (31 Sinopoly and 28 Calb).
2. Exemplary cells were selected from each cell type for detailed electrical (quasi OCV and rate-temperature performance) and structural (cell opening) characterization.
3. According to the capacity and IR measurement results, 28 Sinopoly cells were chosen and distributed into two commercial BESS battery stacks for 2.5 years of realistic operation tests. In parallel, 2 Sinopoly cells cycled continuously under controlled temperature for comparison with stack cells.
4. Finally, 12 Calb cells are chosen to investigate aging behavior on the cell level under controlled temperature and continuous charge/discharge or fixed SOC storage conditions.

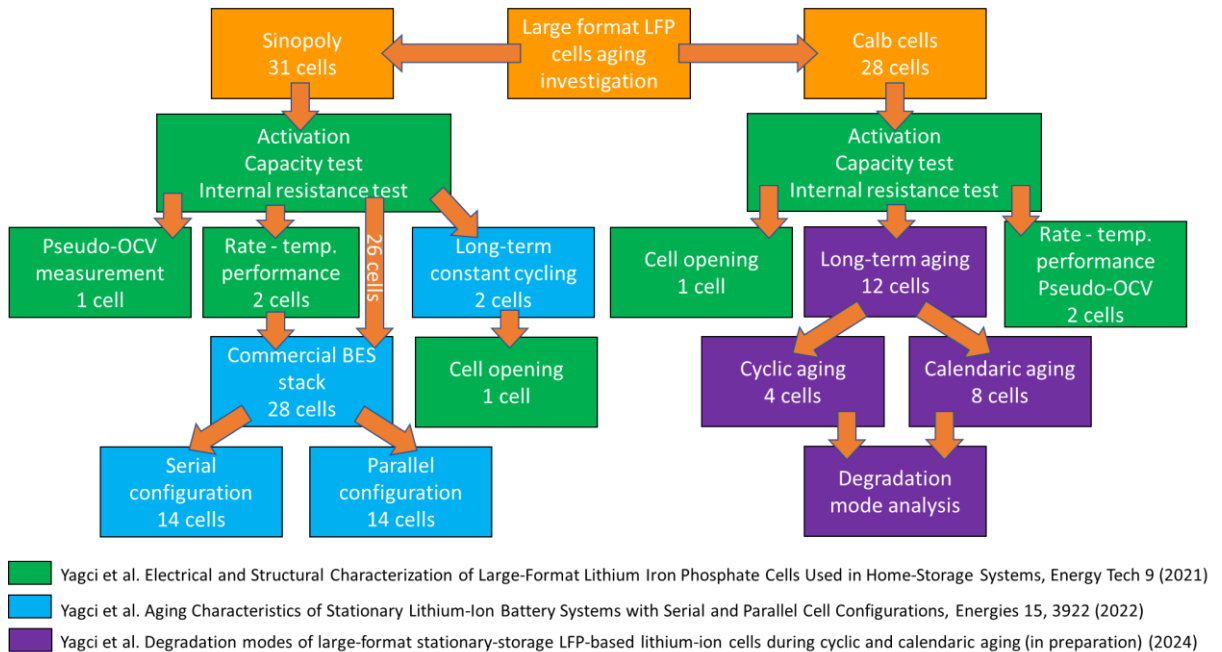


Figure 5: The flowchart of the experimental procedure. The color codes in the legend correspond to publications [42,43,103] in which the methodology and results of the experiment steps with the same color are presented.

The experimental procedures of each of the steps mentioned above, which will be explained in detail in the following subsections, were previously published or in the publication process by Yagci et al. on detailed electrical and structural characterization of LFP cells [42], long-term practical aging characteristics of two commercial residential BESS consisting of LFP cells [43], and cyclic aging and calendaric aging investigation of single commercial LFP cells under controlled ambient temperature [103].

## **3.4 CHARACTERIZATION**

### **3.4.1 Electrical characterization**

The electrical characterization of the cells was performed in the laboratory test setups using battery cyclers Biologic VMP3 (Bio-Logic Science Instruments, France), Basytec XCTS, and Basytec GSM (Basytec, Germany). During the tests, the cells were kept inside CTS-40/200 LI (CTS Clima Temperatur Systeme, Germany) climate chambers at controlled ambient temperatures specified in test protocols. Throughout measurements, cell surface temperature was measured at the center of the outer cell housing (thermocouple Type K with Biologic VMP3 and Pt100 temperature sensor with Basytec XCTS and Basytec GSM).

The initial characterization was performed in two main stages: electrical and structural. Initially, all cells underwent an activation procedure before the beginning of characterization tests. In the following, the capacity and IR of all cells were measured during the first stage of electrical characterization. Additionally, exemplary cells underwent detailed electrical characterization tests: rate capability tests, temperature performance tests, and pseudo-OCV tests.

#### **3.4.1.1 Activation**

As mentioned in Section 3.2, limited or no information was available about the history of the cells when delivered, meaning that some cells could have been stored for a long time without operation. Therefore, each cell underwent an activation procedure with the intent of reducing the harmful effects of electrochemical (*e.g.*, diffusion of ions to inactive sites in the long term) or mechanical (*e.g.*, drying of separator or electrodes due to gravity) “fatigue” on battery performance due to long periods of inactivity.

- **Sinopoly cells**

The activation of Sinopoly cells was performed by two full CCCV charge and CC discharge cycles using Basytec XCTS battery cycler at 20 °C ambient temperature controlled by CTS-40/200 LI climate chamber following the protocol in Table 3.

Table 3: Sinopoly cells activation test protocol.

Step	Technique	Control	End Criteria
1	CC charge	$I = 45 \text{ A}$	$V_{\text{cell}} > 3.8 \text{ V}$
2	CV charge	$V = 3.8 \text{ V}$	$I < 3.6 \text{ A}$
3	Rest		$t_{\text{rest}} > 30 \text{ min}$
4	CC discharge	$I = 45 \text{ A}$	$V_{\text{cell}} < 2.8 \text{ V}$
5	Rest		$t_{\text{rest}} > 30 \text{ min}$

- **Calb cells**

The activation of Calb cells was performed by two full CCCV charge and discharge cycles using Biologic VMP3 battery cyclers at 20 °C ambient temperature controlled by CTS-40/200 LI climate chamber following the protocol in Table 4.

Table 4: Calb cells activation test protocol.

Step	Technique	Control	End Criteria
1	CC charge	$I = 50 \text{ A}$	$V_{\text{cell}} > 3.65 \text{ V}$
2	CV charge	$V = 3.65 \text{ V}$	$I < 9 \text{ A}$
3	Rest		$t_{\text{rest}} > 30 \text{ min}$
4	CC discharge	$I = 50 \text{ A}$	$V_{\text{cell}} < 2.5 \text{ V}$
5	CV discharge	$V = 2.5 \text{ V}$	$I < 9 \text{ A}$
6	Rest		$t_{\text{rest}} > 30 \text{ min}$

### 3.4.1.2 Capacity tests

The initial capacity ( $C_0$ ) of each cell was measured before the beginning of aging experiments. The tests consist of two full charge/discharge cycles. The second discharge capacity was used as the initial cell capacity ( $C_0$ ) throughout the experiments.

- **Sinopoly cells**

The initial capacities of Sinopoly cells were measured using Basytec XCTS battery cyclers at 20 °C ambient temperature controlled by CTS-40/200 LI climate chamber following the same protocol as the activation procedure (cf. Table 3).

- **Calb cells**

The initial capacities of Calb cells were measured using Biologic VMP3 battery cyclers at 20 °C ambient temperature controlled by CTS-40/200 LI climate chamber following the same protocol as the activation procedure (cf. Table 4).

### 3.4.1.3 Rate capability and temperature performance tests

The retention of cell capacity at different C-rates is described with the term *rate capability*. Two individual Sinopoly and Calb cells were selected to investigate rate capability under different temperatures. Test conditions are summarized in Table 5. For each cell type, three current rates (representing low, medium, and high C-rate operation) were tested at three different temperatures (representing cold (5 °C), mild (20 °C), and warm (35 °C) temperature operation). The current differences are due to technical limitations of the battery cyclers, such as maximum current output or limited accuracy at very low currents. According to test results, the two selected cells for each cell type showed the same voltage behavior and capacity within < 2 %. Therefore, only one data set from each cell type will be shown in the results section.

Table 5: Rate capability and temperature performance test conditions for Sinopoly and Calb cells.

Cell type	Low	Medium	High	Temperature
Sinopoly	0.05C (9 A)	0.25C (45 A)	0.83C (150 A)	5 °C, 20 °C, 35 °C
Calb	0.1C (18 A)	0.28C (50 A)	1C (180 A)	5 °C, 20 °C, 35 °C

- **Sinopoly cells**

The rate capability tests of Sinopoly cells were performed using Basytec XCTS battery cyclers for each C-rate at 5 °C, 20 °C, and 35 °C ambient temperatures controlled by CTS-40/200 LI climate chamber. The low C-rate (0.05C) rate capability tests were performed by one full CCCV charge and CC discharge cycles with 30 minutes rest between charge and discharge (cf. Table 6).

Table 6: Sinopoly cells 0.05C (9 A) rate capability test protocol.

<b>Step</b>	<b>Technique</b>	<b>Control</b>	<b>End Criteria</b>
1	CC charge	$I = 9 \text{ A}$	$V_{\text{cell}} > 3.8 \text{ V}$
2	CV charge	$V = 3.8 \text{ V}$	$I < 3.6 \text{ A}$
3	Rest		$t_{\text{rest}} > 30 \text{ min}$
4	CC discharge	$I = 9 \text{ A}$	$V_{\text{cell}} < 2.8 \text{ V}$
5	Rest		$t_{\text{rest}} > 30 \text{ min}$

The medium (0.25C) rate capability tests were performed by one full CCCV charge and CC discharge cycle with 30 minutes rest between charge and discharge with the same protocol as activation (cf. Table 3). Finally, the high rate capability tests were performed by two full CCCV charge and CC discharge cycles (the second full cycle is used in analyses) with the highest current available in our test stand (150 A) following the protocol in Table 7.

Table 7: Sinopoly cells 0.83C (150 A) rate capability test protocol.

Step	Technique	Control	End Criteria
1	CC charge	$I = 150 \text{ A}$	$V_{\text{cell}} > 3.8 \text{ V}$
2	CV charge	$V = 3.8 \text{ V}$	$I < 3.6 \text{ A}$
3	Rest		$t_{\text{rest}} > 30 \text{ min}$
4	CC discharge	$I = 150 \text{ A}$	$V_{\text{cell}} < 2.8 \text{ V}$
5	Rest		$t_{\text{rest}} > 30 \text{ min}$

- **Calb cells**

The rate capability tests of Calb cells were performed using Biologic VMP3 cyclers equipped with 200 A FlexP0012 booster for each C-rate at 5 °C, 20 °C, and 35 °C ambient temperatures controlled by CTS-40/200 LI climate chamber. Low C-rate (0.1C) rate capability tests were performed by one full CCCV charge and discharge cycle with 30 minutes rest between charge and discharge according to the test protocol in Table 8.

Table 8: Calb cells 0.1C (18 A) rate capability test protocol.

Step	Technique	Control	End Criteria
1	CC charge	$I = 18 \text{ A}$	$V_{\text{cell}} > 3.65 \text{ V}$
2	CV charge	$V = 3.65 \text{ V}$	$I < 9 \text{ A}$
3	Rest		$t_{\text{rest}} > 30 \text{ min}$
4	CC discharge	$I = 18 \text{ A}$	$V_{\text{cell}} < 2.5 \text{ V}$
5	CV discharge	$V = 2.5 \text{ V}$	$I < 9 \text{ A}$
6	Rest		$t_{\text{rest}} > 30 \text{ min}$

The medium (0.28C) rate capability tests were performed by one full CCCV charge and discharge cycle with 30 minutes rest between charge and discharge with the same protocol as activation (cf. Table 4). Finally, the high rate capability tests were performed by one full CCCV charge and discharge cycle with 1C (180 A), following the protocol in Table 9.



Table 9: Calb cells 1C (180 A) rate capability test protocol.

Step	Technique	Control	End Criteria
1	CC charge	$I = 180 \text{ A}$	$V_{\text{cell}} > 3.65 \text{ V}$
2	CV charge	$V = 3.65 \text{ V}$	$I < 9 \text{ A}$
3	Rest		$t_{\text{rest}} > 30 \text{ min}$
4	CC discharge	$I = 180 \text{ A}$	$V_{\text{cell}} < 2.5 \text{ V}$
5	CV discharge	$V = 2.5 \text{ V}$	$I < 9 \text{ A}$
6	Rest		$t_{\text{rest}} > 30 \text{ min}$

#### 3.4.1.4 Pseudo-OCV tests

The determination of a cell's actual open circuit voltage (OCV) curve during aging tests is time-consuming due to the long resting times required before OCV measurements. Therefore, for practical purposes, we eliminated long resting times. Instead, we measured one CC discharge/charge cycle at a very low C-rate (0.01C for Sinopoly and 0.02C for Calb) at 20 °C ambient temperature.

Furthermore, the OCV of the cell is different on the same SOC depending on whether the cell is previously being charged or discharged. This hysteresis effect is specifically prominent in LFP lithium-ion batteries and results from the asymmetry of several factors between charge and discharge. The mechanical stress causes potential differences between individual particles, causing hysteresis due to different volume changes between charged and discharged phases as a result of different lattice constants between lithiated and delithiated particles. The average of the potentials of individual active material particles due to varying (de)lithiation rates causes the resulting electrode potential to be different from the theoretical potential of a single particle, causing voltage hysteresis [104–106].

Therefore, we took the arithmetic average of charge and discharge voltage corresponding to the same SOC of the very low C-rate full cycle results. The resulting charge/discharge characteristic curves are not theoretical OCV curves but are practically close to them. In addition, there is a limitation to the accuracy of the battery cyclers, so reducing the C-rate further would decrease the signal-to-noise ratio considerably. Therefore, we interpret these tests as pseudo-OCV or pOCV tests, because this is the minimum current value that accurate voltage measurements could be obtained from our measurement setup.

- **Sinopoly cells**

One Sinopoly cell was used for pOCV tests consisting of one full CC charge and discharge at 0.01C (1.8 A) current rate. The test was performed using Basytec GSM battery cycler at 20 °C ambient temperature controlled by CTS-40/200 LI climate chamber. The test protocol is given in Table 10.

Table 10: Sinopoly cell pseudo-OCV test protocol.

Step	Technique	Control	End Criteria
1	CC charge	$I = 1.8 \text{ A}$	$V_{\text{cell}} > 3.8 \text{ V}$
2	Rest		$t_{\text{rest}} > 30 \text{ min}$
3	CC discharge	$I = 1.8 \text{ A}$	$V_{\text{cell}} < 2.8 \text{ V}$
4	Rest		$t_{\text{rest}} > 30 \text{ min}$

- **Calb cells**

The pOCV tests of two selected Calb cells were performed using Biologic VMP3 battery cycler at 20 °C ambient temperature controlled by CTS-40/200 LI climate chamber. The test protocol is given in Table 11. Both cells underwent one full CC charge and discharge at 0.02C (3.6 A) current rate with no rest phase between charge and discharge. The pOCV test results of the two Calb cells show similar voltage behavior and capacity curve within < 1 %, so only one of the datasets was used in analyses.

Table 11: Calb cells pseudo-OCV test protocol.

Step	Technique	Control	End Criteria
1	CC charge	$I = 3.6 \text{ A}$	$V_{\text{cell}} > 3.65 \text{ V}$
2	CC discharge	$I = 3.6 \text{ A}$	$V_{\text{cell}} < 2.5 \text{ V}$

### 3.4.1.5 Internal resistance tests

The initial IR tests were performed by using the pulse test method in Eq. (13) (for all measurements, we set  $t_1 = t_0 + 3 \text{ s}$ ) for both cell types. The details of the test protocols of each cell are given in Table 12 and Table 13. As the protocol shows, the measurements were repeated throughout the whole SOC range of cells. For aging investigations, the average IR in the whole range is used to compare the aged cell with the fresh cell.

- **Sinopoly cells**

For Sinopoly cells  $IR_{\text{pulse}}$  was measured by applying a lower 0.026C (4.8 A) current pulse for 10 s during a 0.26C (48 A) continuous CC discharge of a fully charged cell at each 10 % SOC from 90 % SOC to 10 % SOC. The measurements were performed using Basytec XCTS battery cycler at 20 °C ambient temperature controlled by CTS-40/200 LI climate chamber. The test protocol is given in Table 12.

Table 12: Sinopoly cells initial internal resistance pulse test protocol.

Step	Technique	Control	End Criteria
1	CC discharge	$I = 48 \text{ A}$	$Q_{\text{discharge}} > 10 \% \cdot C_R$
2	CC discharge	$I = 4.8 \text{ A}$	$t > 10 \text{ s}$
3	Go to Step 1		$V_{\text{cell}} < 2.8 \text{ V}$

- **Calb cells**

For Calb cells  $IR_{\text{pulse}}$  was measured by applying a lower 25 A (0.14 C) current pulse for 30 s during 50 A (0.28 C) at each 2 % SOC from 98 % SOC to 2 % SOC during a full CC charge and a full CC discharge. The measurements were performed using Biologic VMP 3 battery cycler equipped with 200 A FlexP0012 booster at 20 °C ambient temperature controlled by CTS-40/200 LI climate chamber. The test protocol is given in Table 13.

Table 13: Calb cells initial internal resistance pulse test protocol.

Step	Technique	Control	End Criteria
1	CC charge	$I = 50 \text{ A}$	$Q_{\text{charge}} > 2 \% \cdot C_R$
2	CC charge	$I = 25 \text{ A}$	$t_{\text{pulse}} > 30 \text{ s}$
3	Go to Step 1		$V_{\text{cell}} > 3.65 \text{ V}$
4	Rest		$t_{\text{rest}} > 30 \text{ min}$
5	CC discharge	$I = 50 \text{ A}$	$Q_{\text{discharge}} > 2 \% \cdot C_R$
6	CC discharge	$I = 25 \text{ A}$	$t_{\text{pulse}} > 30 \text{ s}$
7	Go to Step 5		$V_{\text{cell}} < 2.5 \text{ V}$

### 3.4.2 Structural characterization

For structural and morphological characterization, one cell of each type was opened in a glovebox (MBraun Unilab Pro SP) under Argon atmosphere ( $\text{H}_2\text{O} < 1 \text{ ppm}$ ,  $\text{O}_2 < 1 \text{ ppm}$ ). For safety reasons, cells were discharged to their discharge cut-off voltages (CCCV: 0.1C CC phase followed by 48 h CV phase at discharge cut-off voltage) before opening. Figure 6 depicts the opening of the Calb cell housing. The cells were opened by removing the outer plastic housing using an oscillating cutting tool (Fein). Structural characterization of the internal geometry was performed on each cell after manually disassembling the electrode stacks. Each electrode was numbered to indicate its relative position within the cell. The total active electrode area was measured with a ruler (resolution 1 mm). The thickness of the anode, cathode, separator, and current collector sheets was measured with a thickness dial gauge (Hahn und Kolb, resolution 1  $\mu\text{m}$ ). The components were weighed by a precision balance (RADWAG PS600.X2, resolution 0.001 g). Cell opening and measurement of the geometric and structural properties of cell components are performed in cooperation with Viktor Daubert (Offenburg University of Applied Sciences) as a part of his bachelor's thesis [107].



Figure 6: The cutting of Calb cell housing inside glovebox with oscillating cutting tool (left). The detail of the cutting profile (right) [107].

For morphological characterization of the electrode microstructure, samples ( $\sim 6 \times 5 \text{ cm}^2$ ) were cut out of the electrode sheets and washed three times. Each washing step involves immersing the sample in a clean petri dish filled with DMC (anhydrous,  $\geq 99\%$ , Sigma-Aldrich) for 2 hours. The samples were flipped in the middle of the process to ensure homogeneity. The electrodes were dried overnight after the washing procedure. For each electrode of each cell type, samples were investigated by LM (Leica, DML2700 M) and SEM (JEOL JSM-6610LV).

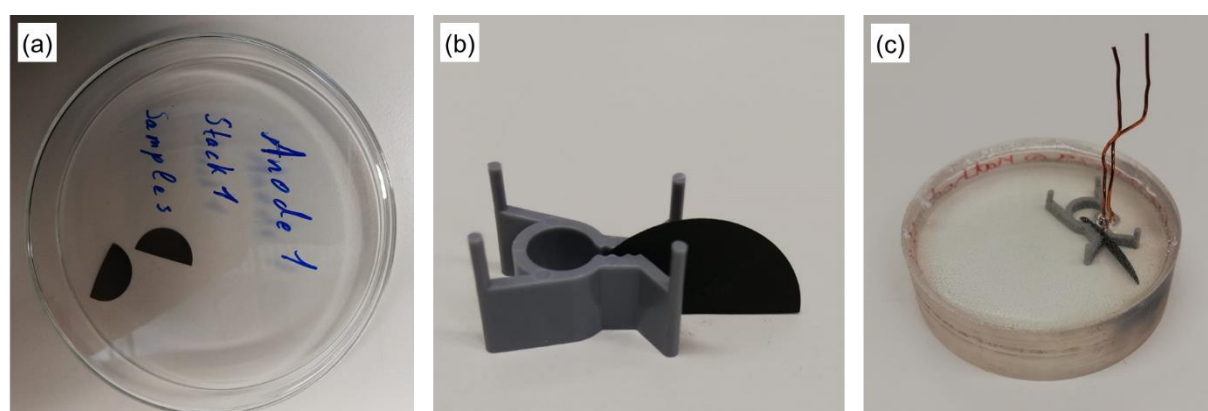


Figure 7: The steps of sample preparation for cross-sectional microscopy. Negative electrode sample of a Calb cell after washing (a). Placement in the sample holder (b). The prepared

sample for microscopy after cold mounting and polishing (c) (the copper cables attached to the sample to improve the conductivity).

For cross-sectional microscopy, samples ( $\sim 1 \text{ cm}^2$ ) were prepared by cold mounting (Epofix, Struers) and polishing processes (Struers, Tegramin 20). The polishing protocol is given in Table 14. René Behmann (Offenburg University of Applied Sciences) supported the sample preparation procedure; the details are given in his bachelor’s thesis [108]. The SEM samples were also investigated for chemical characterization by energy dispersive X-Ray (EDX) spectroscopy (Oxford Instruments X-Max). SEM and LM measurements were performed with the support of Pascale Müller (Offenburg University of Applied Sciences).

Table 14: Polishing protocol of electrode samples

Step	Disc	Medium	Contact pressure	Duration
Rough grinding	MD-Piano 220	Water	40 N	20 min
Fine grinding	MD-Largo	DiaPro Dac 9	20 N	20 min
Diamond polishing	MD-Dac	DiaPro Dac 3	20 N	15 min
Oxide polishing	MD-Chem	OP-s NonDry	20 N	5 min

### 3.5 BATTERY ENERGY STORAGE SYSTEM AGING TESTS WITH SINOPOLY CELLS

#### 3.5.1 Aging of commercial LFP cells in microgrid operation

The investigation of cell aging and stack aging characteristics of commercial LFP stationary storage systems was realized by using two commercial stationary storage systems (ASD Automatic Storage Device GmbH, Germany) with different battery architectures in realistic operation. The cell configurations of the two systems are shown in Figure 8. Each battery was constructed with 14 Sinopoly cells packed closely inside the battery cabinets. A standard configuration, in the following referred to as *serial* battery architecture, is built by serial connection of 14 cells in 14s1p configuration and operated by a single direct current (DC) to alternative current (AC) inverter. A novel configuration, in the following referred to as *parallel* battery architecture, consists of two strings of 7 parallel-connected cells in 1s7p configuration. Each string is operated by an individual DC/AC inverter. In serial configuration, active electronic control for cell balancing is performed with printed circuit boards installed

between positive and negative terminals (visible in Figure 8a). In the parallel configuration, the individual cell terminals are connected in parallel with current collection rails made out of copper, enabling passive balancing via current exchange between cells. Two systems feature two different inverters. The serial system has a 48 V (DC) – 220 V (AC) 2.4 kW inverter (Studer Xtender XTM 2600-48, Switzerland). The parallel system features two 4 V (DC) – 220 V (AC) inverters (ASD Pacadu, Germany).

Both energy storage systems are not equipped with a dedicated temperature control system. No active cooling components or fans are present in the serial system cabinet. The cabinet of the parallel system has two fans (Sunon DP200A, Taiwan) for air circulation with limited capacity (ca. 160 m<sup>3</sup>/h). Thus, the ambient laboratory temperature strongly influences the cell temperature. The microgrid laboratory, in turn, has no active cooling system, and the room temperature is subject to strong seasonal fluctuations. For the present investigations, no additional active cooling systems were installed inside the battery systems or in the laboratory to keep operating conditions close to residential usage conditions. The outside air temperature was measured by the weather station of Offenburg University of Applied Sciences mounted on the rooftop of a university building. The temperature is measured for each cell stack using a temperature sensor (Pt 100) between two selected cells within the battery stack.

Both serial and parallel system cells underwent initial electrical characterization consisting of capacity (cf. Section 3.4.1.2) and IR tests (cf. Section 3.4.1.5). Throughout the experiment, single cells were transferred between the microgrid facility and single-cell testing facility (laboratory) by disassembling the systems for initial characterization and reference performance tests three times over almost three years.

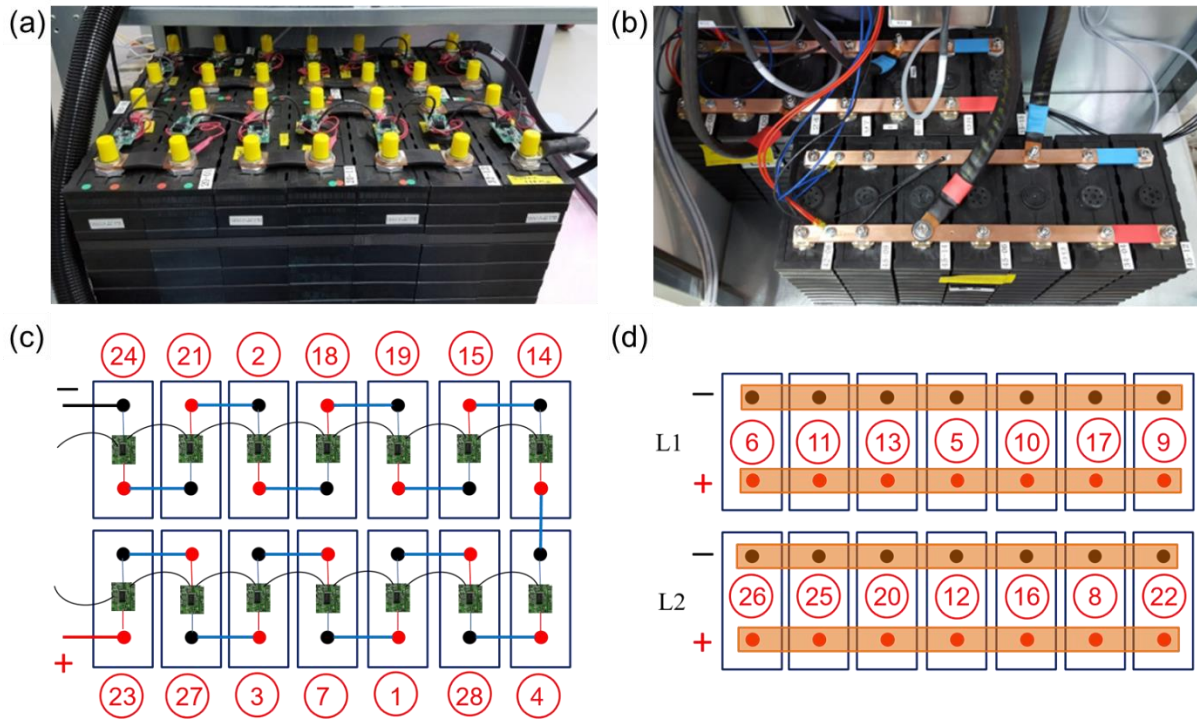


Figure 8: Photograph and schematic representation of the two different 14-cell battery architectures, (a,c) serial (one 14s1p stack) and (b,d) parallel (two 1s7p stacks L1 and L2 with individual inverters). The cell number is given as integer values in the red circles.

### 3.5.1.1 Microgrid setup

The two battery systems, as delivered by the manufacturer, were integrated into a three-phase microgrid that was developed and set up at the Institute of Energy Systems Technology (INES) at Offenburg University of Applied Sciences (Offenburg, Germany) [109]. The setup is shown in Figure 9. The microgrid consists of a photovoltaic generator with 6.5 kW nominal power including three inverters (one for each phase, SMA Sunny Boy 2000 HF, 2 kW, Germany), a small wind turbine (BRAUN Windturbinen ANTARIS SW5.5 Generator CK 7.5, 4.5 kW, Germany), the two battery storage systems (as described above), three controllable loads (one per phase, Chroma 63803 Programmable AC&DC Electronic Load, 3.6 kW, Taiwan), as well as the institute office tract and a battery electric vehicle as consumers. The microgrid can be operated stand-alone and connected to the external grid. The central system components are three network managers (one for each phase, Studer XTM 4000-48, Switzerland) (cf. Figure 9(c)), which can form an island network and include battery charging and inverter functionality. All components are fully controlled via a programmable logic controller (PLC) (Beckhoff CX2040, Germany). The batteries were placed outside the



microgrid to avoid possible interactions between the investigated battery systems and the inverters of the network managers. However, the control and operating modes were carried out as if the batteries were parts of the microgrid.

### ***3.5.1.2 Microgrid operation***

Until the end of aging tests, the two battery systems were operated strictly synchronously. The systems were controlled by the central PLC of the microgrid, which provides time-dependent AC power setpoints to the battery systems that are either given by the user or by an optimization algorithm (cf. below). The charge and discharge currents were continuously monitored and limited (depending on SOC) by the internal energy management of the battery systems. One goal of the aging investigations on the system level is to study the influence of cell configuration on aging behavior. In order to obtain reliable results from the long-term cycling test, it has to be ensured that the cells in the two battery systems are subjected to identical loads. The different capacities of the battery systems, which are due to the deviations of the individual cell capacities from their nominal value (will be discussed in Section 4.1.1), were compensated for by SOC-controlled charging and discharging, that is, charging or discharging over a given SOC range in the same period. The difference in the AC power required for SOC-controlled operation is not only due to the difference in cell capacity but also the different system efficiencies resulting from the internal energy consumption of power electronics and control of the two systems.

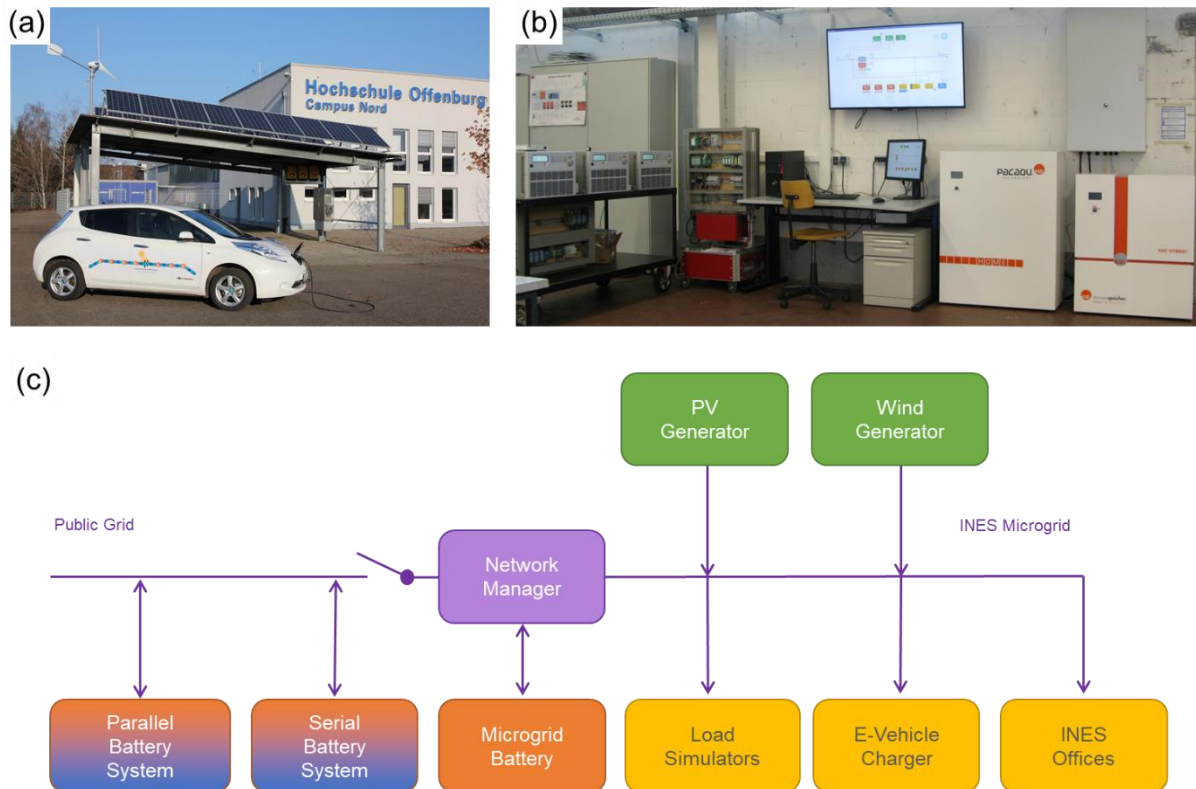


Figure 9: Microgrid at the Institute of Energy Systems Technology (INES) as operation base for the battery systems. (a) External view with wind and PV generators and battery electric vehicle, (b) internal view with serial and parallel battery systems (right), load simulators (left), and network control units (center), (c) operational scheme.

### 3.5.1.3 Operation modes

The battery systems were run in two different operating modes. The first mode, *full-cycle mode*, is applied to provoke fast aging. The battery systems were operated in continuous CC charging (0.15C) and CC discharging (0.25C) between 30 % SOC and 100 % SOC. The duration of one charge/discharge cycle was around 8.5 hours. Higher power and, thus, higher C-rates were not possible due to restrictions on the power electronics of the battery systems. The power required to charge the batteries was taken from the external grid. The electronic loads dissipated the power released during discharge.

Additionally, for 80 days, the systems were operated in a *solar-storage mode*. During this operation mode, the batteries were charged from the PV system during the day and discharged into the building during the night. Furthermore, the charge/discharge profile was precisely controlled by applying an optimization algorithm developed earlier [53,110]. In solar-storage mode, two optimization goals are combined: on the one hand, the reduction of

load peaks when feeding and drawing energy into the public power grid, and on the other hand, the prevention of cell states that are known to cause accelerated aging. The optimization algorithm is realized based on a model-predictive controller (MPC), which includes weather and load forecasts. The reader is referred to Ref. [110] for details. The resulting load profiles were qualitatively similar to what would be expected from a standard controller. Therefore, we expected that using the MPC algorithm would not change the overall conclusions of the present work on battery aging.

#### **3.5.1.4 Periodic reference performance tests (checkups)**

After the start of aging experiments, the status of the cells in terms of cell capacity, the evolution of characteristic charge/discharge curves, and IR was controlled periodically by reference performance tests (from now on referred to as “checkup”). The goal of the checkups is to detect aging patterns within the cells or compare them with each other regarding operation modes, current rate, and stack architecture. Three checkups were performed throughout the experiment after 112, 462, and 897 days of testing. The periodicity of checkups was maintained as regularly as possible. However, there were discrepancies due to technical and logistic limitations, such as the number of available test channels in the laboratory or the availability of the test personnel for disassembly and delivery of stack cells from the microgrid to the test laboratory.

Initially, the cells were disassembled from the battery stack and transported to the test laboratory. In the following, each cell underwent capacity and IR measurements (Biologic VMP3 and Basytec XCTS) in the climate chambers set to 20 °C (CTS-40/200 Li). Test protocols were identical to the initial electrical characterization measurements (cf. Section 3.4.1.2 and Section 3.4.1.5). Therefore, the initial characterization measurements are named “Checkup #0”.

#### **3.5.2 Continuous temperature-controlled cycling**

In parallel with commercial battery stack aging tests in microgrid operation, two additional Sinopoly cells were used as a test control group representing aging under controlled ambient temperature. Like BESS cells, two cells initially underwent initial characterization consisting of capacity (cf. Section 3.4.1.2) and IR (cf. Section 3.4.1.5) measurements. In the following, these two cells were subjected to continuous cycling consisting of 150 A (0.83C) CCCV charge (9 A cut-off current) and 150 A CC discharge at 20 °C ambient temperature in CTS-40/200 LI climate chamber (cf. Table 15 for test protocol). One of the cells was opened after 897 cycles for structural characterization (cf. Section 3.4.2). The remaining cell continued to cycle for 5900 full cycles.

Table 15: Sinopoly cells continuous temperature-controlled cycling test protocol.

Step	Technique	Control	End Criteria
1	CC charge	$I = 150 \text{ A}$	$V_{\text{cell}} > 3.8 \text{ V}$
2	CV charge	$V = 3.8 \text{ V}$	$I < 9 \text{ A}$
3	Rest		$t_{\text{rest}} > 1 \text{ min}$
4	CC discharge	$I = 150 \text{ A}$	$V_{\text{cell}} < 2.8 \text{ V}$
5	Rest		$t_{\text{rest}} > 1 \text{ min}$
6	Go to Step 1		

### 3.6 SINGLE-CELL CALENDARIC AND CYCLIC AGING TESTS WITH CALB CELLS

#### 3.6.1 Experimental setup

The comparison of the effects of calendaric and cyclic aging on cell aging is investigated with 12 Calb cells. Each cell underwent initial electrical characterization consisting of capacity (cf. Section 3.4.1.2) and IR measurements (cf. 3.4.1). Then, the calendaric aging cells were charged until the SOC level was reached according to the test criteria in Table 16. After, they were transferred to two separate climate chambers (Binder KB 115, Germany) set to 35 °C and 50 °C ambient temperatures, respectively. In each chamber, three tests, each consisting of two cells, are performed with the same criteria, as given in Table 16.

Table 16: Calb cells calendaric and cyclic aging test protocol.

Test group	Group 1	Group 2	Group 3	Group 4	Group 5	Group 6
Cell #	1, 2	3, 4	5, 6	7, 8	9, 10	11, 12
Temperature	35 °C	35 °C	35 °C	50 °C	50 °C	50 °C
Aging type	Cyclic	Calendaric	Calendaric	Cyclic	Calendaric	Calendaric
C-rate (Current)	0.28C (50 A)	-	-	0.28C (50 A)	-	-
SOC (Voltage)	-	75 % (3.336 V)	100 % (3.65 V)	-	75 % (3.336 V)	100 % (3.65 V)
DOD	100 %	-	-	100 %	-	-

The calendaric aging cells were kept actively at the target SOC (“floated”) by applying continuous constant voltage (CV) with Basytec GSM battery cycler at corresponding voltages (given in parenthesis under test SOC levels in Table 16) calculated from pOCV curves. So, calendaric aging cells were continuously connected to the battery cycler to stay constantly at the set voltage. Figure 10 shows exemplary current and voltage time profiles of a calendaric aging cell. Continuous but small current fluctuations (ca. 0.75 A, corresponding to around C/250) are visible. The observed average current of ca. -0.4 A is likely an offset of the current measurement.

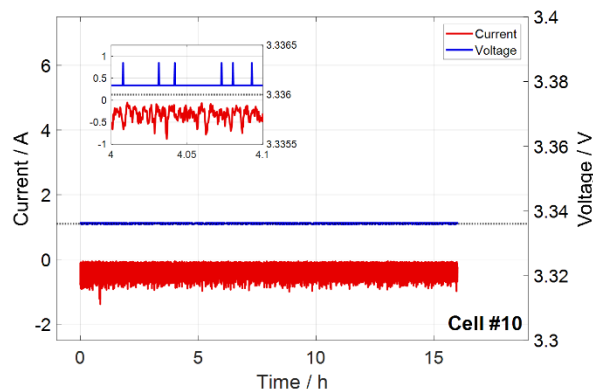


Figure 10: Current and voltage of Cell #10 as a function of time for an exemplary calendaric aging period at 50 °C. The black dotted line represents the battery cycler set voltage. Inset: Detail of current and voltage fluctuations in a 6-minute timeframe.

Cyclic aging cells underwent full CCCV cycles with Basytec XCTS battery cycler consisting of 50 A (0.28 C) constant current (CC) phase followed by constant voltage (CV) phase with 9 A (0.05 C) cut-off current for both charge and discharge (cf. Table 17). The cells rested only 10 seconds after each charge and discharge. The test plan was programmed to run for 100 cycles and restart to segment the test data for efficient data recording and continuous data analysis.

Table 17: Calb cyclic aging cells test protocol.

Step	Technique	Control	End Criteria
1	CC charge	$I = 50 \text{ A}$	$V_{\text{cell}} > 3.65 \text{ V}$
2	CV charge	$V = 3.65 \text{ V}$	$I < 9 \text{ A}$
3	Rest		$t_{\text{rest}} > 10 \text{ s}$
4	CC discharge	$I = 50 \text{ A}$	$V_{\text{cell}} < 2.5 \text{ V}$
5	CV discharge	$V = 2.5 \text{ V}$	$I < 9 \text{ A}$
6	Rest		$t_{\text{rest}} > 10 \text{ s}$
7	Go to Step 1		Cycle number > 100

### 3.6.2 Periodic reference performance tests (checkups)

Similar to the Sinopoly cells tested in Section 3.5.1, the status of all Calb cells (cyclic and calendaric aging) was monitored by four regular checkups performed when cyclic aging cells made 100, 500, 1000, and 1500 full cycles. The calendaric aging cells' checkups were performed simultaneously with cyclic aging cells. The interval of checkups corresponds to 106, 255, 553, and 846 days of calendaric aging on average. Before each checkup, all climate chambers containing the cells were set to 20 °C and kept for at least one day at 20 °C to ensure thermal equilibrium. The initial and following checkups were performed at 20 °C ambient temperature following the same protocol as the initial electrical characterization (cf. 3.4.1) consisting of capacity tests and IR measurements. The initial checkup (checkup #0) measurements are performed by Biologic VMP3 battery cycler inside CTS-40/200 LI climate chambers. The following checkup (#1-4) measurements are performed by Basytec XTS and Basytec GSM battery cyclers inside Binder KB 115 climate chambers. Additionally, during checkups of cyclic and calendaric aging cells, low-C-rate (0.1C = 18 A) CCCV cycling (9 A CV phase cut-off current) measurements (same protocol as the low C-rate capability test on Table

8) were performed at 20 °C in order to calculate pOCV curves by taking the average of charge and discharge voltage at any given SOC.

### 3.7 ANALYSIS OF DEGRADATION MODES

The single-cell calendaric and cyclic aging test data of single Calb cells (cf. Section 3.6) was post-processed to quantify the contribution of different degradation modes on overall cell performance. The analysis consists of three stages: (1) determination of the electrode balances from measured pOCV data; (2) quantification of degradation modes from these results; and (3) practical parameter identifiability. Oliver Richter supported the degradation mode analysis of aging data as a part of his seminar paper [111].

#### 3.7.1 Electrode balances

The “balance” of the positive and negative electrodes refers to the range of lithium stoichiometries ( $x$  in  $\text{Li}_x\text{C}_6$  for graphite,  $y$  in  $\text{Li}_y\text{FePO}_4$  for LFP) that the cell uses during cycling between the cut-off voltages. We define the lithium stoichiometries  $x$  and  $y$  as the lithium concentration relative to the maximum lithium concentration according to

$$x \text{ or } y = \frac{c(\text{Li})}{c_{\max}(\text{Li})}, \quad (16)$$

where  $c(\text{Li})$  is the actual lithium concentration and  $c_{\max}(\text{Li})$  is the maximum lithium concentration in graphite (negative electrode) or LFP (positive electrode). Theoretically, lithium stoichiometry varies between 0 and 1. However, in practice, the complete range may not be accessible, for example, in lithium cobalt oxide  $\text{Li}_x\text{CoO}_2$ , the material decomposes when  $x < 0.5$ .

The aim of electrode balances analysis is to empirically determine the actual stoichiometry ranges of both electrodes during a full cycle using pOCV measurements. The methodology to determine the electrode balances from measured pOCV curves is developed in-house and presented in Ref. [97]. According to the method, the full-cell pOCV curve  $V_{\text{cell}}^{\text{eq}}$ , depending on the full-cell charge throughput  $Q$ , is a superposition of the two half-cell potential curves,  $V_{\text{PE}}^{\text{eq}}$  (positive electrode) and  $V_{\text{NE}}^{\text{eq}}$  (negative electrode), depending on the half-cell lithium stoichiometries  $X_{\text{PE}}$  (positive electrode),  $X_{\text{NE}}$  (negative electrode). The stoichiometry ranges are determined by comparing full-cell OCV curves synthesized from the half-cell curves to the measured pOCV of the target cell using mathematical optimization. Mathematically, this is described as the nonlinear optimization problem

$$\min_p \chi^2 = \min_p \left[ \sum_{n=1}^N \left( \frac{d}{dQ} (V_{\text{cell,exp}}^{\text{eq}})_n - \frac{d}{dQ} (V_{\text{cell,mod}}^{\text{eq}})_n \right)^2 \right], \quad (17)$$

with five unknown parameters,

$$p = \{X_{\text{PE}}^{\text{min}}, X_{\text{PE}}^{\text{max}}, X_{\text{NE}}^{\text{min}}, X_{\text{NE}}^{\text{max}}, C_{\text{cell}}\}. \quad (18)$$

Here,  $C_{\text{cell}}$  is the full-cell capacity calculated from electrode balances analysis,  $V_{\text{cell,exp}}^{\text{eq}}$  is the measured pOCV curve,  $V_{\text{cell,mod}}^{\text{eq}}$  is the synthetic pOCV curve calculated from the half-cell potential curves,  $\chi^2$  is the merit function, and the sum run over  $N$  measured data points of the pOCV curve. The merit function represents the deviation between experimental and synthetic DV curves. The required methods for interpolation, table manipulation, and optimization are taken from MATLAB (R2019a). The interior-point algorithm implemented in MATLAB's *fmincon* solver is used for optimization. As defined above,  $V_{\text{cell,exp}}^{\text{eq}}$  values are obtained directly from pOCV measurements. In order to create a synthetic pOCV curve ( $V_{\text{cell,mod}}^{\text{eq}}$ ) the half-cell potential curves of the two active materials (AM) are needed. As half-cell measurements are not included in the experimental framework, we use literature data. For LFP, half-cell potential curves are taken from Verbrugge et al. [112], and entropies from Viswanathan et al. [113]. For graphite, half-cell potential curves are taken from Smekens et al. [114], and entropies from Reynier et al. [115]. The geometrical parameters are taken from the results of structural characterization (cf. 3.4.2) of the Calb cells [42].

Figure 11 shows exemplary results of electrode balances analysis of a cell as-received. Half-cell curves from the literature are shown as thin solid lines in panels (b) and (c), whereas the calculated stoichiometry ranges are represented as thick solid lines. The end points of the used stoichiometry ranges represent the full and empty battery states. As a result, the best-approximated parameter set is provided.

In analyzing the cyclic aging test cells, the latest parameter set is used as the starting parameter set for the upcoming optimization. Consequently, it is ensured that a parameter set adapted to the age always serves as the basis for the optimization.



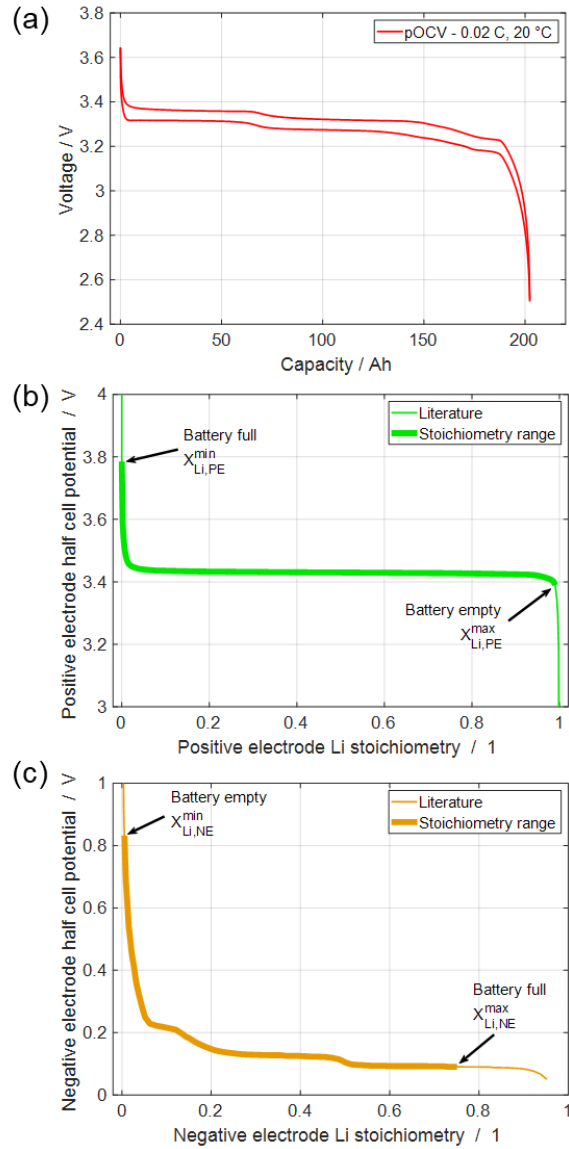


Figure 11: (a) Full cell pOCV curve of a fresh cell measured charged and discharged by 0.02 C-rate at 20 °C. (b) Positive electrode and (c) negative electrode half-cell potential curves and respective Li stoichiometry ranges calculated by electrode balancer analyses.

### 3.7.2 Calculation of degradation modes

As mentioned earlier, the analysis of degradation modes is performed with the assumption that three degradation modes are present: loss of active material of the positive electrode ( $LAM_{PE}$ ), loss of active material of the negative electrode ( $LAM_{NE}$ ), and loss of lithium inventory (LLI).  $LAM_{PE}$ ,  $LAM_{NE}$ , and LLI are quantified regarding capacity  $Q$  (Ah).

### 3.7.2.1 Loss of active material (LAM)

For our analysis, we assume that the actual used stoichiometric range diminishes due to the loss of active materials in both electrodes. The stoichiometry range  $\Delta X$  at any given time  $t$  is defined by using upper and lower stoichiometry limits ( $X^{\max}$  and  $X^{\min}$ ) computed by electrode balances analysis as following

$$\Delta X_{\text{PE}}(t) = X_{\text{PE}}^{\max}(t) - X_{\text{PE}}^{\min}(t) , \quad (19)$$

$$\Delta X_{\text{NE}}(t) = X_{\text{NE}}^{\max}(t) - X_{\text{NE}}^{\min}(t) , \quad (20)$$

for both electrodes. The theoretical capacities in actual stoichiometry range for positive and negative electrodes ( $C_{\text{PE}}$  and  $C_{\text{NE}}$ ) are defined as

$$C_{\text{PE}}(t) = \frac{C_{\text{cell}}(t)}{\Delta X_{\text{PE}}(t)} , \quad (21)$$

$$C_{\text{NE}}(t) = \frac{C_{\text{cell}}(t)}{\Delta X_{\text{NE}}(t)} , \quad (22)$$

where  $C_{\text{cell}}$  is the cell capacity calculated from the pOCV curve used for electrode balances analysis. Equations (19)-(22) are time-dependent because stoichiometric ranges and cell capacity change with aging. For a fresh cell, the equations above are redefined by adding the superscript "0" to indicate that all values address the initial values as follows:

$$C_{\text{PE}}^0 = \frac{C_{\text{cell}}^0}{\Delta X_{\text{PE}}^0} , \quad (23)$$

$$C_{\text{NE}}^0 = \frac{C_{\text{cell}}^0}{\Delta X_{\text{NE}}^0} . \quad (24)$$

We assumed that there was no LAM for a fresh cell. Therefore, the LAM of an aged cell at a given time  $t$  was defined as the following:

$$Q_{\text{LAM,PE}}(t) = C_{\text{PE}}^0 - C_{\text{PE}}(t) , \quad (25)$$

$$Q_{\text{LAM,NE}}(t) = C_{\text{NE}}^0 - C_{\text{NE}}(t) . \quad (26)$$

### 3.7.2.2 Loss of lithium inventory (LLI)

The effect of LLI is observed as a shift of the two half-cell curves with respect to each other. In order to develop a quantitative description, the charge content of the two electrodes  $Q_{\text{PE}}$ ,  $Q_{\text{NE}}$  are defined according to

$$Q_{\text{NE}}(t) = X_{\text{NE}}(t)C_{\text{NE}}(t) , \quad (27)$$

$$Q_{\text{PE}}(t) = X_{\text{PE}}(t)C_{\text{PE}}(t) . \quad (28)$$

We assume that the cell is manufactured with a fully lithiated positive electrode ( $X_{\text{PE}}^{\text{max}} = 1$ ,  $Q_{\text{PE}}^0 = C_{\text{PE}}^0$ , here: LiFePO<sub>4</sub>) and a fully delithiated negative electrode ( $X_{\text{NE}}^{\text{min}} = 0$ ,  $Q_{\text{NE}} = 0$ , here: pure graphite C<sub>6</sub>). We assume that LLI only occurs at the negative electrode, resulting from SEI formation and irreversible plating. With these assumptions, the NE lithium stoichiometry at an arbitrary time is given as

$$X_{\text{NE}}(t) = \frac{Q_{\text{NE}}(t)}{C_{\text{NE}}(t)} = \frac{Q_{\text{cell}}(t) - Q_{\text{LLI}}(t)}{C_{\text{NE}}(t)} , \quad (29)$$

and the PE lithium stoichiometry is given as

$$X_{\text{PE}}(t) = \frac{Q_{\text{PE}}(t)}{C_{\text{PE}}(t)} = \frac{C_{\text{PE}}^0 - Q_{\text{cell}}(t)}{C_{\text{PE}}(t)} . \quad (30)$$

Here,  $Q_{\text{cell}}(t)$  is the total charge throughput of the cell until time  $t$ . In other words, for a fully charged cell  $Q_{\text{cell}} = C_{\text{cell}}$  and for a fully discharged cell  $Q_{\text{cell}} = 0$ . The combination of equations (29) and (30) by eliminating  $Q_{\text{cell}}(t)$  results in

$$Q_{\text{LLI}}(t) = C_{\text{PE}}^0 - X_{\text{PE}}(t)C_{\text{PE}}(t) - X_{\text{NE}}(t)C_{\text{NE}}(t) . \quad (31)$$

This equation can be calculated with an arbitrary pair of  $X_{\text{PE}}(t)$ ,  $X_{\text{NE}}(t)$ . Due to the better identifiability of  $X_{\text{PE}}$  for a full cell (cf. Section 3.7.2.3), we typically used stoichiometric pair at 100 % SOC, resulting in

$$Q_{\text{LLI}}(t) = C_{\text{PE}}^0 - X_{\text{PE}}^{\text{min}}(t)C_{\text{PE}}(t) - X_{\text{NE}}^{\text{max}}(t)C_{\text{NE}}(t) . \quad (32)$$

As a result, equations (25), (26) and (32) allow to quantify LAM<sub>PE</sub>, LAM<sub>NE</sub>, and LLI by using parameters acquired from electrode balances analysis of a fresh cell (results indicated with superscript <sup>0</sup>) and the same cell after aging for the duration of time  $t$ . Additionally, by using the aforementioned assumptions, for any given SOC, we can calculate the corresponding electrode stoichiometries as

$$X_{\text{PE}}(\text{SOC}) = X_{\text{PE}}^{\text{min}} + (1 - \text{SOC}) \cdot \Delta X_{\text{PE}} , \quad (33)$$

$$X_{\text{NE}}(\text{SOC}) = X_{\text{NE}}^{\text{min}} + \text{SOC} \cdot \Delta X_{\text{NE}} . \quad (34)$$

### 3.7.2.3 Parameter identifiability

The framework derived in the two previous sections allows the determination of  $LAM_{PE}$ ,  $LAM_{NE}$ , LLI by using parameters  $X_{PE}^{\min}$ ,  $X_{PE}^{\max}$ ,  $X_{NE}^{\min}$ ,  $X_{NE}^{\max}$ ,  $C_{cell}$ . However, in many practical cases, not all parameters are identifiable. Therefore, further assumptions were necessary to eliminate the unidentifiable parameters. These assumptions were based on experimental data. For example, in Figure 11, it is noticeable that the NE lithium stoichiometry is in a potential plateau region with a full cell, while the PE half-cell curve of the cathode shows a strong gradient. On the other hand, the NE half-cell curve exhibits a strong gradient for an empty cell, and the PE is adjacent to the voltage plateau, spanning nearly the whole PE stoichiometry. Therefore, the identifiability of  $X_{NE}$  is best for an empty cell and that of  $X_{PE}$  for a full cell. Still, as the NE half-cell potential curve has several steps, the identifiability of the NE lithium stoichiometry range remains good.

Furthermore, as a result of ongoing LLI, the maximum stoichiometry of the positive electrode  $X_{PE}^{\max}$  shifts to lower values in time. For the  $LiFePO_4$  electrode of the cell investigated here,  $X_{PE}^{\max}$  shifts into the large voltage plateau where the voltage is nearly constant (cf. Figure 11(b)). Within this plateau,  $X_{PE}^{\max}$  is practically unidentifiable because the plateau voltage can be associated with a wide range of Li stoichiometries. Thus, we have to exclude  $X_{PE}^{\max}$  from the optimization problem. This, in turn, makes the identification of  $LAM_{PE}$  impossible. Therefore, we assumed that the LFP positive electrode does not undergo LAM for the degradation modes analysis.

$$LAM_{PE} = 0 . \quad (35)$$

Accordingly, we assume that the theoretical capacity of PE does not change:

$$C_{PE} = C_{PE}^0 . \quad (36)$$

Under this assumption, the maximum stoichiometry at any given time  $X_{PE}^{\max}(t)$  can be calculated according to:

$$X_{PE}^{\max}(t) = X_{PE}^{\min}(t) + \frac{C_{cell}(t)}{C_{PE}^0} . \quad (37)$$

Furthermore, as mentioned earlier, we recorded  $C_{cell}$  value directly from the experimental data from the capacity of the pOCV curves. The number of optimization parameters was reduced by two with these two assumptions. As a consequence, the parameter set to be determined for solving the optimization problem was reduced to  $p = \{X_{NE}^{\min}, X_{NE}^{\max}, X_{PE}^{\min}\}$ .

These parameters are sufficient to calculate  $LAM_{NE}$  and LLI from equations (26) and (32), respectively.

## 4 RESULTS AND DISCUSSION

---

### 4.1 ELECTRICAL AND STRUCTURAL CHARACTERIZATION

The first step in investigating the aging behavior of large-format LFP cells was to perform a detailed electrical and structural investigation of two different commercial LFP cells (Sinopoly and Calb cells), as described in Section 3.4. The aim of this step is to gather detailed electrical and structural parameters of the commercial cells, along with electrode balances analysis of the test data, to create a complete characteristics database of a fresh cell as a reference for aging experiments.

Ideally, fresh cells (never used or not stored for a long time) from the same production batch should be used for detailed initial characterization to ensure that aging or inhomogeneities do not affect the results. Unfortunately, there was no information on as-delivered Sinopoly or Calb cells about their production date or batch numbers. Therefore, at the start of experiments, we assumed that the cells from the same shipment had similar production and aging history because no other criteria were available to classify cells.

The results presented in this chapter were published in *Energy Technology*: M. C. Yagci, R. Behmann, V. Daubert, J. A. Braun, D. Velten, and W. G. Bessler, “Electrical and Structural Characterization of Large-Format Lithium Iron Phosphate Cells Used in Home-Storage Systems,” *Energy Technology* 9 (6), 2000911 (2021) [42]. The electrical characterization tests were performed by me with the support of Jonas Touzri and René Behmann. Cell opening was performed by me with the support of Viktor Daubert as a part of his Bachelor’s thesis at Offenburg University of Applied Sciences under my co-supervision with Wolfgang G. Bessler [107]. Sample preparation and investigation of samples at LM and SEM were performed by me with the support of René Behmann as a part of his Bachelor’s thesis at Offenburg University of Applied Sciences under the supervision of Wolfgang G. Bessler and Dirk Velten [108]. Jonas A. Braun supported electrode balancer analysis. Microscopy investigations were performed by me with the assistance of Pascale Müller. Hanhee Kim supported the development of thermodynamic data on active materials. The article was written by myself with the editing of Wolfgang G. Bessler, except for the experimental methodology of the tests and analyses performed by co-authors who wrote their respective sections.

## 4.1.1 Electrical characterization

### 4.1.1.1 Capacity tests

As presented in Section 2.3.2, capacity change in time is considered the primary indicator of cell aging. Therefore, the first step of the aging investigation was the measurement of cell capacity using the test protocol described in Section 3.4.1.2. The measurement results of the 28 Sinopoly cells (to be chosen for BESS aging experiments) and 28 Calb cells in the form of cell voltage as a function of charge throughput are shown in Figure 12. In this representation, the lower curves represent discharge, progressing in time from left to right, while the upper curves represent charge, progressing from right to left. Here and in the following figures and tables, the left column shows results from the Sinopoly cells, while the right column shows results from the Calb cells. Although both cell types have the same chemistry, their cut-off voltages, as specified by the manufacturer, are significantly different (cf. Table 2), leading to different curve shapes, as evident from Figure 12. All individual cells show a strong scatter in their measured capacity for both cell types. For Sinopoly cells, CC discharge capacities range from 158.9 to 195.8 Ah, with an average of 169.5 Ah and a standard deviation of 11.9 Ah. For Calb cells, the scatter is less pronounced, with CC discharge capacities ranging from 188.9 to 199.2 Ah with an average of 195.9 Ah and a standard deviation of 2.4 Ah. Notably, all Calb cells have capacities above the nominal capacity (180 Ah), which is not the case for Sinopoly. The reason for the large scatter of the Sinopoly cells is unclear. Following the delivery, all cells were stored and treated in-house in the same way; therefore, the scatter must be assigned either to production itself (e.g., different production batches) or cell history between production and delivery, which is unknown to us.

The scatter of the cell capacity is significant in both cases. When cells are integrated into BESS, they are typically connected in series to increase voltage to a level suitable for inverters. The capacity scatter leads to a permanent de-balancing of the cells in the system, potentially leading to accelerated aging and posing a challenge to balancing systems. These effects are investigated in detail in Section 4.2.

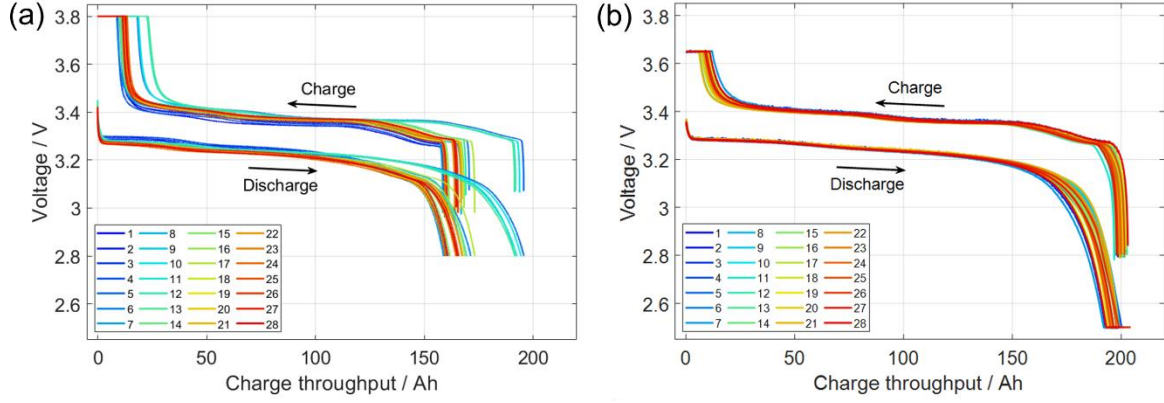


Figure 12: Discharge/charge curves of 28 Sinopoly cells (a) and 28 Calb cells (b). The current rates of the CC phase are 0.25C for Sinopoly and 0.28C for Calb at 20 °C ambient temperature. The lower branches represent discharge (time progresses from left to right), while the upper branches represent charge (time progresses from right to left). The charge throughput ( $x$  scale) is zero for a fully-charged cell. The test protocol is given in Section 3.4.1.2.

#### 4.1.1.2 Rate capability and temperature performance tests

According to the results of the capacity tests, one cell of each type close to median capacity (Sinopoly cell #28 with 164.9 Ah capacity, and Calb cell #6 with 195.6 Ah capacity) was selected for rate capability and temperature performance tests defined in Section 3.4.1.3, which consisted of C-rate tests (recording of discharge/charge curves at different currents) at different ambient temperatures (5, 20, 35 °C). The results of the tests are shown in Figure 13. Here, the same representation is used as in Figure 12; cell voltage is plotted as a function of charge throughput. The lower branches represent discharge, and the upper branches charge. This representation has the advantage that overpotentials are easily visualized. Charge and discharge overpotentials are indicated in panel (a). The overpotential  $\eta$  is defined [116,117] as the difference between operation voltage  $V$  and equilibrium voltage  $V^{\text{eq}}$ ,

$$\eta = V - V^{\text{eq}} . \quad (38)$$

The overpotential is (per this definition) negative for battery discharge (where  $V < V^{\text{eq}}$ ) and positive for battery charge (where  $V > V^{\text{eq}}$ ). An increasing gap between discharge and charge branches means increasing overpotentials.



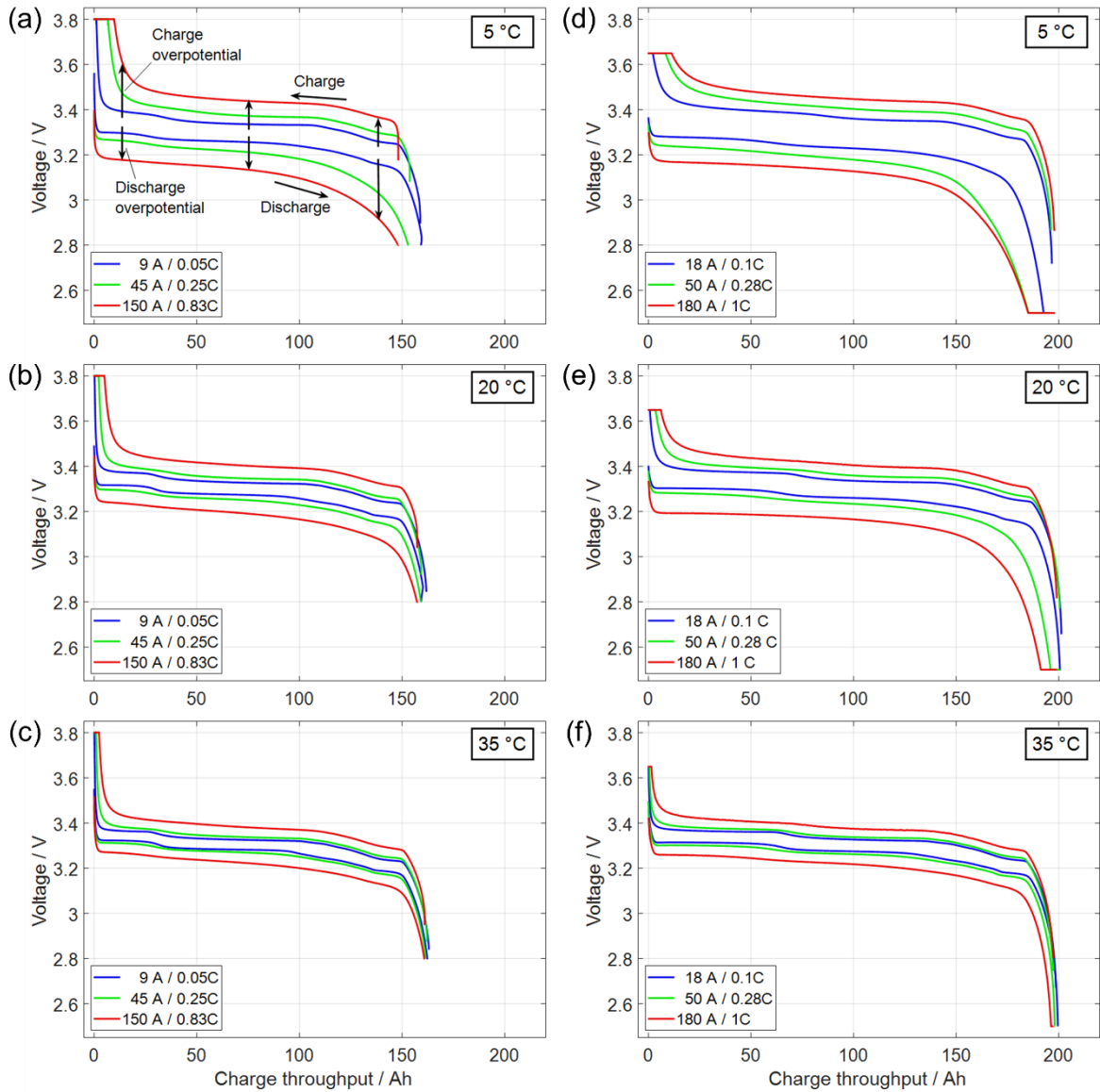


Figure 13: Discharge/charge curves of Sinopoly (a, b, c) and Calb (d, e, f) cells measured with three current rates representing low, medium, and high current rates. The measurements were repeated at three different ambient temperatures (5 °C, 20 °C, 35 °C). The lower branches represent discharge (time progresses from left to right), while the upper branches represent charge (time progresses from right to left). The charge throughput ( $x$  scale) is zero for a fully-charged cell. The test protocol is given in Section 3.4.1.3.

As shown in Figure 13, both cells, Sinopoly (left) and Calb (right), show qualitatively the same behavior, which can be summarized as follows. (i) C-rate increase leads to higher overpotentials, as visible in the increasing gap between discharge and charge branches. This typical behavior of electrochemical cells is due to increasing ohmic, electrochemical, and transport losses [116,117]. (ii) As a consequence of the increased overpotential, an increase

in the C-rate leads to a decrease in the CC-dischargeable capacity, known as the “capacity-rate effect” [50]. However, for the relatively low currents investigated here ( $\leq 1C$ ), the effect is small compared to other cell types [118]. (iii) Increasing temperature has a similar effect as decreasing the C-rate, both on capacity and overpotential. As a result, using the Calb cell as an example, 5 °C / 0.1C shows a very similar curve as 35 °C / 1C. (iv) The overpotentials show an asymmetric behavior: during discharge, overpotentials increase towards low SOC, while during charge, overpotentials increase towards high SOC. This asymmetry is indicated by the arrows in panel (a). It is pronounced for low temperatures and high C-rates. A similar asymmetry has been observed in cells with NCA cathode [119], although the mechanism may differ in the present LFP cells.

Studying heat losses during cycling is interesting because they affect system-level thermal management strategies and lower energy efficiency. Figure 14 shows measured temperature differences between the cell and the ambient as a function of time for different C-rates and ambient temperatures defined as

$$\Delta T(t) = T_{\text{cell}}(t) - T_{\text{ambient}} \quad (39)$$

The cell temperature,  $T_{\text{cell}}$ , was measured at the cell surface with a thermocouple. The ambient temperature,  $T_{\text{ambient}}$ , is the setpoint of the climate chamber. During cycling, the temperature difference between the cell and the ambient ( $\Delta T$ ) depends on the C-rate and ambient temperature. It shows a distinct temporal behavior due to irreversible and reversible heating. The heating power  $\dot{Q}$  within an electrochemical cell is given as [120]

$$\dot{Q} = -I \cdot \eta - I \cdot (T - T^0) \cdot \frac{dV^{\text{eq}}}{dT} \quad (40)$$

where the first term on the right-hand side represents irreversible heating (always positive) and the second term reversible (entropic) heating (positive or negative, depending on signs of current and  $dV^{\text{eq}}/dT$ ). The overpotentials  $\eta$  are highest at low temperatures (cf. Figure 13), causing high irreversible heating (first term). Therefore, at low ambient temperatures (5 °C)  $\Delta T$  is highest, and at high ambient temperatures (35 °C)  $\Delta T$  is generally the lowest. At low currents, the contribution of the reversible heating can become significant, causing non-monotonous temperature curves. Note that, particularly at low currents,  $\Delta T$  is well below 1 °C and the measurements may additionally be influenced by small fluctuations in the ambient temperature.

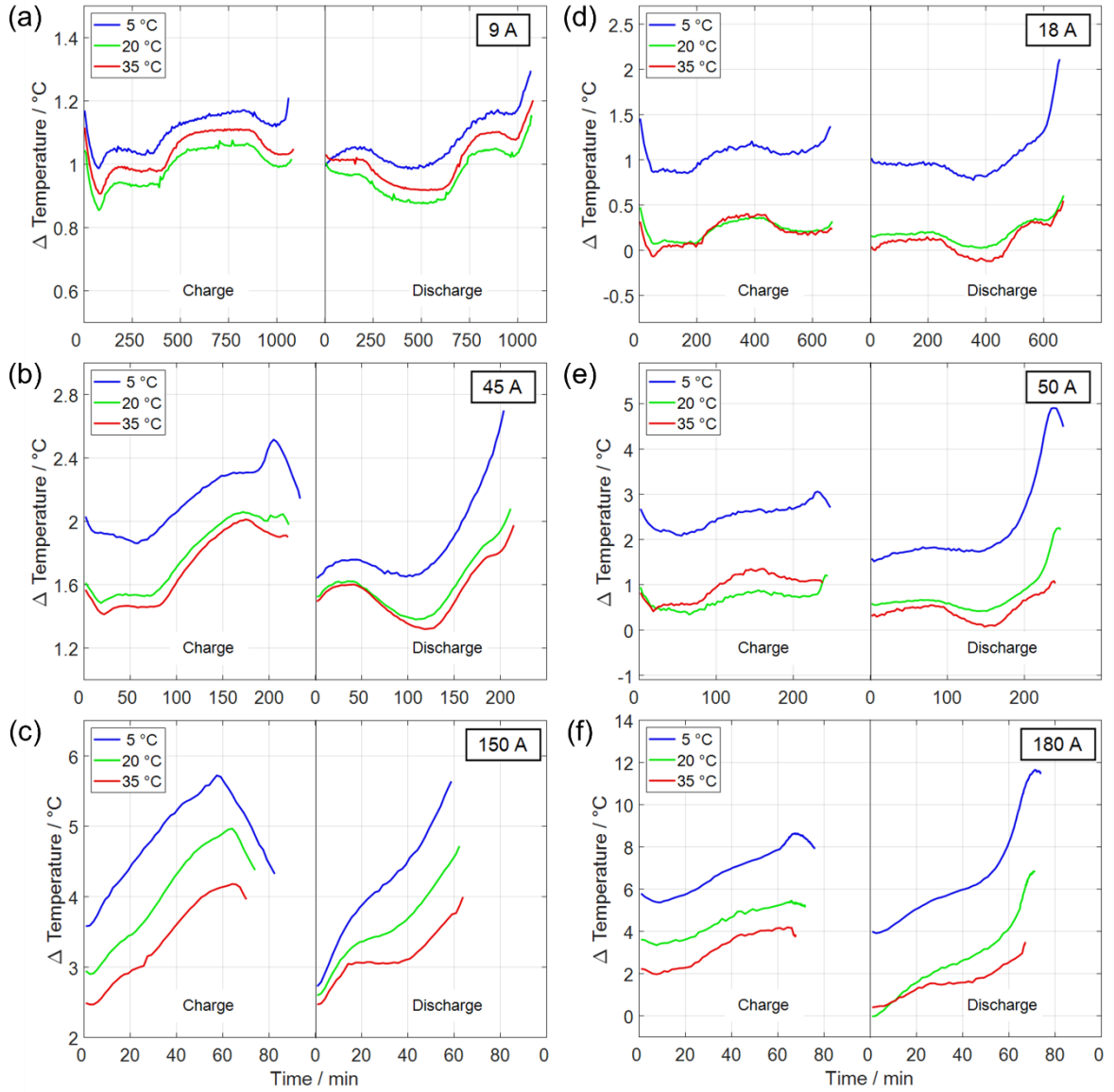


Figure 14: Difference between cell surface temperature ( $T_{\text{cell}}$ ) and ambient temperature ( $T_{\text{ambient}}$ ) as function of time for Sinopoly (a, b, c) and Calb (d, e, f) cells during rate capability and temperature performance tests. Test currents are indicated in the top right corner of the plots, and ambient temperatures are given in the legends. The test protocol is given in Section 3.4.1.3.

Energy efficiency is a representation of overall system performance. Low energy efficiency corresponds to high energy losses. In the case of BESS, low energy efficiency means a lower portion of charged energy is available for discharge, which leads to lower economic feasibility of the overall system. To investigate the energetic performance of the Sinopoly and Calb cells under investigation, the energy efficiency  $\eta_{\text{energy}}$  both cells at different C-rates and temperatures are calculated according to Eq. (12). In practice, the battery cyclers record the

test data (e.g., voltage, current, temperature) in certain intervals. Therefore, the energy efficiency calculation is performed with the discrete integral

$$\eta_{\text{energy}} = \frac{E_{\text{discharge}}}{E_{\text{charge}}} = \frac{\sum_{\text{discharge}} I_n \cdot V_n \cdot \Delta t}{\sum_{\text{charge}} I_n \cdot V_n \cdot \Delta t} = \frac{\sum_{\text{discharge}} V_n \cdot \Delta Q_n}{\sum_{\text{charge}} V_n \cdot \Delta Q_n}, \quad (41)$$

where  $I_n$ ,  $V_n$ , and  $Q_n$  are the  $n$ th measured current, voltage, and charge throughput, respectively. The results are shown in Figure 15. Both cell types show high efficiencies above 88 % for all investigated conditions, reaching up to almost 99 % for the Calb cell at 35 °C. The efficiency of the Sinopoly cell shows considerably less dependency on ambient temperature than that of the Calb cell. At low temperatures (5 °C), the efficiency is higher for the Sinopoly cell. As efficiencies below unity are due to irreversible heat losses,  $\eta_{\text{energy}}$  is indirectly related to the cell temperature increase: Conditions with observed high  $\Delta T$  (i.e., low ambient temperature and/or high C-rate cf. Figure 14 panels (c) and (f)) were also observed to have low  $\eta_{\text{energy}}$  (Figure 15).

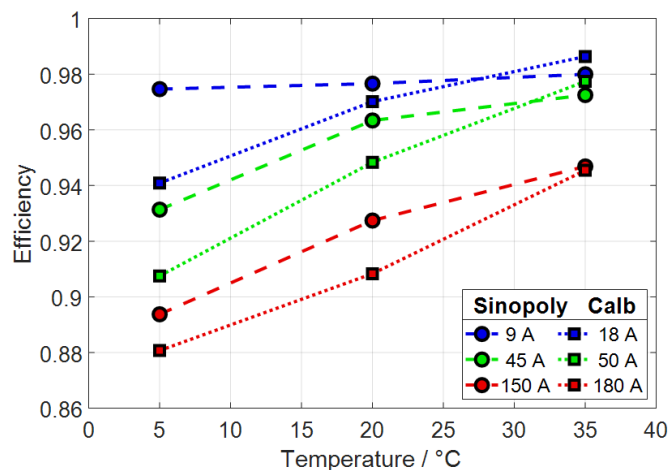


Figure 15: Discharge/charge energy efficiency  $\eta_{\text{energy}}$  of Sinopoly (circles) and Calb (squares) cells calculated from the rate capability test results at three different temperatures (5 °C, 20 °C, 35 °C). The test protocol is given in Section 3.4.1.3.

#### 4.1.2 Structural characterization

The structural characterization consists of two main stages: determination of internal geometrical properties of cell components and investigation of electrode microstructure. One cell of each type was opened in an argon-filled glovebox for structural characterization. For Calb, a fresh cell (as delivered) was used. For Sinopoly, lacking availability of fresh cells at the time of the experiment, one of the cells used for the continuous temperature-controlled

cycling test (cf. Section 3.5.2) is opened (after performing 897 cycles at 150 A over two years) at 89.6% SOH. The results of structural characterization could show differences due to the different aging status of the cells. The differences will be discussed later in this section.

#### 4.1.2.1 Internal geometry

Following the activation and capacity test, the Sinopoly and Calb cells were opened in the glovebox following the procedure in Section 3.4.2. Pictures of the cells after cutting and removing the lower part of the casing are shown in Figure 16. Both cell types have a similar internal design. Both cells consist of two separate electrode stacks wrapped in a plastic foil and taped together. The current collector tabs are connected to the outer terminals. Both cells have a pressure vent, but no positive temperature coefficient (PTC) connector or other safety features could be identified.

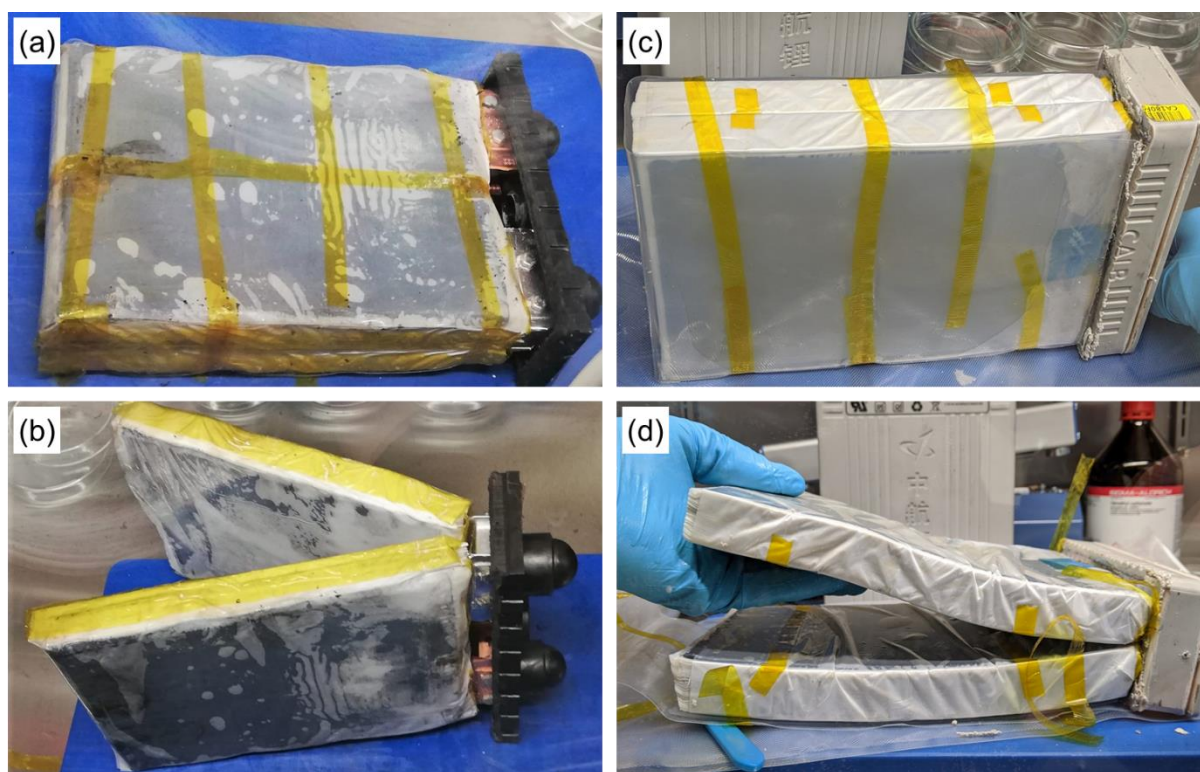


Figure 16: Pictures of the interior structure of Sinopoly (a, b) and Calb (c, d) cells opened in an argon-filled glovebox.

The current collector tabs were cut, and the stacks were unwrapped for further disassembly. For each stack, a single long separator sheet was observed to be arranged in Z form between the stacked electrode sheets (no winding). Here and in the following, we use the term “electrode sheet” for a current collector foil coated on both sides with electrodes. All electrode

sheets, including the outermost, were coated from both sides. Pictures of the sheets are shown in Figure 17. The electrode and separator sheets of the (aged) Sinopoly cell qualitatively appear to be used more than those of the (fresh) Calb cell.

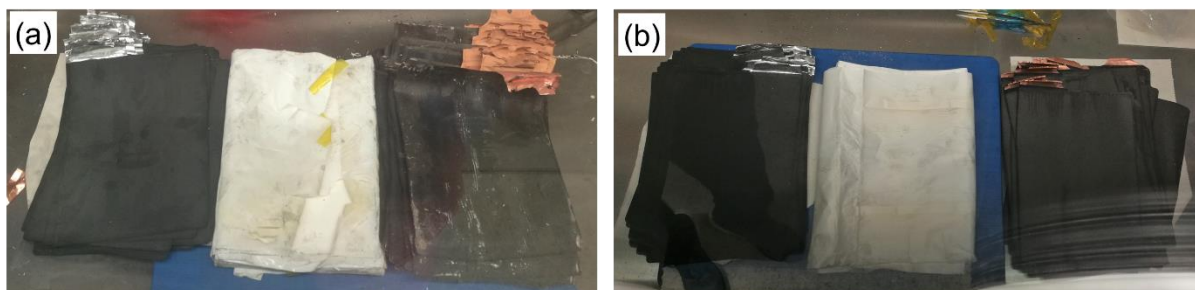


Figure 17: Positive electrode sheets (left), separator sheet (middle), and negative electrode sheets (right) of Sinopoly (a) and Calb (b) cells.

Details of the geometrical and weight properties of all components are given in Table 18. Both cells show a similar, but not identical, design. Both cells contain 146 negative and 144 positive electrode sheets (counting both stacks). There is a clear anode overhang [121], with the anode having a larger area than the cathode by 4.9 % (Sinopoly) and 5.7 % (Calb).

Table 18: Internal geometrical properties and component masses of the two cell types.

Cell type	Sinopoly			Calb		
	NE	Separator	PE	NE	Separator	PE
Height/cm	22.0	23.9	21.5	22.5	23.5	22.0
Width/cm	15.9	2382	15.4	15.7	2431	15.3
Thickness (single sheet)/ $\mu\text{m}$	128.8	44.1	178.7	140.7	31.6	176.6
Thickness (single current collector)/ $\mu\text{m}$	15.3	-	26.1	15.6	-	25.6
Thickness (single electrode)/ $\mu\text{m}$	56.8	-	76.3	62.6	-	75.5
Area (single sheet)/ $\text{cm}^2$	348.0	384.8	329.3	350.5	379.5	334.1
Volume (single sheet)/ $\text{cm}^3$	4.48	1.69	5.89	4.93	1.12	5.90
Number of sheets	146	2	144	146	2	144
Total area/ $\text{m}^2$	10.16	11.39	9.485	10.24	11.43	9.623
Total volume/ $\text{cm}^3$	654.4	502.3	847.5	720.3	361.1	849.9
Total mass electrodes/g	906	-	1644	1190	-	1907
Mass loading electrodes/ $\text{mg}/\text{cm}^2$	8.92	-	17.3	11.6	-	19.8
Total mass (sheet)/g	1560	369.2	1997	1331	308.5	1976
Total mass current collection*/g	654	-	353	141	-	69

\* includes the aluminum and copper foils, tab collectors, and terminals

The mass distribution of the cell components is shown in Figure 18. In both cell types, the positive electrode is the dominating component, providing around one-third of the whole cell mass, followed by the casing (around one-quarter) and the negative electrode (around one-fifth of the cell mass). The significant contribution of the casing is remarkable. Both cells have a PP hard case with significant thicknesses of 5.3 mm (Sinopoly) and 6.2 mm (Calb). The manufacturers seem to accept the lowered specific energy resulting from the massive housing at the benefit of high mechanical robustness.

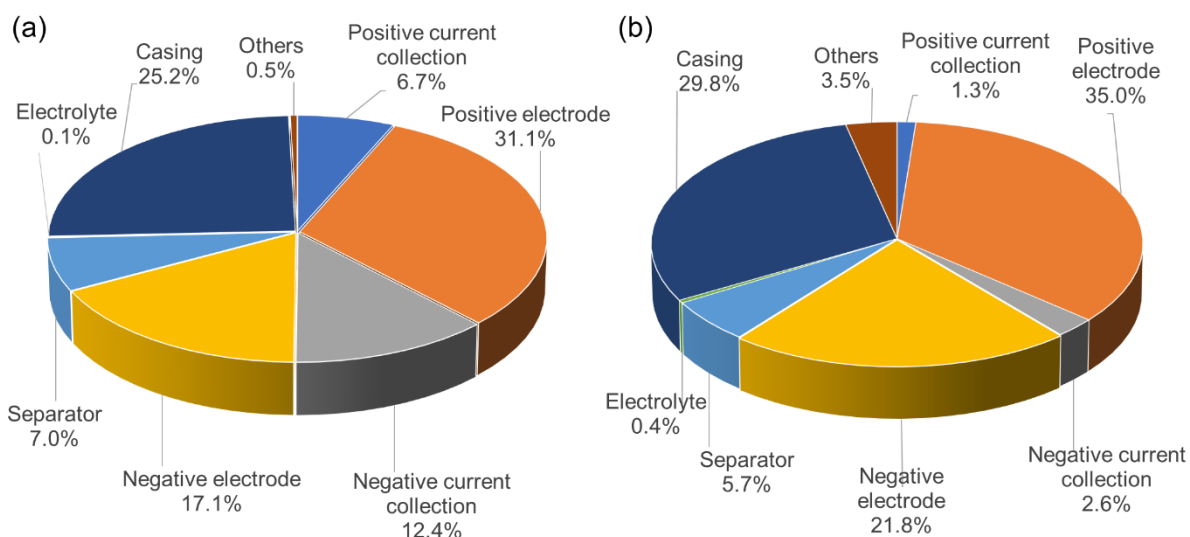


Figure 18: Mass distribution of the components of Sinopoly (a) and Calb (b) cells. “Electrolyte” refers to the free liquid left inside the casing after removing the electrode stacks (electrolyte soaked in the porous electrodes could not be measured). “Current collection” includes metal foils, tab collectors, and terminals. “Others” refers to plastic foils and tapes wrapped around the electrode stacks, screws of the tab collection system, and seals.

#### 4.1.2.2 Electrode microstructure

In order to characterize the electrode microstructure, both electrode sheets of both cell types were investigated via LM (providing a lower-resolution overview) and SEM (providing high-resolution results and allowing chemical analysis via EDX). The results of the LM are shown in Figure 19. All samples were investigated in cross-sectional view (cf. Section 3.4.2 for sample preparation). The left images (panels (a-d)) show results from the Sinopoly cell, the right images (panels (e-h)) from the Calb cell, and each electrode is shown with lower and higher resolution. All micrographs show the current collector in the center as a bright bar coated with porous composite electrodes on both sides. The positive electrodes (panels (a), (b), (e), and (f)) have a compact appearance. Granular structures on both sides of the current collector may be present; however, the features seem to be below the resolution limit of the LM. The negative electrodes (panels (c), (d), (g), and (h)) show a clear composite appearance with granular features in the 5-10  $\mu\text{m}$  range. The chemical composition of granular structures is presented in EDX results. The thicknesses for the Sinopoly cell are 176  $\mu\text{m}$  for the positive electrode sheet and 126  $\mu\text{m}$  for the negative electrode sheet. The thicknesses for the Calb cell are 178  $\mu\text{m}$  for the positive electrode sheet and 137  $\mu\text{m}$  for the negative electrode sheet. The thickness values measured from the LM are consistent with the ones measured by thickness



gauge within <15 % deviation (cf. Table 18). The samples might be thicker due to the absence of applied pressure by the thickness gauge and the removal of the electrolyte during the washing procedure of the samples.

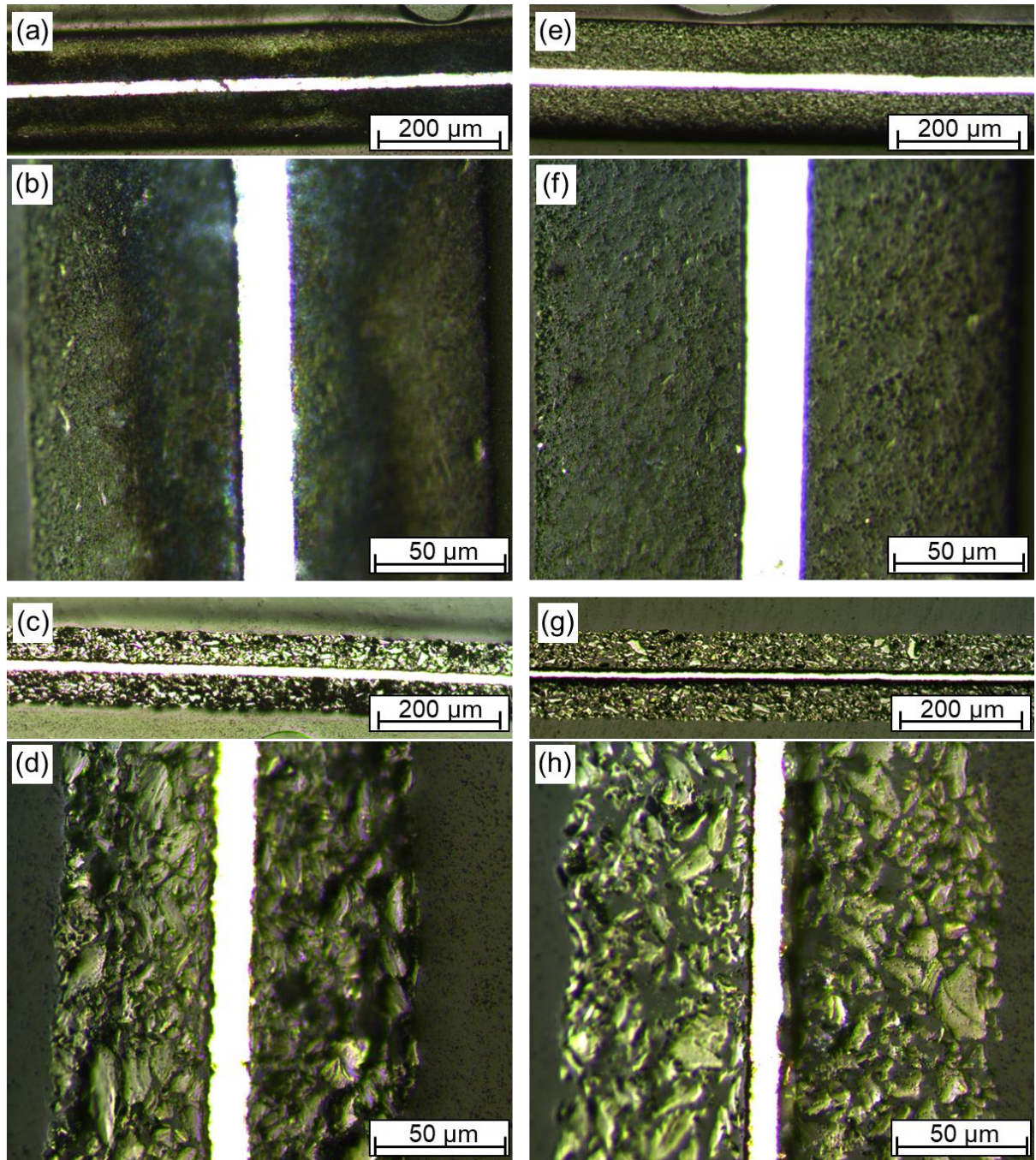


Figure 19: Light microscopy investigations of polished electrodes (cross-section): Sinopoly positive electrode (a, b) and negative electrode (c, d), Calb positive electrode (e, f) and negative electrode (g, h). Sample holders are visible close to the upper border of panels (a) and (e).

Electron micrographs of the samples are shown in Figure 20. Here, each electrode is shown both in the top and cross-sectional views. For the positive electrodes (panels (a), (b), (e), and (f)), the granular structure of the electrode is clearly visible compared to LM images due to the significant resolution advantage of SEM. The top views (panels (a) and (e)) show irregularly shaped but roughly spherical particles that are in the 0.4  $\mu\text{m}$  diameter range for the Sinopoly and in the 0.5  $\mu\text{m}$  diameter range for the Calb cell. The particles in the Calb cell (e) appear more densely packed and agglomerated than in the Sinopoly cell (a). The low density of the Sinopoly negative electrode can be due to proposed electrochemical milling by aging [88]. The cross-sectional views (panels (b) and (f)) show a combination of fine and occasional larger particles. The electrodes seem to have slightly detached from the right side of the current collector, probably a consequence of sample preparation. For the negative electrodes (panels (c), (d), (g), and (h)), the top views (panels (c) and (g)) reveal irregularly shaped, flake-like particles that are in the 10  $\mu\text{m}$  diameter range for the Sinopoly and in the 15  $\mu\text{m}$  diameter range for the Calb cell. The cross-sectional view (panels (d) and (h)) does not provide a very good contrast between the active material particles and the resin-filled porosity. Still, the irregularity of the particle shapes and significant size distribution is evident for both cell types. The Sinopoly electrode (d) seems closer packed with smaller porosity than the Calb electrode (h). The thicknesses measured from the cross-sectional views of the Sinopoly cell are 182  $\mu\text{m}$  for the positive electrode sheet and 128  $\mu\text{m}$  for the negative electrode sheet. The thicknesses measured from the cross-sectional views of the Calb cell are 181  $\mu\text{m}$  for the positive electrode sheet and 139  $\mu\text{m}$  for the negative electrode sheet. The thickness values are consistent with those determined by LM.

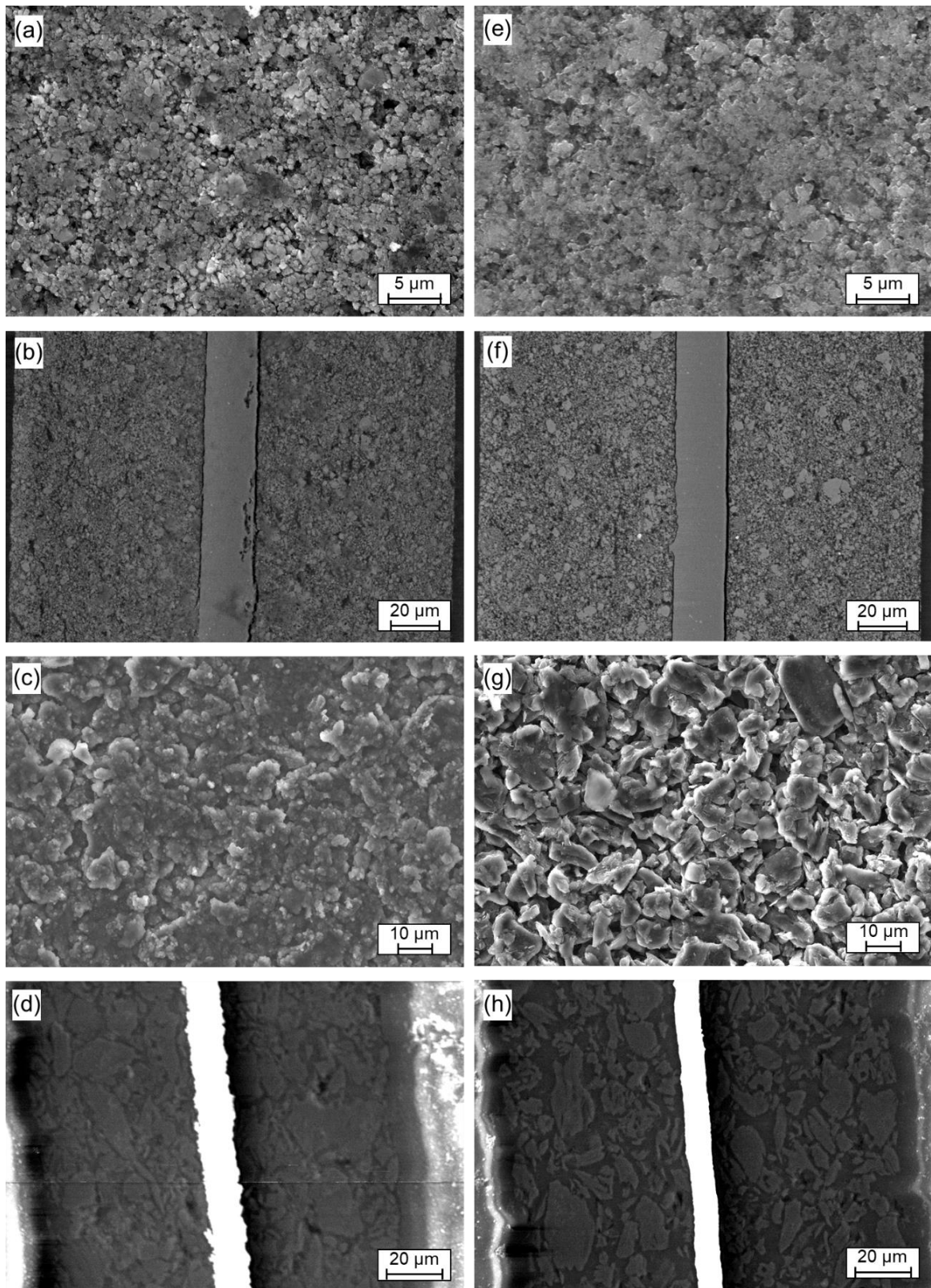


Figure 20: Scanning electron microscopy investigation: Sinopoly positive electrode in top-view (a) and cross-sectional view (b), negative electrode in top view (c) and cross-sectional view (d); Calb positive electrode in top view (e) and cross-sectional view (f), negative electrode in top view (g) and cross-sectional view (h).

EDX was used to probe the chemical composition of the electrodes from top-view micrographs. The results are given in Table 19 for all four investigated electrodes. The results identify LFP and graphite as active materials in both cell types, as those elements (Fe, P, O at the positive and C at the negative electrodes) are the majority species identified in the EDX signal. Both positive electrodes also show a significant amount of carbon, typically used as a conductive additive in LFP electrodes [13,122]. Both Sinopoly electrodes also show a non-negligible fluorine signal, probably solid electrolyte interphase (SEI) components originating from electrolyte degradation [94] – note that these electrodes were harvested from an aged cell. Consequently, the (fresh) Calb cell shows no fluorine at the positive electrode and only a tiny amount at the negative electrode. The oxygen observed at both negative electrodes may similarly result from SEI components. The remaining elements given in Table 19 are negligible or below detection limits. In particular, no sign of other blended active materials (such as silicon at the negative electrodes or cobalt at the positive electrodes) can be identified. Notably, no yttrium was found, despite the claim of the Sinopoly datasheet to use  $\text{LiFeYPO}_4$  (cf. Appendix 6.2.2). The EDX results confirm that the chemistry of both cell types is LFP/graphite.

Overall, the combined LM, SEM, and EDX investigations show that both cell types have similar, but not identical, electrode properties in terms of particle size and shape, electrode morphology, and materials chemistry.

Table 19: Results of EDX analysis. All values in percent. Missing values mean the material amount is below the detection limit.

	<b>Sinopoly PE</b>	<b>Sinopoly NE</b>	<b>Calb PE</b>	<b>Calb NE</b>
<b>Iron, Fe</b>	26.74	-	26.12	-
<b>Phosphorus, P</b>	14.73	1.23	13.47	0.18
<b>Oxygen, O</b>	35.17	18.24	36.65	6.02
<b>Aluminum, Al</b>	-	0.02	-	-
<b>Carbon, C</b>	19.92	58.25	23.07	89.18
<b>Cadmium, Cd</b>		0.01		
<b>Copper, Cu</b>	-	1.05	-	1.11
<b>Fluorine, F</b>	2.99	20.62	-	3.31
<b>Silicon, Si</b>	0.03	0.23	-	0.19
<b>Sodium, Na</b>	-	-	-	0.03
<b>Sulfur, S</b>	0.20	0.36	-	-
<b>Cobalt, Co</b>	-	-	0.03	-
<b>Vanadium, V</b>	0.24	-	-	-
<b>Iridium, Ir</b>			0.44	
<b>Titanium, Ti</b>	-	-	0.21	-
<b>Yttrium, Y</b>	-	-	-	-
<b>Identified material</b>	<b>LFP</b>	<b>Graphite</b>	<b>LFP</b>	<b>Graphite</b>

#### 4.1.3 Electrode balances

The last step of the cell characterization was determining the lithium stoichiometry ranges in which the electrodes of the two cell types are operated. To this goal, the electrode balances analysis method (cf. Section 3.7.1) was applied to the electrical and structural characterization results using the optimization tool mentioned earlier [97].

The electrode balances analysis results are shown in Figure 21. The left and right panels correspond to Sinopoly and Calb cells, respectively. Panels (a) and (e) show measured pOCV (C/100 for Sinopoly cell, C/50 for Calb cell) curves and the synthetic curves after optimization. For both cell types, the simulation matches the experimental data accurately. The precision of the simulation results is also confirmed in the differential voltage analysis shown in panels (b) and (f). The small but characteristic steps in the voltage curves were well reproduced by the simulation. The characteristic steps appear at different charge throughputs for Sinopoly and Calb cells – a clear sign of the differing anode balance. As shown

from the deconvolution presented as dashed lines in panels (b) and (f), these steps can be fully assigned to the graphite anode, while the LFP cathode dominates the curve only at very low charge throughput. Panels (c) and (g) show the graphite anode half-cell potential curves. The literature input is shown as a thin line, while the stoichiometry range used in the cells during cycling is included as a bold line. The two cell types show different behavior, with the Sinopoly cell (panel (c)) showing a smaller stoichiometry range than the Calb cell (panel (g)). Finally, panels (d) and (h) show the exact representation of the LFP cathode. The complete plateau range or even almost the complete stoichiometry range is used for cycling.

The quantitative results of the electrode balance analysis are given in Table 20. This table also includes the required input parameters. When electrode areas and thicknesses are known, as in the present study, the optimization output includes the volume fraction of active electrode material. These data are also given in Table 20, which provides a complete and self-consistent data set of chemical and structural parameters of the two cell types. These parameters provide the basis for future modeling and simulation investigations, both physicochemical continuum models (so-called pseudo-2D, P2D, or Newman-type models) [123,124] and semi-empirical equivalent circuit (EC) models [125].

From the point of view of cell manufacturing, it is interesting to quantify the loading of active materials. The electrode balance analysis allows us to deduce the area-specific active material loading  $m_{AM}^A$  (in mg/cm<sup>2</sup>) as

$$m_{AM}^A = \frac{m_{AM}}{A_e} = \frac{V_{AM} \cdot \rho_{AM}}{A_e} = \frac{V_e \cdot \varepsilon_{AM} \cdot \rho_{AM}}{A_e} = d_e \cdot \varepsilon_{AM} \cdot \rho_{AM} , \quad (42)$$

the usable electrode capacity  $C^A$  (in mAh/cm<sup>2</sup>) as

$$C^A = \frac{C_{cell}}{A_e} , \quad (43)$$

and the areal capacity  $C_{AM}^A$  (in mAh/cm<sup>2</sup>) as

$$C_{AM}^A = \frac{C^A}{\Delta X_{Li}} . \quad (44)$$

In these equations, AM stands for active material (graphite or LFP),  $m_{AM}$  is the total active material mass in the cell,  $A_e$  the active electrode area,  $V_{AM}$  the total volume of active material,  $\rho_{AM}$  the density,  $V_e$  the electrode volume,  $d_e$  the electrode thickness,  $\varepsilon_{AM}$  the volume fraction,  $C_{cell}$  the cell capacity, and  $\Delta X_{Li}$  the lithium stoichiometry range during cycling. The resulting values are given in Table 20. The areal capacities are in the range of 1.8–2.8 mAh/cm<sup>2</sup> and, therefore, lower than the 3–4 mAh/cm<sup>2</sup> values that Lin et al. [126] reported for “current”

lithium-ion batteries. The active materials mass loadings are 7.7–12.2 mg/cm<sup>2</sup>, less than the measured total mass loadings of 8.9–19.8 mg/cm<sup>2</sup> (cf. Table 18), indicating the significant contribution of inactive materials such as binder and conductive additives to the electrode mass.

Table 20: Electrode balance analysis results providing a self-consistent parameter set for negative electrode (NE) and positive electrode (PE) of Sinopoly and Calb cells.

Cell type	Sinopoly		Calb	
	NE	PE	NE	PE
Active material	Graphite	LFP	Graphite	LFP
Density/kg m <sup>-3</sup>	2270 [127]	3600 [128]	2270 [127]	3600 [128]
Molar mass of delithiated phase/g mol <sup>-1</sup>	72.1	150.8	72.1	150.8
Half-cell thermodynamic data	[112,113] (cf. Figure 21c)	[114,115] (cf. Figure 21d)	[112,113] (cf. Figure 21c)	[114,115] (cf. Figure 21d)
Active electrode area/m <sup>2</sup>	9.48		9.62	
Electrode thickness/m	56.7·10 <sup>-6</sup>	76.3·10 <sup>-6</sup>	62.6·10 <sup>-6</sup>	75.5·10 <sup>-6</sup>
Capacity/Ah	165		202	
Volume fraction at 50 % SOC	0.597	0.381	0.554	0.448
Lithium stoichiometry range	0.011 ... 0.64	1.9·10 <sup>-5</sup> ... 0.96	0.005 ... 0.75	0.0004 ... 0.995
Active material loading/mg/cm <sup>2</sup>	7.68	10.5	7.87	12.2
Active material capacity / mAh/cm <sup>2</sup>	2.72	1.81	2.82	2.11
Used electrode capacity / mAh/cm <sup>2</sup>	1.74		2.10	

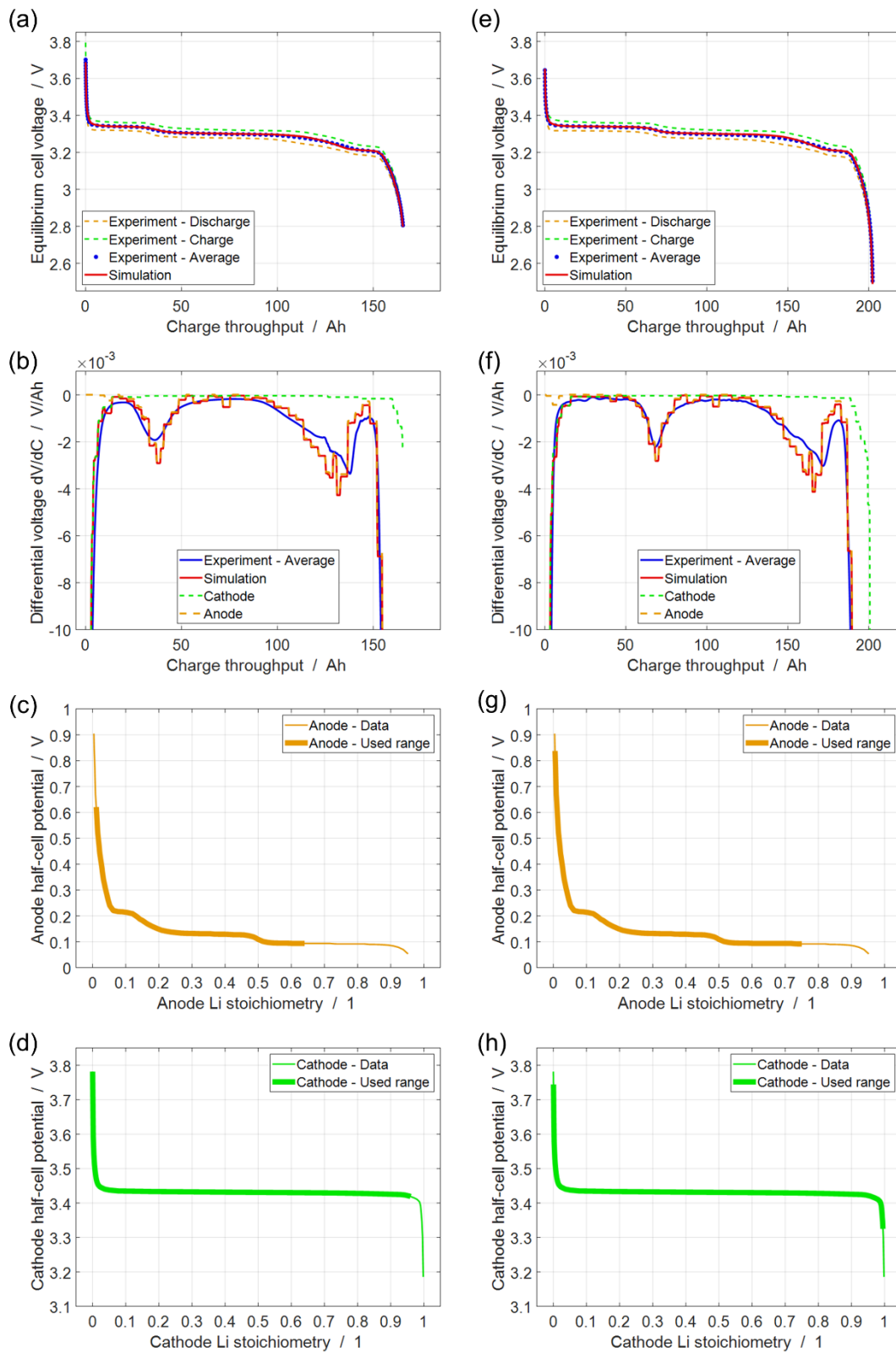


Figure 21: Results of the electrode balancing analysis of Sinopoly (left) and Calb (right) cells: pOCV curves (a, e), differential voltage curves (b, f), negative electrode half-cell voltage (c, g) and positive electrode half-cell voltage (d, h).



#### 4.1.4 Summary

The initial electrical and structural characterization test results are presented in this section. The capacity test results of Sinopoly and Calb cells revealed that Sinopoly cells had a large scatter of initial discharge capacity with an average below nominal cell capacity. In contrast, Calb cells had relatively uniform initial discharge capacity distribution above nominal capacity. Charge/discharge curves of both cell types demonstrate large flat voltage plateaus typical to LFP cells. Rate capability and temperature performance tests show that charge/discharge overpotentials increase with increasing current rates, and cell capacity decreases significantly at low temperatures, particularly at high current rates, for both cell types. One exemplary cell from each type was opened in an inert atmosphere. Each cell component's size, volume, and weight were measured quantitatively. The results show that cell casing makes an immense contribution to overall cell weight.

Additionally, electrode samples investigated in LM and SEM show small ( $< 1 \mu\text{m}$ ) LFP particles and larger ( $\sim 10 \mu\text{m}$ ) graphite particles on positive and negative electrodes, respectively. Furthermore, EDX elemental analyses of samples verify LFP/graphite cell chemistry. The range of lithium stoichiometries during charge/discharge is determined by electrode balances analysis of experimental data. In conclusion, the electrical and structural characterization test results create a reference initial state dataset for aging experiments and a self-consistent parameter set for the use in cell models needed for performance prediction or state diagnosis.

## 4.2 AGING CHARACTERISTICS OF COMMERCIAL BATTERY ENERGY STORAGE SYSTEMS WITH SERIAL AND PARALLEL CELL CONFIGURATIONS

In the previous section, the electrical and structural characterization results of Sinopoly and Calb cells are presented in detail, along with electrode balance analysis. As a follow-up experiment, we investigated the aging behavior of two commercial stationary storage system battery stacks of Sinopoly cells in serial and parallel configurations. The objective of the experiment is to monitor aging on stack and single-cell levels and observe the effect of stack configuration on overall aging.

The results presented in this chapter were published in *Energies*: M. C. Yagci, T. Feldmann, E. Bollin, M. Schmidt, and W. G. Bessler, "Aging Characteristics of Stationary Lithium-Ion Battery Systems with Serial and Parallel Cell Configurations," *Energies* 15, 3922 (2022) [43]. Initial characterization and periodic performance tests were performed by myself with the support of Jonas Touzri under the supervision of Wolfgang G. Bessler. Microgrid tests were performed

by Thomas Feldmann with the support of Michael Wirwitzki under the supervision of Elmar Bollin and Michael Schmidt. The data analysis was performed by myself with the support of Thomas Feldmann. The article was written by myself with the editing of Wolfgang G. Bessler, except for the experimental methodology of the Microgrid operation, which was written by Thomas Feldmann and edited by Michael Schmidt.

#### 4.2.1 Initial characterization and cell selection

The initial electrical characterization test results of 28 Sinopoly cells that are allocated for commercial BESS tests are used as a reference (labeled as “checkup 0”) for periodic checkups (cf. 3.5.1.4). The results of capacity and IR measurements (performed according to test protocols in Sections 3.4.1.2 and 3.4.1.5) of all 28 cells are shown in Figure 22. Panel (a) shows charge/discharge curves reproduced from Figure 12(a). Apart from very low and high SOC, the cells exhibit the flat voltage behavior typical for LFP-based cells. However, cell capacities show a strong capacity variation, ranging from 158.8 to 195.7 Ah (18.9 % capacity variation). Panel (b) shows the IR of the cells from pulse tests as a function of SOC. All cells show a slightly decreasing IR with increasing SOC, yet with a distinct peak at 50 % SOC. We attribute this peak to the fact that, at 50 % SOC, the pulse tests were interrupted to measure electrochemical impedance spectra. Similar to individual cell capacities, there is a strong cell-to-cell IR variation. At 50 % SOC, the values range from 0.59 to 0.98 m $\Omega$ .

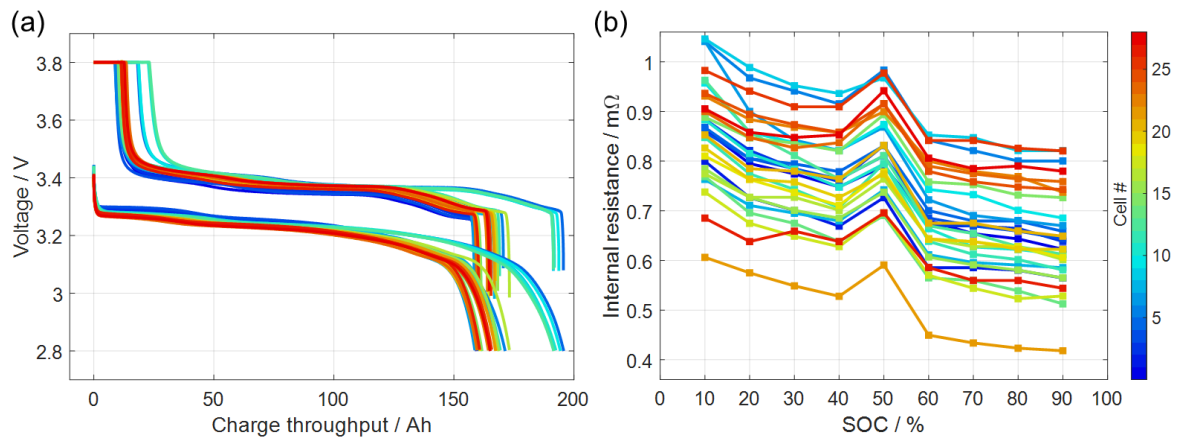


Figure 22: Initial characterization of 28 Sinopoly cells for commercial battery energy storage systems. (a) Galvanostatic cycling at 0.25C. The lower branch on the curves represents discharge, where time progresses from left to right; the upper branch represents charge, where time progresses from right to left. (b) Internal resistance  $IR_{\text{pulse}}$  calculated from Eq. (13) as a function of SOC.

Capacity and IR data are summarized in Figure 23 by plotting IR as a function of capacity. The data show that there is no correlation between these two performance indicators. As summarized in Table 1 and discussed in Section 2.1.2, cell-to-cell variations can be tolerated in a parallel cell configuration due to passive balancing. In contrast, capacity homogeneity is essential for serial cell configurations to eliminate the influence of possible “weak” cells exhibiting overcharge/overdischarge. In order to test this hypothesis, 14 cells with minimum capacity and IR difference were selected for the serial system. The remaining cells were allocated to the parallel system, as indicated in Figure 23. These cells were selected in such a way that the first stack (L1) consists of cells with a high capacity variation, and the second stack (L2) consists of relatively low (<5 Ah) capacity variation.

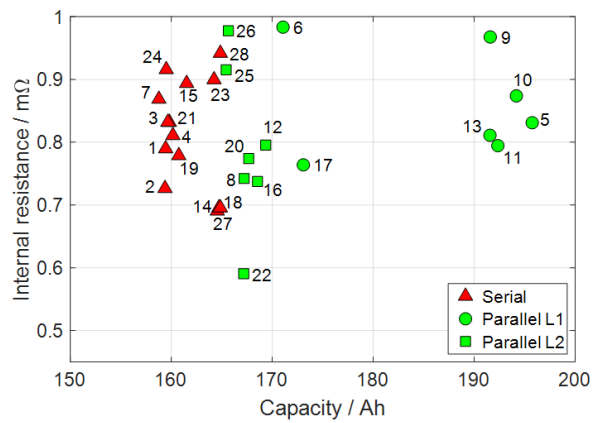


Figure 23: Initial internal resistance ( $IR_{pulse}$ ) at 50 % SOC as a function of initial cell capacity for all 28 cells and distribution of the cells to the two battery systems.

Furthermore, selecting cells with high capacity variation enables monitoring the possible architectural advantage of the parallel system, which is relatively unsusceptible to cell inhomogeneity due to passive balancing currents via the parallel connection. A statistical analysis of the cell selection is given in Table 21. The standard deviation of the capacities in the serial system is 2.18 Ah, which is significantly lower than the value of 11.35 Ah for the parallel system. The standard deviations of the IR are 0.071 mΩ and 0.085 mΩ for the serial and parallel systems, respectively.

Table 21: Statistical analysis of initial capacity and internal resistance test results for serial and parallel stack architectures.  $\Delta$  variation,  $\mu$  mean value,  $\sigma$  standard deviation.

	Capacity			Internal resistance		
	$\Delta$ / Ah	$\mu$ / Ah	$\sigma$ / Ah	$\Delta$ / m $\Omega$	$\mu$ / m $\Omega$	$\sigma$ / m $\Omega$
<b>Serial cell configuration</b>	6.08	161.59	2.18	0.251	0.812	0.071
<b>Parallel cell configuration</b>	30.3	177.18	11.35	0.392	0.825	0.085

#### 4.2.2 Microgrid operation

After the initial checkup and cell selection were performed as described above, 28 Sinopoly cells were assembled into the two battery systems (serial and parallel systems), as described in Section 3.5.1 in detail. The systems were operated as part of the microgrid over an extended period (around 1000 days). The timeline of the experiments is shown in Figure 24. Panel (a) shows the cumulated equivalent full cycles (EFC) as a function of time, which we define as

$$\text{EFC} = \frac{\text{Total discharged energy}}{\text{Nominal energy}} = \frac{\int_{\text{microgrid}} |P_{dis}| dt_{dis}}{V_N \sum_{n=1}^{N_{cell}} C_0^n} \quad (45)$$

where,  $P_{dis}$  is the discharge power,  $t_{dis}$  is the discharge time,  $V_N$  is the nominal cell voltage, and  $C_0^n$  is the initial discharge capacity of individual cell  $n$  as calculated during checkup #0. The sum  $n$  runs until the number of all cells ( $N_{cell}$ ) in the battery stack, and the integral on the numerator runs over the whole microgrid operation time. Due to differences in system architectures, stack capacities, and technical control systems design of the microgrid, the operation of the stacks was power controlled. Therefore, system power is used to calculate the total discharged energy in Eq. (45).

The type of operation mode indicated in the plot within the respective timeframe is either full-cycle or solar-storage mode. Also, the periods of the checkups are indicated, where the battery stacks were disassembled, the periodic reference performance tests were performed, and the battery stacks were reassembled. Minor rest phases during the operation were due to system or laboratory shutdowns. Over almost three years, the serial and parallel systems accumulated 810 and 881 EFCs, respectively. As the operating power was scaled to the individual system capacities described in Section 3.5.1.2, serial and parallel systems exhibited a similar number of EFCs.

Temperature has a strong influence on cell aging [27]. In Figure 24(b), measured cell and outside temperatures (daily averages) are plotted as a function of time. Temperature

measurements were integrated into the test setup only after the first checkup. Therefore, the data for the initial operation phase is missing. Outside temperature shows distinct seasonal variation, ranging between 5 to 30 °C. The temperatures inside the battery housings show a matching variation; however, they are up to 10 °C higher. The parallel system shows systematically higher temperatures than the serial system by ca. 2 °C. As mentioned earlier, the battery systems investigated here do not have dedicated cooling for battery stacks. As a result, the temperature difference between two battery systems can result from up to ten-fold higher currents and corresponding higher ohmic losses in the parallel system.

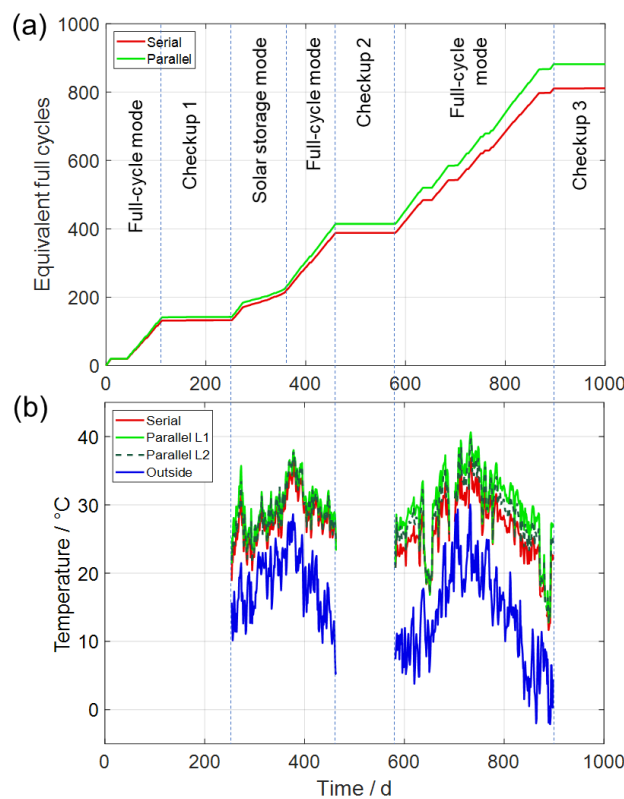


Figure 24: Timeline of the microgrid operation, including rests for cell checkup experiments. (a) Accumulated equivalent full cycles for the serial and parallel battery systems. (b) Daily average of measured temperatures.

In order to allow more detailed insight into battery operation, Figure 25 shows exemplary 48 h data of SOC, current, and voltage for the two battery systems, both for solar-storage mode (left panels) and full-cycle mode (right panels). In solar-storage mode, the systems exhibited a day-night partial cycle: fully charged during the day and then discharged to around 50 % SOC during evening and night. In full-cycle mode, the systems were operated continuously

between 30 % and 100 % SOC as set by the microgrid controller. The current and voltage characteristics represent the two system architectures. The serial system operated at high voltages (around 46 V) and low currents (up to 35 A). In contrast, the parallel system operated at low voltages (around 3.4 V, corresponding to the single-cell voltage) and high currents (up to 350 A).

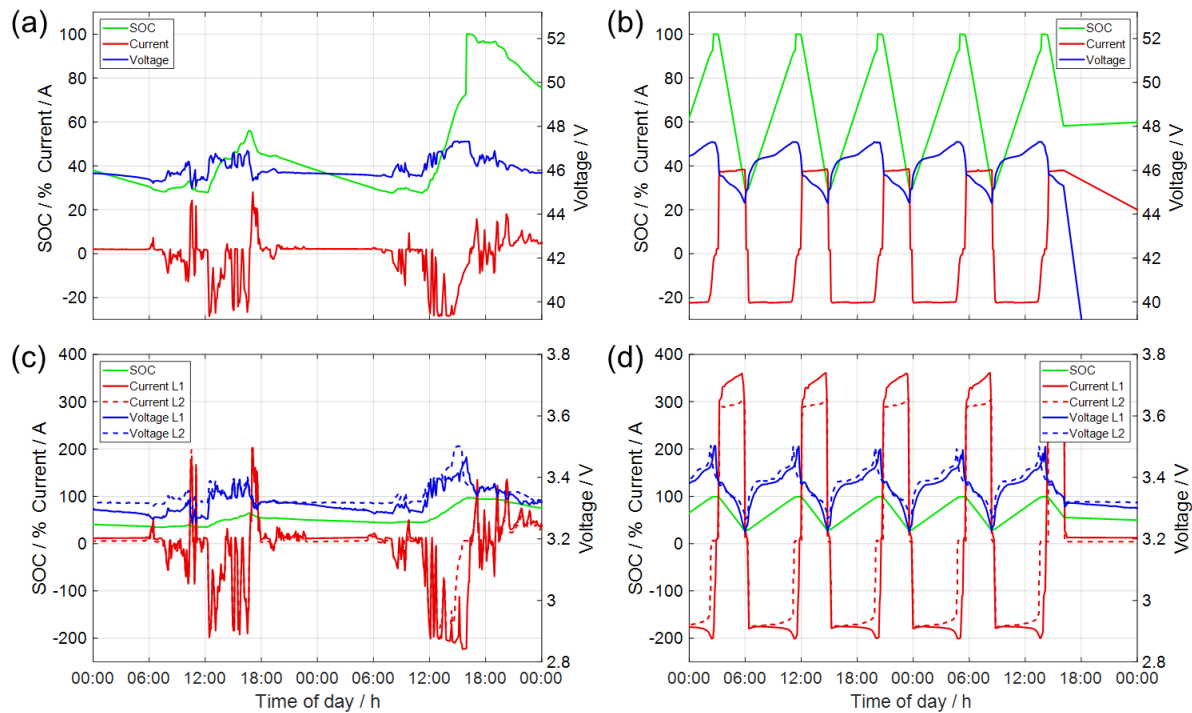


Figure 25: Exemplary microgrid operation data (SOC, current, and voltage) representing 48 h periods. (a) Serial system, solar-storage mode, (b) serial system, full-cycle mode, (c) parallel system, solar-storage mode, (d) parallel system, full-cycle mode. The scale ranges of the voltage axes correspond to the nominal voltage operation window of the systems.

### 4.2.3 Comparison of checkup results

The performance of each cell was investigated via three checkups throughout microgrid operation at time intervals indicated in Figure 24. The first checkup was performed after 112 days of full-cycle mode operation. The second checkup was performed after a mixed full-cycle mode and solar-storage mode operation of 210 days. The third checkup was performed after an extended 317-day full-cycle operation. As a result, the checkups were performed after 131, 388, and 810 (serial) and 141, 414, and 881 (parallel) equivalent full cycles, corresponding to 112, 462, and 897 days of testing, respectively. The checkup intervals are not constant

because of the technical inflexibilities of assembling and disassembling battery storage systems into and from a running microgrid.

The evolution of the discharge/charge characteristics of four exemplary cells is shown in Figure 26. Each panel compares the performance during the three checkups and the initial reference performance test (“checkup 0”). For each system (serial shown at the left, parallel at the right), one cell with relatively low capacity loss and the cell with highest capacity loss are shown. A significant capacity loss is visible for all cells; the discharge curves end at a lower charge throughput for later checkups. At the same time, the voltage spread between the charge and discharge branches remains relatively unaffected – in the plateau range between ca. 25 and ca. 125 Ah charge throughput, the discharge curves are lying more or less on top of each other. This indicates that the IR of the cells is not strongly affected by ongoing operation. The loss of cell capacity is also associated with a shortening and shifting of the characteristic voltage plateaus attributed to the stoichiometry range of the graphite anode [42].

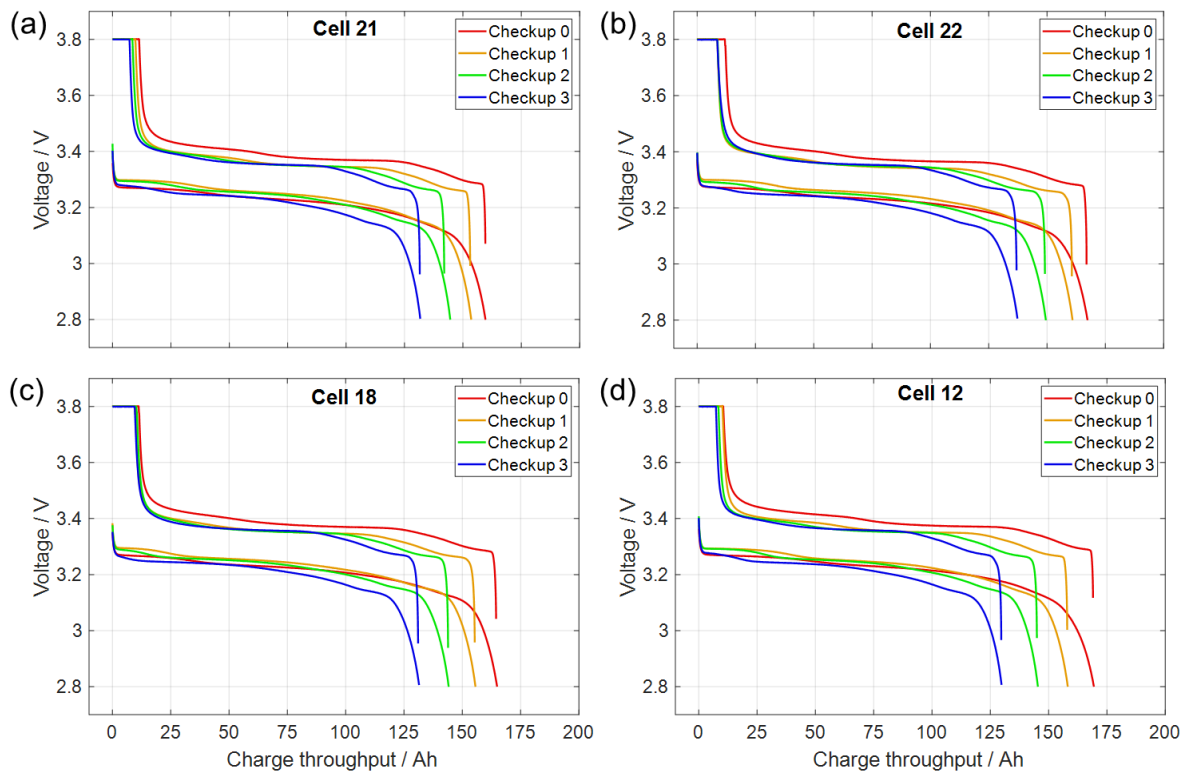


Figure 26: Charge/discharge behavior of exemplary individual cells with relatively low capacity loss (upper row) and highest capacity loss (lower row) for serial (left panels) and parallel (right panels) battery architecture. “Checkup 0” corresponds to the initial characterization of the fresh cells.

As shown in Section 4.2.1, the cells show a wide distribution of initial capacity. Therefore, the absolute and normalized capacity (*i.e.*, discharge capacity relative to initial capacity) are used for further analysis. Figure 27 demonstrates the change of absolute and normalized capacities during the checkups as a function of cell number. The order of the cells in this figure corresponds to the arrangement in the stacks (cf. Figure 8). All cells lose capacity monotonously with increasing cycling time, reaching around 80 % of the initial capacity at checkup 3. There is a clear cell-to-cell scatter. A statistical analysis of the capacity losses is given in Table 22. After checkup #3, the average capacity losses of cells amount to 18.6 % in the serial system and 21.4 % in the parallel system. Also, the scatter is larger in the parallel system than in the serial system. Therefore, the cells in the parallel system have aged slightly more than those of the serial system. However, the variation and standard deviation of the serial system are continuously increasing, while in the parallel system, both values decrease at checkup #2 and increase slightly until the end of the experiments. Thus, the higher average aging of parallel system cells can be attributed to relatively wide initial cell capacity variation rather than operational differences between systems.

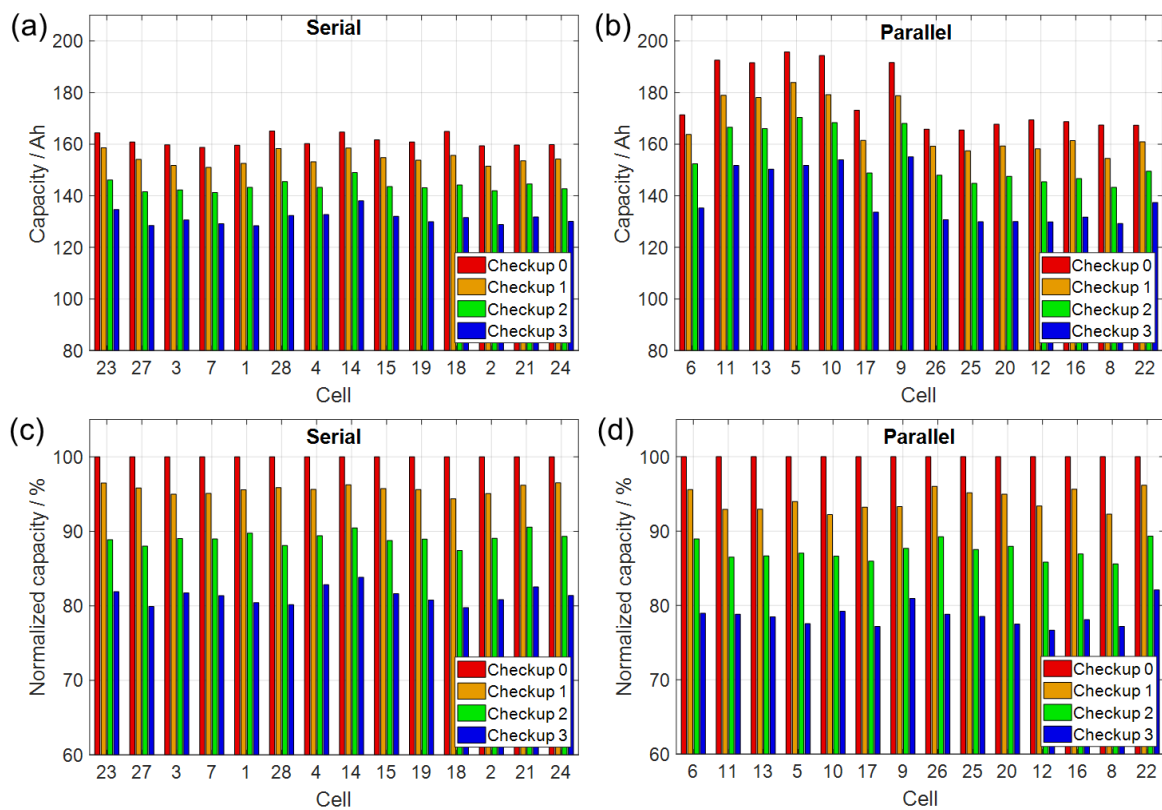


Figure 27: Absolute (a, b) and normalized (c, d) capacity for individual Sinopoly cells measured during each checkup. The test protocol is given in Section 3.5.1.4.



Table 22: Normalized capacity losses of serial and parallel system cells.  $\Delta$  corresponds to variation,  $\mu$  corresponds to mean value, and  $\sigma$  corresponds to standard deviation.

	Serial			Parallel		
	$\Delta / \%$	$\mu / \%$	$\sigma / \%$	$\Delta / \%$	$\mu / \%$	$\sigma / \%$
<b>Checkup 1</b>	2.1	4.3	0.6	3.9	5.9	1.4
<b>Checkup 2</b>	3.1	10.9	0.9	3.7	12.7	1.2
<b>Checkup 3</b>	4.1	18.6	1.2	5.4	21.4	1.5

Furthermore, at the end of the microgrid operation, the normalized capacity and internal resistance changes of 28 cells were compared to initial values. For this analysis, we used  $IR_{\text{cycle,CC}}$  method to calculate internal resistance as described in Section 3.1 Eq.(14). The four combinations of these two parameters versus each initial value are plotted in Figure 28. Panel (a) shows the capacity loss as a function of initial capacity. No capacity loss pattern depending on initial capacity is observed within and between the two systems; only the slightly higher capacity losses in the parallel system are visible. Panel (b) also shows no correlation between capacity loss and initial IR. Panel (c) shows the change of IR as a function of initial capacity. The change of IR is mostly negative (around -20 %), meaning that IR decreased between initial and final checkups, although four cells showed IR increase. Despite the common trend of decreasing IR, the correlation between the two parameters is still unclear. Finally, panel (d) shows the IR change as a function of initial IR. The data for the cells in the serial system exhibit a clear linear correlation: the magnitude of IR decrease is higher for the cells with higher initial IR, and IR increase is higher for cells with lower IR. The reason for this behavior is unclear. Possibly, this behavior is related to the diminishing of the initial cell-to-cell scatter of IR from 0.8-1.5 m $\Omega$  to 1.05-1.2 m $\Omega$  at the end of the experiment as, mathematically, the change is higher for outlier values in a converging system.

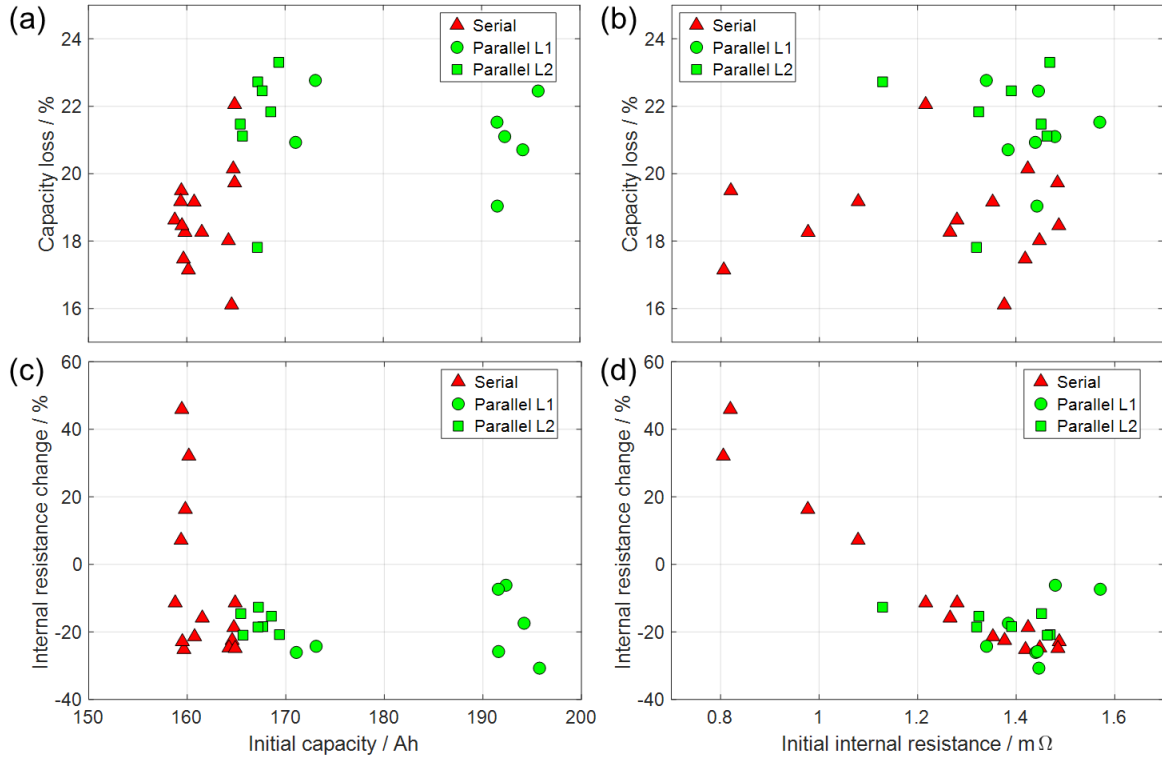


Figure 28: Capacity loss (upper panel) and internal resistance ( $IR_{\text{cycle,CC}}$ ) change (lower panel) at the end of microgrid operation as a function of initial capacity (a, c) and initial internal resistance ( $IR_{\text{cycle,CC}}$ ) (b, d). The initial capacity and internal resistance values are taken from the first checkup (#0), and the values at the end of the microgrid operation are taken from the last checkup (#3). The checkup test protocol is given in Section 3.5.1.4.

#### 4.2.4 Comparison of microgrid operation with temperature-controlled cycling

The serial and parallel system cells were operated in a commercial battery stack, controlling and monitoring the complete stack's total power input/output. Moreover, as mentioned above, no active temperature control exists within used commercial systems. Thus, for further assessment of the aging behavior of stack cells in comparison to single cell aging, two additional Sinopoly cells from the same delivered batch underwent continuous full cycles consisting of 0.83C (150 A) CCCV charge and CC discharge at 20 °C ambient temperature in a climate chamber with the test protocol described in Table 15. This type of experiment is typically used for assessing datasheet behavior. As mentioned in Section 3.5.2, the cycling of one of the cells was interrupted for cell opening. The aging test result of the remaining cell is shown in Figure 29 in comparison with serial and parallel system cells.

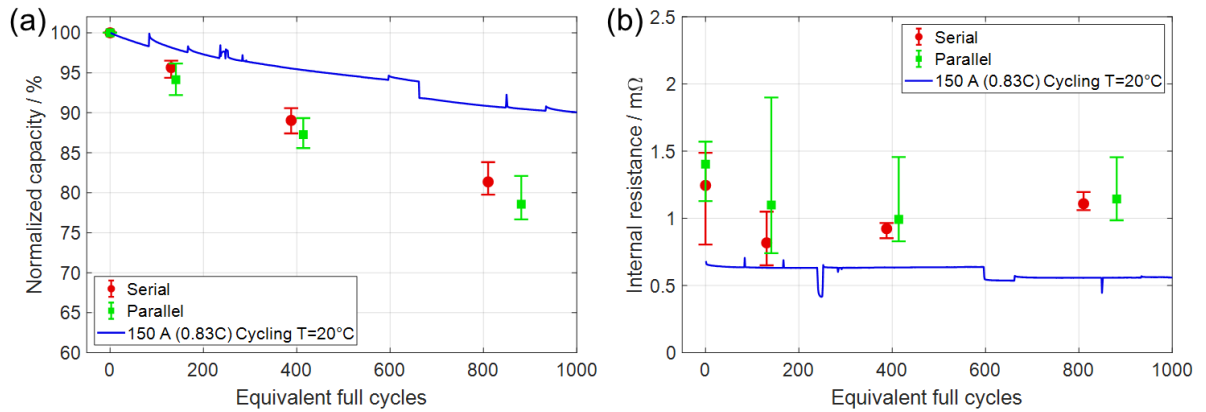


Figure 29: Comparison between the serial and parallel battery system cells (the error bars indicate the range of the 14 respective single cells) and an individual cell cycled with continuous full cycles at 20 °C. (a) Normalized capacity, (b) internal resistance ( $IR_{\text{cycle,CC}}$ ) calculated from the charge/discharge curves using Eq. (14). The single cycling test protocol is given in Section 3.5.2.

Figure 29 (a) compares the normalized capacity of the continuously cycling single cell and the average cell capacities of the serial and parallel BESS. The error bars indicate the range of the 14 respective single cells. The single cell exhibits a capacity loss of 10.0 % after 1000 EFC. Further cycling resulted in capacity losses of 20.3 % after 3000 EFC and 34.3 % after 4000 EFC (data not shown). The capacity retention of the tested cell is on par with the specifications given in the manufacturer’s product brochure (cf. Appendix 6.2.1), demonstrating 20 % capacity loss after 3000 cycles at 20 °C with C/3 currents. However, we can consider that our test cell demonstrates superior capacity retention, considering that, in our case, the C-rate is 2.5 times higher than the manufacturer’s capacity retention test. It is interesting to compare these results to the capacity losses of the battery systems, plotted as points in Figure 29 (a). The comparison shows that the single cycling cell exhibits a much smaller capacity loss than the system cells – the serial and parallel systems age about twice as fast as the single cell. These results are unexpected and highly problematic for system manufacturers who typically assign lifetime warranties based on single-cell testing results.

The IR of the continuous cycling single cell is calculated by  $IR_{\text{cycle,CC}}$  method (cf. Eq. (14)) and plotted as a function of cycle number in Figure 29 (b). Again, the data of the system cells are plotted as points, and the range of the 14 cells as error bars. The single cell exhibits an essentially constant IR over the 1000 full cycles. The system cells show an IR drop from initial characterization (0 cycles) to the first checkup (ca. 135 cycles) and then an increase of IR until, at the last checkup, it has a similar value as initially. The initial IR drop means the cells

seem to have been activated during the first cycles, as discussed above. The origin of the activation is unclear. The IR of the cycling cell is around a factor of two lower than that of the system cells, which might be due to a higher cell temperature resulting from the continuous 0.83 C cycling. It should be noted that the IR shows a strong cell-to-cell scatter (large error bars in Figure 29 (b)). At present, it is not possible to assess if this is an actual property of the cells or if this is caused by measurement inaccuracy (e.g., resulting from different contact resistances of the connection cables).

#### **4.2.5 Discussion**

In Section 4.2, we have presented the aging characteristics of 28 cells operated in two battery systems with different cell configurations. The observed overall capacity loss of ca. 20 % after ca. 2.5 years and ca. 850 EFC of operation is relatively high for stationary applications, where lifetimes of > 5000 EFC (corresponding to ca. 17 years of operation at 300 EFC per year [129]) are expected. Surprisingly, the single cell tested under laboratory conditions exhibited significantly lower capacity loss. Several potential reasons can be discussed as the origin of stronger aging of cells under system operation as opposed to cells under laboratory operation: (i) influence of check-up experiments, (ii) influence of current rate and cycling depth, (iii) influence of inverters, (iv) influence of cell balancing, (v) influence of temperature. The effects of each possible factor will be discussed in the coming subsections.

##### **4.2.5.1 Influence of checkups**

The periodic checkups are not considered while calculating the duration of cell operation in terms of EFC since the influence of checkup tests can be neglected, as each checkup contributed only three full cycles to the total of 810 (serial) and 881 (parallel) equivalent full cycles. The effect of additional resting periods due to assembly/disassembly and transportation of the cells can be considered calendaric aging periods. The effect of such calendaric aging periods on aging can be neglected in a head-to-head comparison of serial and parallel systems because its duration was the same for all cells.

##### **4.2.5.2 Influence of C-rate and DOD**

In the literature, both high cycling depth and high currents have been observed to accelerate capacity loss in lithium-ion battery cells [16,17,19]. During microgrid operation, the serial and parallel system cells cycled between 100 % and 30 % SOC during full-cycle mode, corresponding to 70 % DOD. In the serial system, throughout the full-cycle mode, the maximum current was lower than 0.25C (45 A), on average 0.12C (22.1 A) at charge and 0.21C (38.5 A) at discharge. In the parallel system, cell currents were not measured separately.

However, for comparison, maximum charge and discharge currents can be assumed to be distributed equally to each cell. The maximum charge and discharge currents are calculated as a result of this assumption as 0.16C (28.6 A) and 0.28C (51.1 A), respectively.

On the other hand, the single cycling cell is subjected to full cycles (100 % DOD) at a much higher current of 0.83C (150 A). Therefore, the cycling conditions in the system are significantly softer than those for the single cell. Therefore, the proposed negative effect of higher C-rate and deeper cycles on aging is opposite to the observation shown in Figure 29 and cannot explain the relatively higher aging of serial and parallel system cells.

#### **4.2.5.3 Influence of power electronics**

Power electronics, particularly DC-AC inverters, are essential for integrating a stationary storage system into the AC grid. During inverter operation, the batteries are subjected to fast (typically, 50 Hz) voltage fluctuations referred to as ripples. These ripples result from incomplete suppression of high-frequency AC harmonics during AC-DC rectification or electrical noise generated by internal electronic switching operations of the power electronics [130]. Research on various lithium-ion battery types and waveforms demonstrated insufficient evidence to prove that ripples affect lithium-ion battery aging [131–134]. It was suggested that the electrochemical double-layer capacitance acts as a filter against AC harmonics, thus limiting their effect on cell aging [132,134]. On the other hand, it was recently shown that low-frequency harmonics below the corner frequency of the double-layer capacitance cause accelerated aging in NMC lithium-ion batteries [135]. In summary, there is not enough proof to state whether there is a significant contribution of inverters to the aging of lithium-ion batteries.

#### **4.2.5.4 Influence of cell balancing**

In the serial system, the cells have individual balancing circuits. These circuits induce additional currents or microcycles in the cells. The influence of these currents on aging has not been investigated so far, to the best of our knowledge. The parallel system does not have an active balancing system. Still, passive balancing currents are expected between the cells during rest phases to balance possible differences in cell voltages. These passive balancing currents between cells cause additional microcycles. The magnitude of the active or passive balancing currents is expected to be much smaller than the absolute charge and discharge currents. It is, therefore, unlikely that they are the origin of the accelerated aging of the serial and parallel systems. Moreover, in the case of parallel configuration, the magnitude of passive balancing currents is expected to be higher in outlier cells, that is, cells with the highest and

lowest capacities. However, the comparison of capacity loss of cells depending on their initial capacities (Figure 28(a)) does not show accelerated aging of outlier cells.

#### **4.2.5.5 Influence of temperature**

As discussed in Section 2.3.3.1, higher temperature causes higher capacity loss. As already shown and discussed above (Figure 24), the temperatures in the systems show a significant seasonal variation. Additionally, the system cells are closely packed (cf. Figure 8), which hinders heat transfer out of the cells. Consequently, measured cell surface temperatures were very high (up to 40 °C in summer) with substantial seasonal variation. The single cell was operated at 20 °C ambient temperature under strong heat convection in the climate chamber. The surface temperature of the single cell measured by a thermocouple was constantly at 25 °C.

Grolleau et al. give a thermal activation energy of 52.1 kJ/mol for the SOC-independent term of their aging model [78]. Kupper et al. use a thermal activation energy of 55.5 kJ/mol for the aging reaction implemented in their model [27]. Using a value of 53 kJ/mol, the Arrhenius equation yields a factor of two when increasing temperature from 25 °C (assumed single-cell temperature) to 35 °C (assumed average system-cell temperature), which agrees very well with the two times more capacity loss of serial and parallel system cells compared to single-cell (cf. Figure 29). From this discussion, we tentatively conclude that the observed faster capacity loss of the cells operated in the system, compared to the single-cell cycling experiment, is due to a difference in cell temperatures.

The temperature of individual cells in a battery system depends on the position within the stack. According to the discussion above, this should also affect aging behavior. The capacity losses of the cells as a function of the spatial position are shown in Figure 30. Indeed, in both battery architectures, the cells with the lowest capacity loss are at the sides of the stacks where convective heat losses to the ambient are possible. Otherwise, there is no explicit dependence of aging on cell position for the serial system. For the parallel system, however, the strongest aging occurs towards the center of the two stacks, which might be associated with the position of the main cables close to the center of the current collector rails (cf. Figure 8). Towards the main cable connections, the current on the rails gets higher, which may be associated with the highest ohmic heating (proportional to current squared) of the rails, higher temperatures of the cells in the center, and, therefore, stronger aging. The results thus show that the spatial position of cells within the stack does have a clear, albeit weak, influence on aging and underlines the need for a homogeneous thermal design of the battery system. The actual temperature distribution of the stacks was not measured throughout experiments,

so the analysis of the correlation between cell temperature and aging is limited to the assumption that the cells on the sides exhibit lower temperatures than the ones in the interior. However, the higher capacity losses of interior cells still give hindsight about the importance of the thermal management of stacks for the overall battery lifetime.

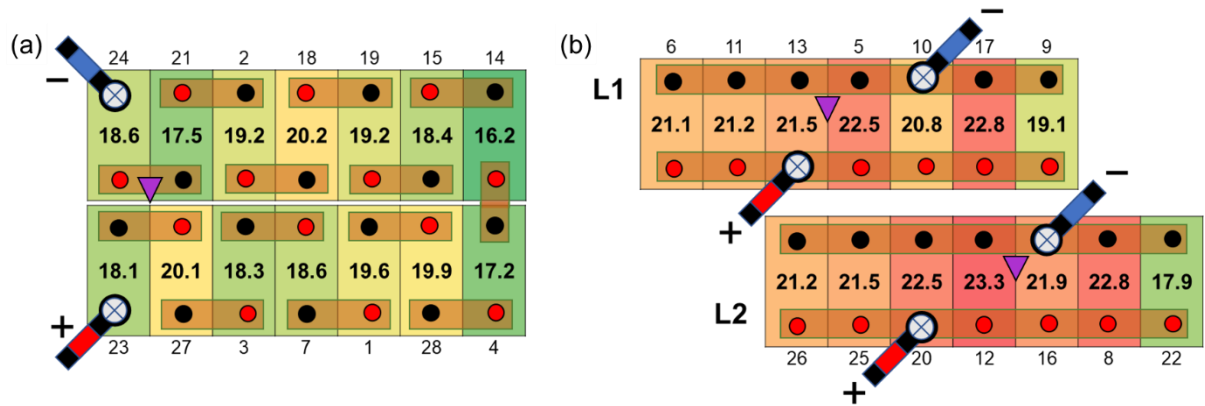


Figure 30: Capacity loss of the individual cells (given as numerical values in percent and also as color code) of the (a) serial and (b) parallel battery architectures according to the spatial position (cf. Figure 8). The cell number is given in smaller font below the cells. The purple symbols indicate the position of the thermocouples for recording the temperature data shown in Figure 24.

#### 4.2.5.6 Influence of cell configuration

Assessing the difference in aging behavior between serial and parallel cell configurations is one of the goals of the aging investigation on the system level. Therefore, the two battery systems were operated strictly synchronously under the same ambient temperature conditions. As a consequence of the different system designs, this still resulted in different current loads and temperatures for the individual battery cells. Still, the difference between the average capacity loss of serial and parallel systems at the end of the microgrid operation was only 2.8 %, which is within the capacity loss variation of the cells of both systems. Despite minor differences, we conclude that there is no dominant configuration-specific influence on cell aging. The slightly higher capacity loss of the cells in the parallel system is probably due to a higher temperature of the cells, which possibly results from the ohmic heating of the current collection rails and the connection cables, as already discussed above. Furthermore, the large initial cell-to-cell capacity variation up to 30.3 Ah can lead to passive balancing

currents between the cells during rest phases, which may cause additional microcycles and heat losses.

#### **4.2.6 Summary**

The realistic aging characteristics of two commercial BESS equipped with Sinopoly cells with different (serial and parallel) battery stack architectures are investigated during microgrid operation for 1000 days. The results reveal that on the system level, both BESS lost significant (serial: 18.6 %, parallel: 21.4 %) capacity after 810 (serial) and 881 (parallel) EFC, which is much below the 5000 EFC lifetime target of manufacturers. Furthermore, a single cell under cycling at a higher C-rate at 20 °C ambient temperature demonstrated superior capacity retention by losing 10 % capacity after 1000 EFC. Therefore, we attribute higher temperatures (measured up to 40 °C on BESS cell surfaces) to a factor of two higher capacity loss in BESS cells. Additionally, there is no clear superiority in aging performance between serial and parallel stack architectures. Therefore, parallel system architecture can be economically advantageous because of the possibility of using cells with different capacities and SOHs.

### **4.3 CALENDARIC AND CYCLIC AGING CHARACTERISTICS OF SINGLE CELLS**

In Section 4.2, the results of the aging investigation of two commercial battery stacks (built with Sinopoly cells) under realistic operation conditions are presented. No superiority between system architectures is detected, and more interestingly, both systems underperformed compared to single cell continuously cycled at a higher C-rate at controlled ambient temperature. We conclude that the superior performance of the single cell is due to lower cell temperature. However, the individual contribution of calendaric aging and cyclic aging periods of system cells to overall aging cannot be quantified. Therefore, temperature-controlled single-cell calendaric and cyclic aging experiments were performed according to the test protocol in Section 3.6 by using Calb cells to distinguish the contributions of temperature and operation mode (cycling or rest) on aging. This experiment allowed us to compare head-to-head the aging of the cells under the same aging type (calendaric or cyclic) at different temperatures and the cells at the same temperatures with different aging types. Additionally, to investigate the effect of storage SOC on calendaric aging, two calendaric aging test groups were present at each temperature at 100% SOC and 75% SOC, corresponding to fully charged cell and cell resting at voltage plateau, respectively.

The results presented in this chapter will be published in an article in preparation: M. C. Yagci, O. Richter, R. Behmann, and W. G. Bessler “Degradation modes of large-format stationary-



storage LFP-based lithium-ion cells during cyclic and calendaric aging”. The experimental methods were created by myself with Wolfgang G. Bessler’s supervision. The execution of aging tests and experimental data analysis was performed by myself with the support of René Behmann. Oliver Richter performed degradation mode analysis for his seminar work at Offenburg University of Applied Sciences under Wolfgang G. Bessler’s supervision. The text was written by myself except for the degradation mode analysis section, which is written with the support of Oliver Richter. The manuscript was edited by Wolfgang G. Bessler.

#### 4.3.1 Initial characterization

Charge and discharge curves, temperature dependencies, efficiencies, and internal geometries of the Calb cells used in single-cell aging experiments are presented in Section 4.1. In order to minimize cell-to-cell variations, the most homogenous 12 cells were selected to represent all test scenarios (cf. Table 16) among 28 Calb cells from the same batch. Cell capacity and IR were used to compare the homogeneity of fresh Calb cells. After selection, 12 Calb cells were numbered from #1 to #12. The capacity and IR (calculated by the  $IR_{pulse}$  method from Eq. (13)) of the selected cells measured during initial electrical characterization are shown in Figure 31.

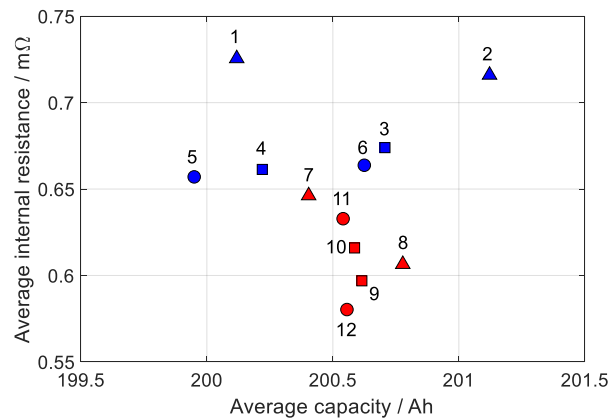


Figure 31: Average discharge capacity and average internal resistance (2%-98% SOC)  $IR_{pulse}$  (Eq. (13)) of 12 Calb cells investigated for calendaric and cyclic aging measured during initial characterization. Cell numbers are indicated next to the data points. Blue cells are used for aging tests at 35 °C ambient temperature, and red cells are used for aging tests at 50 °C ambient temperature.

The average charge/discharge capacities of the cells vary between 199.9 Ah and 201.1 Ah. The capacity range is 1.2 Ah, corresponding to 0.6 % of the maximum cell capacity. Average

IR varies between 0.58 mΩ and 0.73 mΩ. The IR range is 0.15 mΩ, corresponding to 20 % of the maximum IR. While capacity variation is small, IR variation is significant. Large deviations in IR of cells may be explained by the very low, sub-milliohm IR of these large-format cells that are well-below the measurement accuracy of the battery cycler (Biologic VMP3, France) given as 0.4% of the recorded value at the datasheet, which corresponds to an accuracy of  $\pm 0.1$  A for pulsed internal resistance measurements. Therefore, based on the similarity of the cell capacities, we believe that the cells are sufficiently similar to quantitatively compare their aging behavior in the remainder of the study.

### 4.3.2 Cyclic aging

The cyclic aging tests were performed until each cell completed approximately 1500 full cycles. Specifically, 1509, 1500, 1495, and 1505 full cycles are completed for cells #1, #2, #7, and #8, respectively. Exemplary full charge/discharge cycles of Cell #1 (cycling at 35 °C) and Cell #7 (cycling at 50 °C) are shown in Figure 32.

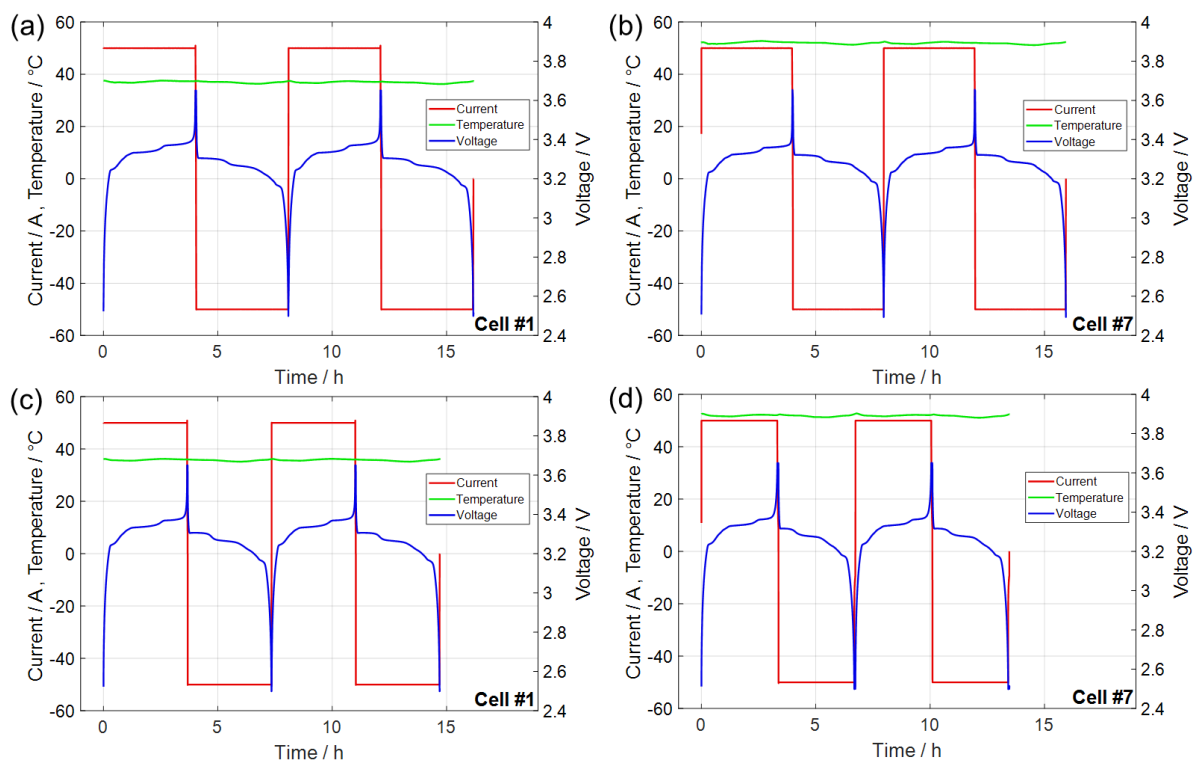


Figure 32: Voltage, current, and temperature profiles during two exemplary consecutive full cycles as a function of cycle time. (a) Cycle 10 and 11, Cell #1, cycled at 35 °C. (b) Cycle 10 and 11, Cell #7, cycled at 50 °C. (c) Cycle 1100 and 1101, Cell #1, cycled at 35 °C. (d) Cycle 1100 and 1101, Cell #7, cycled at 50 °C.

The upper panels of the figure show relatively fresh cells undergoing 10th and 11th cycles. Full charge/discharge cycles take 8 hours ( $\pm 4$  mins), which is in good agreement with the actual C-rate corresponding to C/4. The lower panels show the same cells in their aged state undergoing 1100th and 1101st cycles. In aged cells, full cycle duration is significantly shortened to 7.35h (Cell #1 at 35 °C) and 6.7h (Cell #7 at 50 °C) due to capacity loss with aging. Cell surface temperatures are, on average, 2 °C higher than ambient temperature. The CV phases exist for charge and discharge but are not visible in figures due to their very short duration (maximum 2 minutes) compared to the total length of full charge/discharge.

Charge and discharge curves of every 100th cycle, plotted as voltage vs. charge throughput, are shown in Figure 33 for Cell #1 (cycling at 35 °C) and Cell #7 (cycling at 50 °C). The cell capacity decreases with increasing number of cycles. As expected, the capacity loss is faster at 50 °C than 35 °C. Interestingly, at 35 °C, there is no significant change in overpotentials (the voltage gap between charge and discharge branches) with increasing cycle number. The stable charge-discharge plateaus are attributed to non-increasing cell resistance in the literature [76]. On the other hand, at 50 °C, overpotentials increase continuously, more significantly at lower SOC (0-25 %) and higher SOC (75-100 %). Both datasets show a clear shift of the characteristic voltage step at around 60 Ah charge throughput, associated with the graphite electrode, which will be exploited in the degradation mode analysis (cf. Section 4.3.4.2).

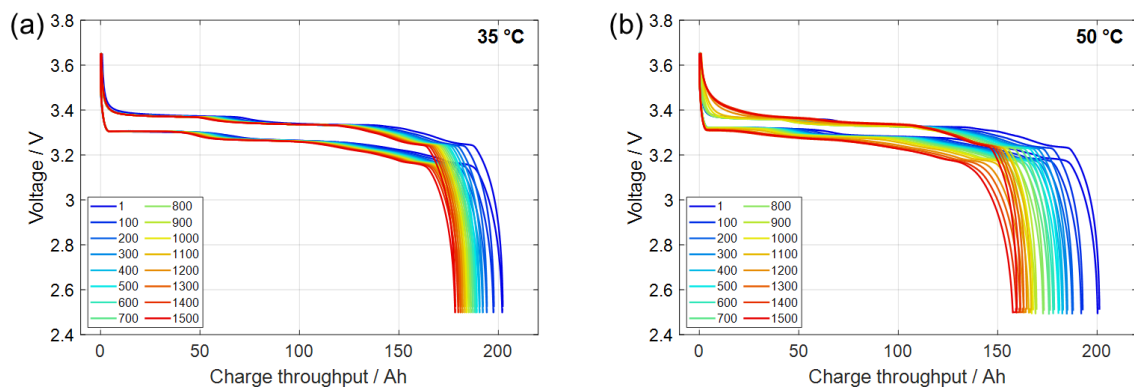


Figure 33: Selected galvanostatic 0.28C aging cycles of (a) Cell #1 cycled at 35 °C and (b) Cell #7 cycled at 50 °C. The lower branches on the curves represent discharge, where time progresses from left to right; the upper branches of the curves represent charge, where time progresses from right to left.

The quantitative analysis of cell characteristics throughout cyclic aging is shown in Figure 34. Cells #1 and #2 are cycled at 35 °C, and cells #7 and #8 are cycled at 50 °C ambient temperature. Discharge capacity is displayed in panel (a). All cells continuously lose capacity. The curves show small discontinuities every ca. 100 cycles, associated with scheduled stops and restarts of the cycling protocol defined in experimental methodology (cf. Section 3.6.1). The 50 °C cells show more significant discontinuities at 100, 500, 1000, and 1400 cycles. These points correspond to lengthy interruptions of cyclic aging tests lasting more than a week: the first three are regular checkups, and the last one is a technical problem resulting in a power outage. After each break, the cycling continues with visibly different capacity for a few cycles until the curve approaches the pre-break values. This behavior has been interpreted before due to the anode overhang [121]. Although the 35 °C cells were subjected to checkups simultaneously with 50 °C cells, the impact on the discharge capacity is much less pronounced than in the case of the 50 °C cells.

Panel (b) shows  $IR_{\text{cycle,full}}$  calculated from Eq. (15) as a function of cycle number. All cells show a small drop of IR during the first ca. 20 cycles, then a temporary increase for ca. 20 cycles, along with similar incremental increases in coulombic and energy efficiency. These results are in parallel with the initial overvoltage decrease of LFP cells observed in the literature [105]. The impedance decrease in the first cycles of LFP cells can also be attributed to the electrochemical milling of the PE. Electrochemical milling is the process in which LFP particles crack and crumble because of mechanical stress due to volumetric change during Li (de)intercalation. These cracks increase the active surface area and the tortuosity of the electrode, which facilitates electronic conductivity and mass transport [88]. The 35 °C cells then show a very slow increase of 4.7 % on average between the 100th and 1000th cycles, followed by a slightly accelerated IR increase. The 50 °C cells start with a significantly lower IR, associated with faster electrochemistry and transport at higher temperatures. The IR slightly increases up to ca. 800 cycles. Then, the cells show a “knee” type behavior [136], with rapidly increasing IR associated with short-term fluctuations. After the 1000th cycle break (third checkup), the cells continue with a higher IR, while after the 1400th cycle, IR decreases significantly for cells cycled at 50 °C. These results underline the influence of the checkups and other lengthy interruptions on cell behavior and, therefore, the nonlinear dependence of aging on cell history.

Panels (c) and (d) show SOH, defined in Eq. (10). Panel (c) shows a linear plot, while panel (d) uses the same data plotted as a function of the square root of the number of cycles. The cells cycled at 35 °C show significantly better capacity retention (86-88 % SOH) at the end of the test compared to the ones cycled at 50 °C (77-79 % SOH). The high-temperature cells reached

80 % SOH (end of commercial life) at around 1350 cycles. The dashed line in panel (d) corresponds to linear interpolation using the first 300 cycles for each cell. Cell #1 (cycled at 35°C) demonstrates close to linear behavior of SOH versus square root of cycle number during the first 500 cycles, while Cell #2 (cycled at 35 °C) temporarily deviates from the linear fit between cycles 50-290. After 415 cycles, Cell #2 permanently deviates from linear fit. Both cells cycled at 50 °C show an initial deviation from linear fit (between cycles 27-255 for Cell #7 and 27-132 for Cell #8). After ca. 350 cycles both cells cycled at 50 °C deviates from the linear fit permanently. In the literature, the square root of time dependency of capacity loss is calculated and experimentally validated by semi-empirical life models [137]. The physical origin of the  $\sqrt{t}$  dependency is attributed to the SEI formation in which diffusion-limited growth is involved [96].

Finally, panels (e) and (f) show coulombic efficiency (CE) and energy efficiency ( $\eta_{\text{energy}}$ ). CE and  $\eta_{\text{energy}}$  are calculated from the charge/discharge dataset of cyclic aging tests. In other words, for each cell CE and  $\eta_{\text{energy}}$  are calculated at cyclic aging test temperature (cf. Table 16) indicated next to cell numbers in Figure 34 and with the same protocol as cyclic aging tests (cf. Table 17). Coulombic efficiency remains close to unity for all cells over the complete experiment; we believe that the slightly lower efficiency of Cell #7 is due to miscalibration of the associated cyler channel. Still, the 50 °C cell data exhibit more significant noise than the 35 °C cell data, the origin of which is unclear. After ca. 900 cycles, the energy efficiency of 50 °C cells is reduced even below the efficiency of 35 °C cells. Moreover, the reduction of energy efficiencies of 50 °C cells is inversely symmetrical with the increase of internal resistance after 900 cycles in panel (b). Even the step increase in energy efficiency after 1400 cycles superimposes with the decrease in internal resistance in the same cycling period. Therefore, an increase in internal resistance is presumably the leading cause of energy efficiency decrease in 50 °C cells.

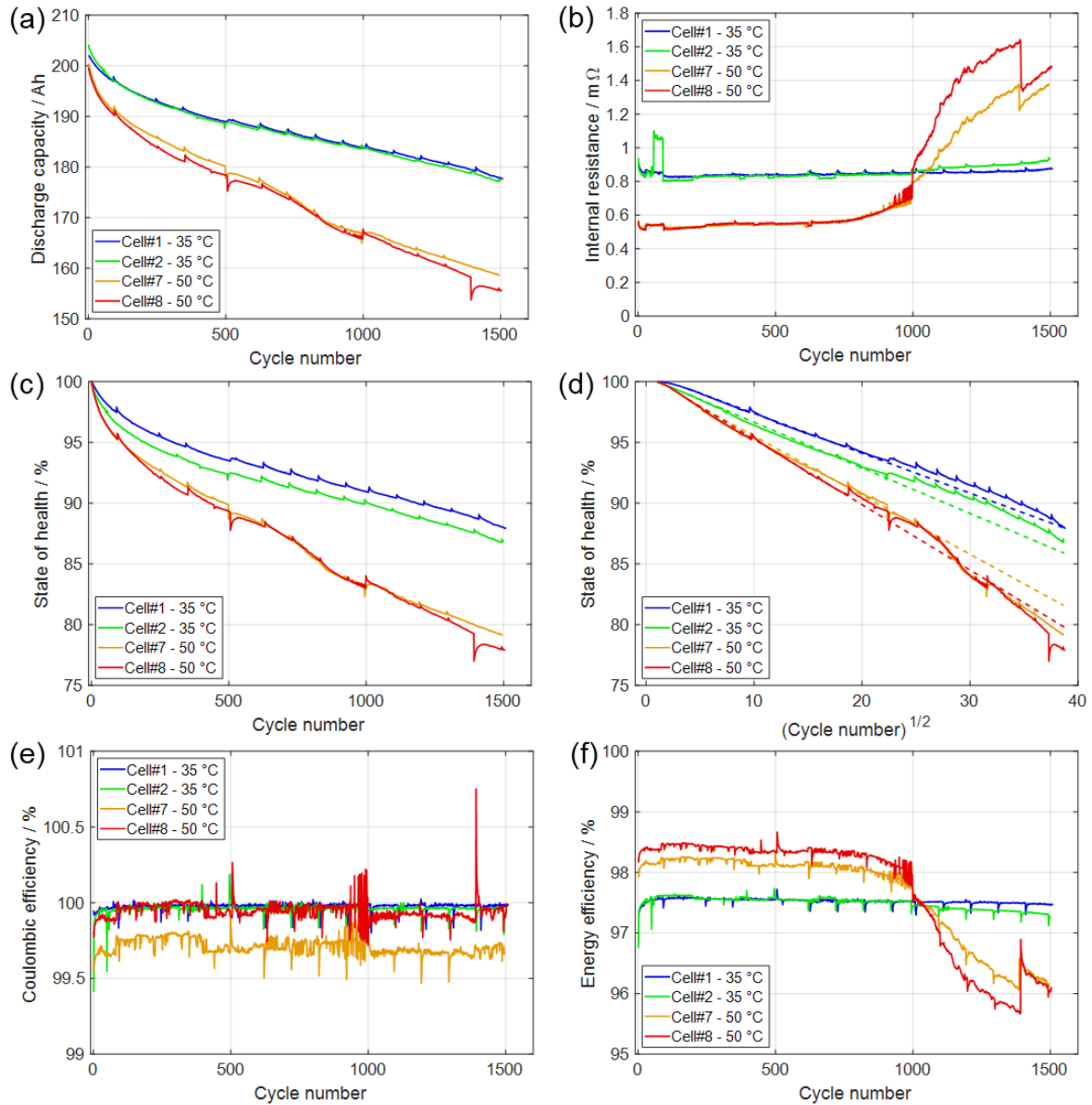


Figure 34: Quantitative analysis of cyclic aging test data. (a) Actual discharge capacity  $C_R$ , (b) internal resistance  $IR_{\text{cycle,full}}$  (calculated from Eq. (15)), (c) state of health (SOH) vs. cycle number, (d) SOH vs. square root of cycle number, (e) coulombic efficiency (CE), and (f) energy efficiency ( $\eta_{\text{energy}}$ ).  $C_R$ ,  $IR_{\text{cycle,full}}$ , CE, and  $\eta_{\text{energy}}$  are calculated from cyclic aging tests CCCV charge/discharge cycles at 0.28C (CV cut-off current: 0.05C) according to the cyclic aging test protocol given in Table 17 at ambient temperatures given in legend next to cell numbers.

### 4.3.3 Calendaric aging

The calendaric aging cells were kept under the test conditions given in Table 16 for 875 days. The electrical properties of the cells, except cell voltage, are measured only during checkups

to isolate any cycling aging effects from calendaric aging cells. The quantitative analysis of checkup results of calendaric aging cells is presented in Figure 35. Checkups were performed at ca. 0, 100, 250, 550, and 850 days. According to discharge capacity test results in panel (a), all cells lose capacity continuously during calendaric aging. Exceptionally, between checkup #1 and checkup #2, taking place after 106 and 255 days of aging, capacity loss of 35 °C cells is minimal (between 0.8 Ah - 1.08 Ah), which is more than 2 to 7 times smaller compared to capacity losses between other checkups. SOH evolution in panel (c) shows that relative capacity loss is higher in 50 °C cells (ca. 13.6 % on average) compared to 35 °C cells (ca. 7.7 % on average) independent of SOC level. Moreover, within the cells aged at the same temperature, no capacity retention superiority is observed between SOC levels. The observations on relative capacity change indicate that temperature is the dominant factor in the SOH decrease of calendaric aging cells. Panel (d) shows SOH change as a function of the square root of time plotted along with dashed lines corresponding to linear fit data generated with the MATLAB Basic Fitting tool. 50 °C cells, except for slight discrepancies at checkup #2, show a straight linear decay with the square root of time until the end of experiments. It is not possible to observe any consistent linear decay pattern for 35 °C cells.

Panel (b) demonstrates  $IR_{\text{cycle,full}}$  calculated from charge/discharge curves during checkups according to Eq. (15) as a function of test time. After the initial IR drop for all cells at checkup #1, all cells underwent IR increase at checkup #2. The highest IR values were measured for all cells except Cell #9 (calendaric aging conditions: 50 °C, 100 % SOH) at checkup #2. IR decreases once more according to checkup #3 results until rising finally close to initial values at the end of the tests. IR measurements at checkup #3 uniquely show that all cells aged at constant 100 % SOH have lower IR than the ones aged at 75 % SOH, but this pattern cannot be observed by any other quantitative analysis. The IR values of the large-format cells used for the calendaric aging experiment are in m $\Omega$  level. In addition, the cell contacts had to be changed for some cells during each setup, contrary to the cyclic aging cells due to the limited number of test channels available. Therefore, the fluctuation of IR can probably be attributed to the changes in contact resistances.

Panels (e) and (f) show the results of coulombic efficiency (CE) and energy efficiency ( $\eta_{\text{energy}}$ ) analysis results. Initial characterization results (checkup #0) show larger cell-to-cell CE and  $\eta_{\text{energy}}$  variations (3.5 % for CE and 2.6 % for  $\eta_{\text{energy}}$ ) compared to checkups #1-4 (between 1.5 % and 1.7 % for CE and between 1.6 % and 2 % for  $\eta_{\text{energy}}$ ). The difference in variety is probably because checkup #0 was performed with Biologic VMP3 and checkups #1-4 with Basytec XCTS and Basytec GSM battery cyclers. In panel (e) following checkup #1 until the

end of measurements, CE remains steady and close to unity for all cells. The offset observed at each cell can be attributed to the miscalibration of test channels. The  $\eta_{\text{energy}}$  dataset in panel (f) shows that 50 °C cells have higher  $\eta_{\text{energy}}$  than 35 °C cells starting with checkup #1. Similar to coulombic efficiency results, energy efficiencies of calendaric aging cells demonstrate little variety ( $< 0.5\%$  for all cells) throughout the experiment.

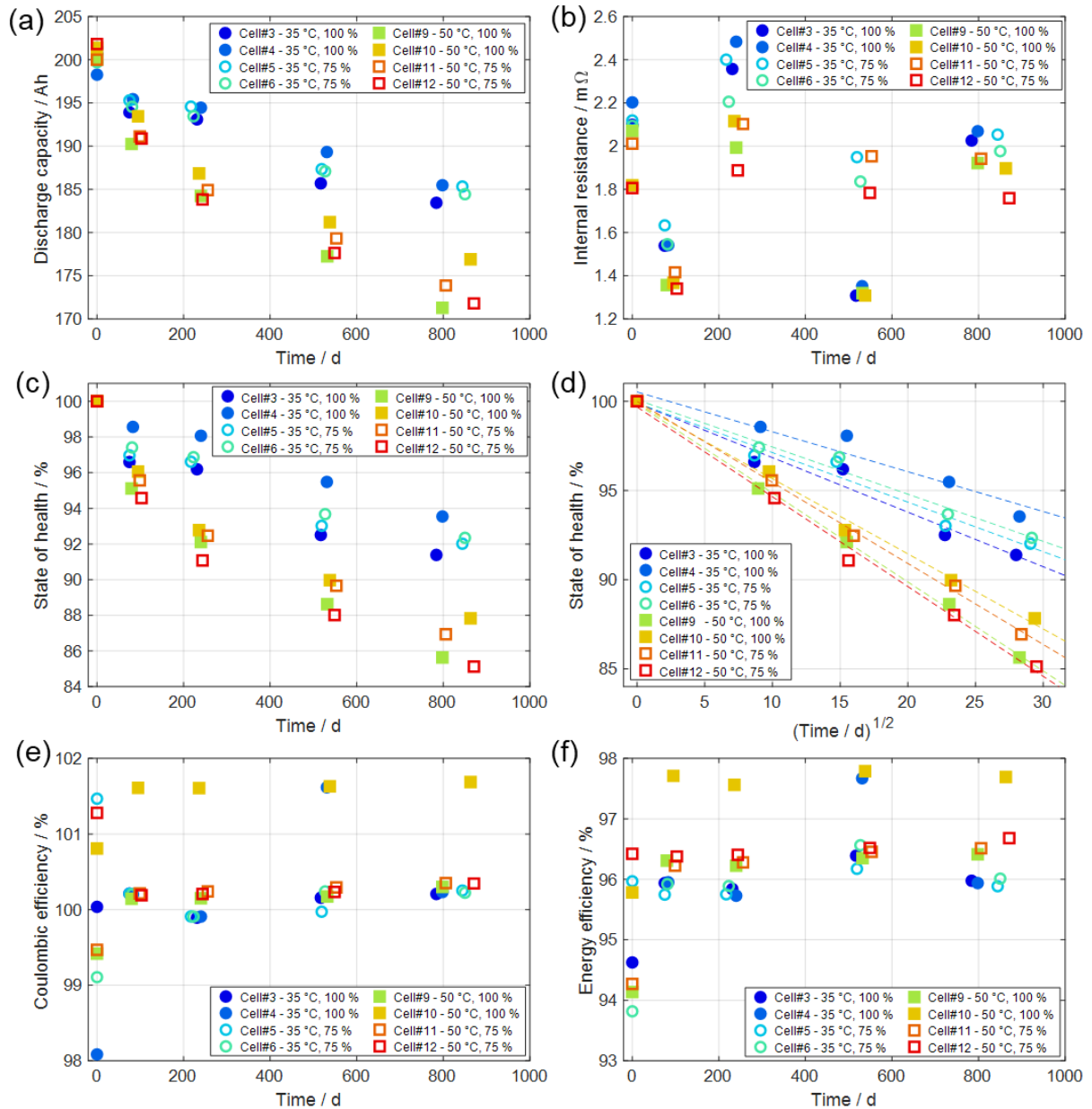


Figure 35: Quantitative analysis of the checkup results of calendaric aging cells. Aging conditions (temperature, SOC) are given in legend next to cell numbers. Checkups are performed at 20 °C ambient temperature. (a) Actual discharge capacity  $C_R$ , (b) internal resistance  $IR_{\text{cycle,full}}$  (calculated from Eq. (15)), (c) state of health SOH vs. time, (d) SOH vs.



square root of time, (e) coulombic efficiency ( CE ), (f) energy efficiency (  $\eta_{\text{energy}}$  ).  $C_R$ ,  $IR_{\text{cycle,full}}$ , CE, and  $\eta_{\text{energy}}$  are calculated from checkup CCCV charge/discharge cycles at 0.28C (CV cut-off current: 0.05C) according to the test protocol given in Section 3.6.2.

#### 4.3.4 Degradation modes analysis

Following the end of Calb cell calendaric and cyclic aging tests, the checkup dataset of calendaric and cyclic aging cells and charge/discharge cycles dataset of cyclic cells were investigated by degradation modes analysis described in Section 3.7. The analysis aims to simulate the contribution of possible degradation modes to overall aging. The motivation for degradation mode analysis is to identify dominant aging modes using only experimental data. As a result, we can hypothesize about the possible aging mechanisms responsible for calendaric and cyclic aging.

##### 4.3.4.1 Electrode balances

The results of electrode balances analysis of one exemplary cyclic aging cell (Cell #7 aged at 50 °C) are presented in Figure 36. The figure shows experimental pOCV curves, synthetic OCV curves, and DVA plots at four selected timeframes during cyclic aging tests corresponding to the start of tests (1st cycle), the midpoint of tests (750th cycle), last (1495th) cycle, and the last checkup (checkup #4). In panels (a) and (c), corresponding to the 1st and 750th cycle, well-formed voltage plateaus and steps are visible in the pOCV curves, which translate to clear peaks in the DV curves in panels (b) and (d). Synthetic OCV and DV curves match well with the experimental ones, so the optimization algorithm outputs are accurate. The DV peaks change their position towards lower charge throughput for the older cell; for example, the NE DV peak at ca. 65 Ah 1st cycle in panel (b) shifts to ca. 45 Ah 750th cycle in panel (d), as observed in Figure 33 by continuous narrowing of the respective voltage plateau.

The data for the 1495th cycle (panels (e) and (f)) show a qualitative difference. In panel (e), the steps in the pOCV curve are hardly recognizable. Consequently, in panel (f), the characteristic features of the DV curve become very broad. The NE DV peak, which is initially positioned around 65 Ah, has nearly vanished, except for the tiny peak at ca. 25 Ah. As these peaks serve as a basis for identifying the lithium stoichiometry regions, the optimization algorithm is unable to obtain good results – the DV peak at ca. 25 Ah is shifted to ca. 5 Ah in the synthetic curve, resulting in a poor agreement between experimental and synthetic pOCV. The broadening of DV peaks with consecutive aging is attributed to spatially inhomogeneous aging, leading to a superposition of multiple different half-cell curves [93].

We have observed that high C-rates broaden the characteristic steps in the voltage curve compared to low C-rates (cf. Section 4.1). Therefore, typically, C-rates below 0.1C are used for DVA [98]. The cyclic aging dataset in panels (a-f) consists of CCCV charge/discharge cycles at 0.28C (0.05C CV cut-off) at 50 °C. The checkup data in panels (g) and (h) is measured with CCCV 0.1C (0.05C CV cut-off) at 20 °C. Despite the lower C-rate, the DV peaks are broader in panel (h). Still, the optimization algorithm is able to converge to a better agreement between experimental and synthetic pOCV curves, as seen in panel (g).

The DV peaks are used to calculate lithium stoichiometries throughout the aging tests. However, the broadening of peaks (as in panels (f) and (h)) beyond identifiable limits hinders the calculation of Li stoichiometries. The electrode balance analysis of all cyclic aging cells demonstrates that the peak identifiability of cells aging at 50 °C is lost after ca. 1000 cycles, corresponding to ca. 83 % SOH (cf. Figure 34(c)). On the other hand, the broadening of peaks beyond identifiability does not occur for 35°C cyclic aging cells, allowing the calculation of the lithium stoichiometries until the end of the test. At the end of tests, the SOH of cells cycled at 35 °C are 86 % and 88 %, so their SOH is still above 83%, where peak broadening reached beyond identifiable limits for 50 °C cyclic aging cells. Thus, we can conclude that the presented methodology allows the calculation of lithium stoichiometries of cyclic aging cells under investigation up to capacity loss of about 17 %.

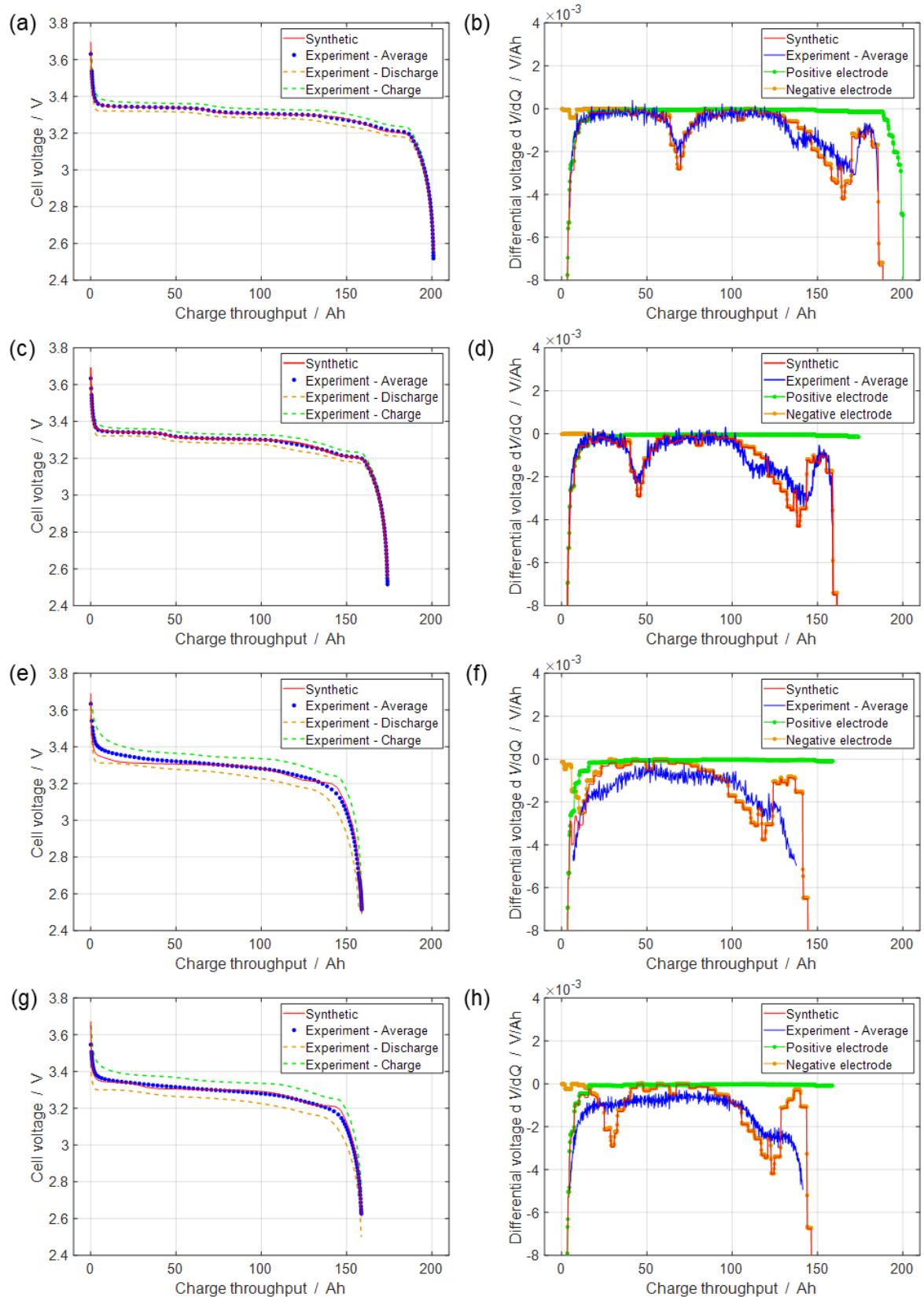


Figure 36: Electrode balances analysis results of exemplary cycling data and last checkup of Cell #7. Left panels (a), (c), (e), (g): Experimental charge, discharge, charge/discharge average (pseudo-OCV) curves, and synthetic OCV curve. Right panels (b), (d), (f), (h): DV curves of

experimental pOCV curve, synthetic OCV curve, and individual electrodes. (a-b) 1st cycle, (c-d) 750th cycle, (e-f) 1495th (last) cycle, (g-h) last checkup (#4) performed at the end of cycling. All cycles were performed with the CCCV test protocol with 0.28C (0.05C CV cut-off current) at 50 °C, and the checkup capacity test was performed with the CCCV test protocol with 0.1C (0.05C CV cut-off) at 20 °C.

#### 4.3.4.2 Quantification of cyclic aging cells degradation modes

The lithium stoichiometries of individual electrodes were calculated via electrode balances analysis from the optimization of pOCV and DV curves for all cycles (cf. 4.3.4.1). The results of stoichiometric analysis, quantification of LAM and LLI degradation modes for all cyclic aging cells are presented in Figure 37. The cyclic aging temperatures of the cells are given next to cell numbers in the legend of each plot. Figure 37(a-d) shows the minimum and maximum lithium stoichiometries of PE and NE as a function of cycle number. Two types of data sets are shown in the figure. The continuous data points (dots) represent the cycle-by-cycle analysis of cyclic aging data of CCCV cycles performed with 0.28 C (0.05C CV cut-off current) at 50 °C or 35 °C. The individual data points (circles) represent capacity test cycles performed with 0.1C CCCV (0.05C CV cut-off current) cycles performed during checkups (after 500, 1000 and 1500 cycles) at 20 °C.

According to lithium stoichiometry analysis, NE (b) is almost completely delithiated in a fully discharged cell. Similarly, in a fully charged cell, hardly any lithium ions are left in PE (d). In both cases (b) and (d), there is not much difference between the cyclic data and the checkups. However, the determined lithium stoichiometry values from the checkups are generally slightly higher than those from the cyclic aging data.

PE maximum lithium stoichiometry ( $X_{PE}^{max}$ ) traces (c) start at about 99 % lithiation for all cells, indicating that PE dictates the usable cell capacity. The lithiations decrease with age and are very similar to the capacity curves in Figure 34. This similarity can be explained by Eq. (37). As discussed above, PE minimum lithium stoichiometry ( $X_{PE}^{min}$ ) behaves quite constant with values close to zero and has hardly any influence on the result. Therefore,  $X_{PE}^{max}$  is approximately proportional to the cell capacity with respect to the initial theoretical PE capacity ( $\frac{C_{cell}(t)}{C_{PE}^0}$ ). However, it was assumed in Section 3.7.2.3 that the PE itself does not age (no loss of active material), so its theoretical capacity remains constant. Under this assumption, the decrease of  $X_{PE}^{max}$  is resulting from the capacity loss due to the loss of cyclable lithium ( $Q_{LLI}$ ) during the aging process.

When the maximum lithium stoichiometries of NE ( $X_{NE}^{max}$ ) (a) are considered, it is noticeable that these show a lower relative lithiation than PE during the aging process, which also shows that PE determines the usable cell capacity. Again, a decrease in lithiation with increasing cycles is evident. All cells start at a maximum lithiation of just under 80 %, which can be explained by the oversized NE. In the case of the two 50 °C cells, a loss of active material could be suspected after the 800th cycle since the lithium stoichiometry does not drop further. Besides, an increase until 1000 cycles can be observed. However, an opposite behavior is seen after the 1000th cycle with a sharp drop. This behavior is unrealistic and can be attributed to the incorrect identifiability of the lithium stoichiometry values using the electrode balancer. No such strong decreases occurred from the checkup data of the 50 °C cells, which were carried out at lower C-rates. Here, a relatively constant decrease of the upper lithium stoichiometry between the individual checkups is recognizable. These smaller decreases appear more realistic. Hence, the aging parameters can be better determined when the battery tests are run at lower C-rates. For the 35 °C cells, no significant discrepancies between the cyclic data and the checkups are apparent. It is clear from the curves shown that the absolute lithium stoichiometry decreases with increasing age.

Figure 37(e) and (f) show the loss of active material of the negative electrode  $Q_{LAM,NE}$  (Eq.(26)) and loss of lithium inventory  $Q_{LLI}$  (Eq. (32)), respectively, as a function of cycle number. The results are shown additionally as a function of time in panels (g) and (h). In order to scale the  $Q_{LAM,NE}$  and  $Q_{LLI}$  plots (panels e-h) equally for better comparison, these data are plotted within the same capacity ( $y$ -axis) limits. In panel (e), after 1000 cycles, most of the 50 °C cyclic aging cell values are missing. Due to the incorrect identification of  $X_{NE}^{max}$  starting at about 1000 cycles in the cyclic test data of the 50 °C cells, NE capacity changing with time  $C_{NE}(t)$  according to Eq. (22) can no longer be determined correctly. This is because  $\Delta X_{NE}(t)$  drops suddenly, causing  $C_{NE}(t)$  to increase rapidly, although it should decrease with time. As a result,  $Q_{LAM,NE}(t)$  becomes negative according to Eq. (26) while  $C_{NE}(t) > C_{NE}^0$ . So, the missing values are negative and do not represent realistic results but limitations of electrode balances analysis.

On the other hand, there are no missing or unrealistic values for 50 °C cyclic aging cells in panel (f), although miscalculated  $C_{NE}(t)$  is included in the calculation of  $Q_{LLI}$  according to Eq. (32). The reason is that  $C_{NE}(t)$  is used in the equation in multiplication with  $X_{NE}^{max}(t)$ . According to Eq. (22) if the stoichiometry range decreases unrealistically (*e.g.*, accommodating little or no change in cell capacity), the anode capacity must increase accordingly. As a result, their product still gives the cell capacity. In other words, the absolute

amount of lithium that can be cycled remains unchanged. For this reason,  $Q_{LLI}$  curves can be considered accurate despite the misidentified lithium stoichiometry values.

The NE active material loss ( $Q_{LAM,NE}$ ) is higher for both 50 °C cells than the 35 °C cells throughout the experiment. Similarly, it is noticeable that the 50 °C cells show a significant increase in active material loss after approximately 700 cycles, while the checkup data (measured at 20 °C) do not show any significant changes. On the other hand, the increase in active material is consistent with the shortening of the first discharge voltage plateau (Figure 33(b)) and the shifting of NE DV peak at 65 Ah to 40 Ah (Figure 36(b),(d)). The shortening of the voltage plateau is linked to lower NE active material available for the reaction [88], which is in parallel with our results. For the 35 °C cells, the increase of active material loss sets in at about 1400-1500 cycles. Interestingly, at this point, they have reached about the same SOH (about 87%) as the 50 °C cells at the onset of  $Q_{LAM,NE}$  increase. Due to the oversized anode, the test cells remain unaffected by these charge quantity losses. However, loss of lithiated active material can also result in cyclable lithium loss, which would cause noticeable damage to the cell. Here, for all cyclic aging cells, electrochemical milling can be a prospective mechanism to cause the loss of active material in the late stages of aging via the detachment of particles from conductive carbon black [31].

As expected,  $Q_{LLI}$  plots in (f) and (h) show that higher temperature results in faster LLI. Contrary to  $Q_{LAM,NE}$  plots, no significant discrepancies exist between the results of the cyclic aging cycles and the checkups. It is also noticeable that the curves are similar to the absolute capacity curves (cf. Figure 34 (a)) mirrored on the  $x$ -axis. The absolute capacity loss of cyclic aging cells corresponds to the charge losses attributed to LLI with a deviation of approx. 1 Ah. Therefore, while developing our degradation modes analysis method, the assumptions correspond to reality with a very good approximation. Consequently, we conclude that the SEI formation and irreversible plating on NE is the decisive reason for cell aging.

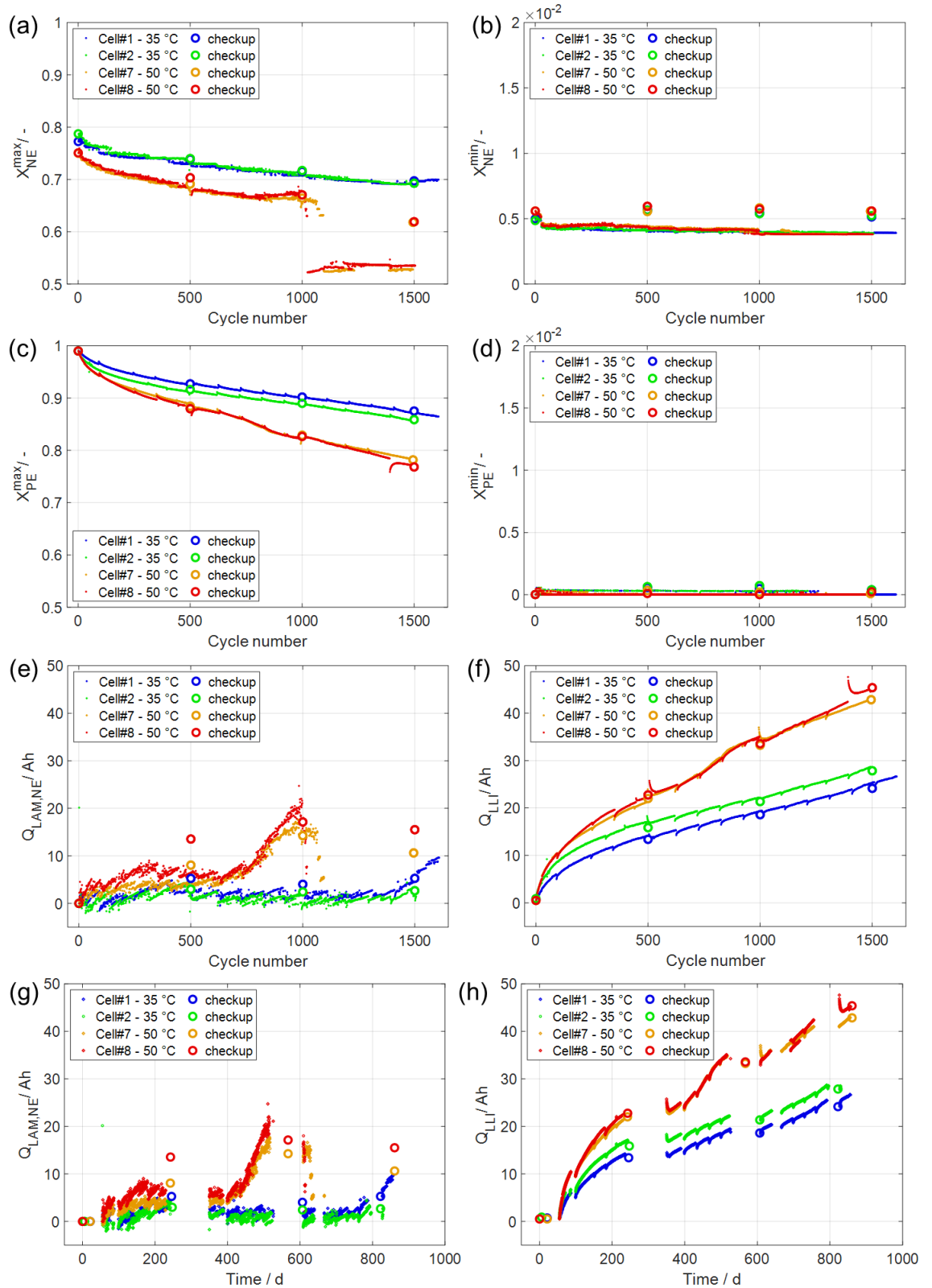


Figure 37: Lithium stoichiometry and degradation modes calculated from electrode balances analysis of cyclic aging cells. Cyclic aging data is represented with dots (aging temperature is given next to cell number in legends), and checkup data (at 20 °C) is represented with circles. (a) Maximum NE stoichiometry, (b) minimum NE stoichiometry, (c) maximum PE

stoichiometry, (d) minimum PE stoichiometry. (e)  $Q_{LAM,NE}$  vs. cycle number, (f)  $Q_{LLI}$  vs. cycle number, (g)  $Q_{LAM,NE}$  vs. time, (h)  $Q_{LLI}$  vs. time. All cycles were performed with the CCCV test protocol with 0.28C (0.05C CV cut-off current), and checkups were performed with the CCCV test protocol with 0.1C (0.05C CV cut-off).

#### 4.3.4.3 Quantification of calendaric aging cells degradation modes

Charge/discharge data is only available during period checkups for calendaric aging cells. Therefore, identical to the protocol for cyclic aging cells, lithium stoichiometry calculations and degradation mode analysis were performed using DVA and pOCV curves recorded during period checkups. Figure 38 (a-d) shows the NE and PE lithium stoichiometries variation. Maximum lithium stoichiometry values of both (a) NE ( $X_{NE}^{max}$ ) and (c) PE ( $X_{PE}^{max}$ ) continuously decreases for 50 °C cells and stays constant or decreases for 35 °C with aging. The decrease is always higher for 50 °C cells, regardless of floating SOC. The reduction of the stoichiometric range indicates capacity loss, which is directly proportional to aging. Thus, lower maximum stoichiometries can be regarded as proof of faster aging at 50 °C. Besides, the results indicate that SOC has little effect on the stoichiometric parameters compared to temperature.

Minimum NE stoichiometry ( $X_{NE}^{min}$ ) (b) remains constant after an initial increase for all cells, while the minimum PE stoichiometry values  $X_{PE}^{min}$  (d) increase slightly with aging. Despite the increase, the  $X_{NE}^{min}$  and  $X_{PE}^{min}$  do not exceed 0.0013 and 0.006, respectively. Consequently, similar to the cyclic aging cells, PE is almost completely delithiated at the end of charging, and NE is almost completely delithiated at the end of discharging processes.

In panel (e), NE active material loss ( $Q_{LAM,NE}$ ) values fluctuate irregularly around 10 Ah after the initial increase detected in checkup#1. The standard industrial manufacturing practice of LFP cells and our measurements (cf. Section 4.1.2) confirm that the NE area is larger than PE (on average, 5.3 % larger according to our measurements). Due to the oversized NE (“anode overhang”), NE capacity does not become smaller than the PE capacity during aging. Therefore, PE capacity is the determining factor of cell capacity. For this reason, the usable capacity of all test cells is unaffected by NE active material losses, similar to cyclic aging cells.  $Q_{LLI}$  plot in panel (f) demonstrates a continuous increase for 50 °C cells with aging, regardless of storage SOC. For 35 °C, after the initial increase to ca. 10 Ah is observed in checkup #1, the values stay stagnant except for a small incrementation to ca. 12 Ah at the end of measurements. Therefore, the ambient temperature has a more significant effect on LLI than storage SOC for the calendaric aging cells. Comparing  $Q_{LAM,NE}$  (e) and  $Q_{LLI}$  (f) shows that the



LLI via SEI formation and irreversible Li plating is the more pronounced aging mechanism for calendaric aging cells, especially after ca. 575 days. This effect is more pronounced for 50 °C cells.

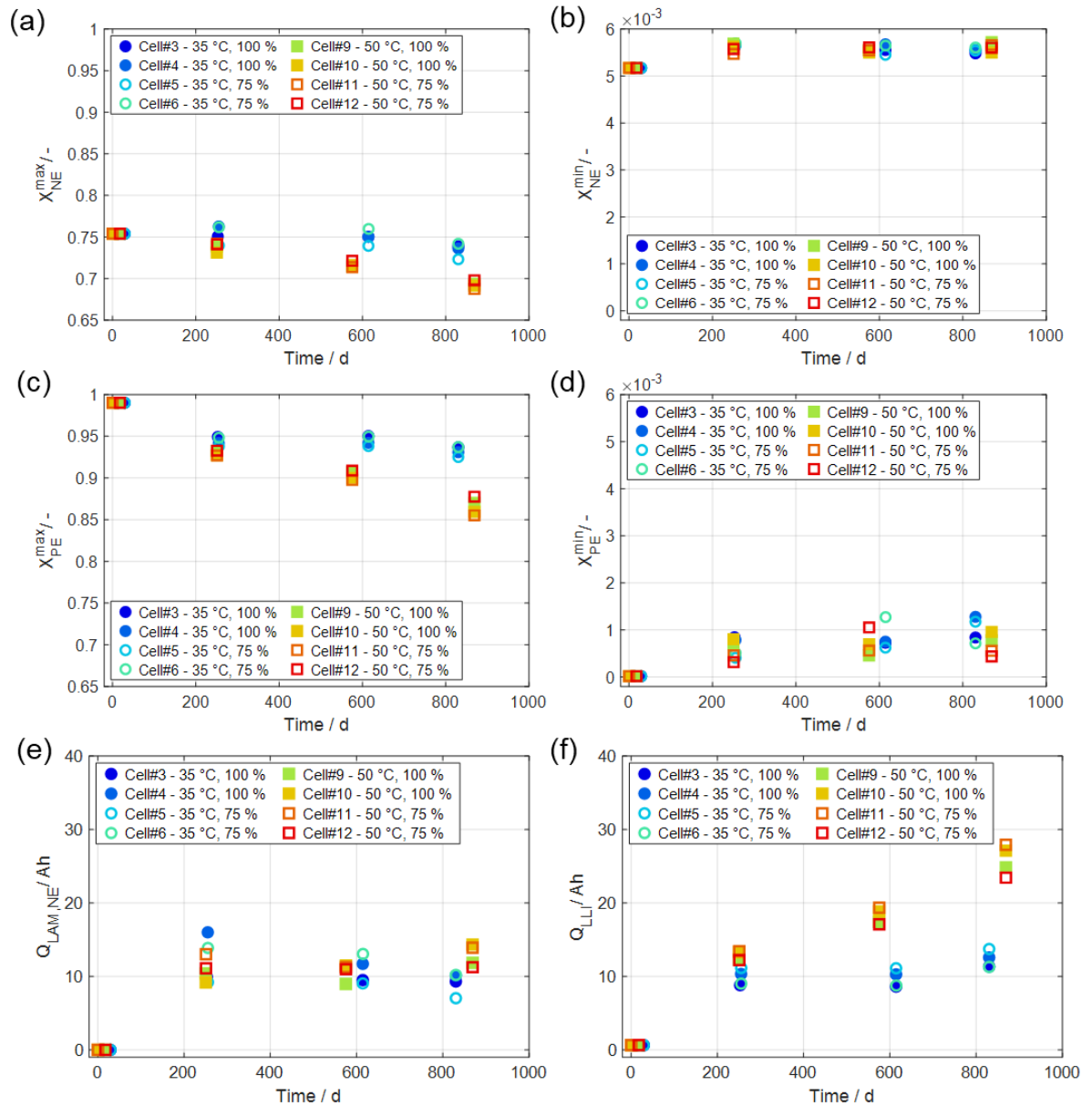


Figure 38: Li stoichiometry and degradation modes calculated from electrode balance analysis of calendaric aging cells checkup measurements (performed at 20 °C). (a) Maximum NE stoichiometry, (b) minimum NE stoichiometry, (c) maximum PE stoichiometry, (d) minimum PE stoichiometry, (e)  $Q_{LAM,NE}$  vs. time, (f)  $Q_{LLI}$  vs. time. All checkups are performed using the CCCV test protocol with 0.1C (0.05C CV cut-off).

### 4.3.5 Discussion

The objectives of the calendaric and cyclic aging tests on the cell level are investigating the influence of operating conditions on aging, comparing individual effects of calendaric and cyclic aging on overall cell lifetime, and quantifying the degradation modes by using experimental data. In Figure 39, we compare the SOH, IR,  $LAM_{NE}$ , and LLI of all 12 cells.

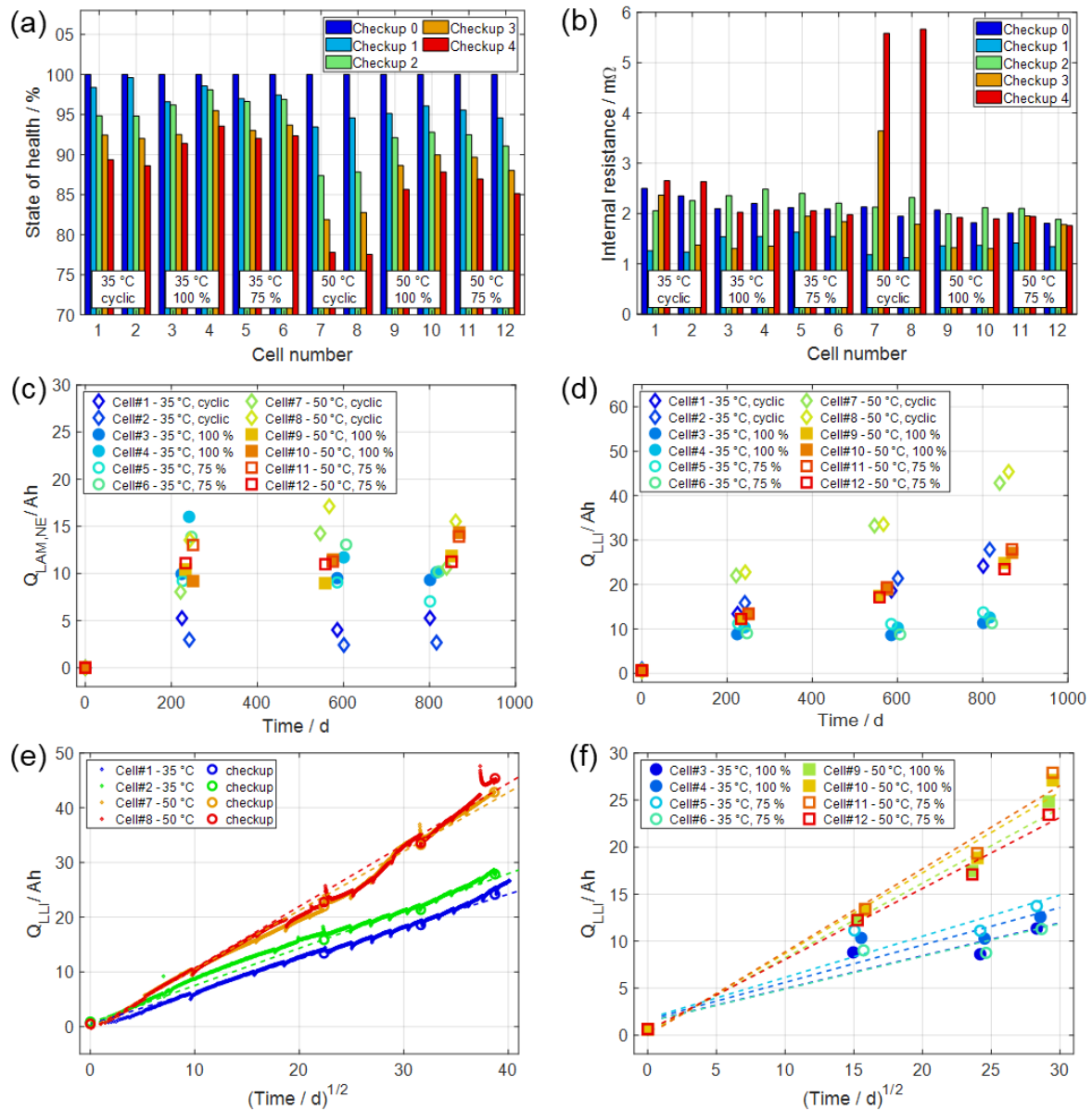


Figure 39: Comparison of calendaric and cyclic aging cells aging indicators and degradation modes. (a) SOH (b)  $IR_{cycle,full}$  (Eq. (15)) (c)  $Q_{LAM,NE}$  vs. time (d)  $Q_{LLI}$  vs. time (e)  $Q_{LLI}$  vs. square root of cycle number (f)  $Q_{LLI}$  vs. square root of time.

Except for panel (e), only checkup results are presented to be able to compare the results under the same conditions. SOH comparison of aging cells in panel (a) shows that regardless of aging type (cyclic or calendaric) and storage SOC, all cells aged at 35 °C outperform all cells aged at 50 °C in capacity retention at all checkups. Only among the cells aged at identical temperatures does cyclic aging increase capacity loss significantly. Additionally, within calendaric aging cells at both temperatures, no distinctive aging pattern is observed depending on the SOC level of the cells. These results agree with similar calendaric aging tests in literature [80], which state that ambient temperature rather than storage SOC is the dominant factor causing SOH decrease.

The IR of all cells dropped in the first checkup (checkup #1) after aging tests started, which can be attributed to the conditioning behavior observed for LFP cells. In addition, after checkup #2, the IR of cyclic-aging cells at 50 °C increased 2.5 times more than all other cells. However, no such correlation between capacity loss and internal resistance was present for outlier 50 °C cyclic cells for other checkups, and the rest of the cells exhibited high and irregular fluctuations of IR throughout the experiment. Therefore, as mentioned earlier, IR cannot be used as an aging indicator due to inadequate measurement sensitivity of battery cyclers in mΩ level and changes in contact resistances due to mandatory changes of test channels throughout the experiment.

The degradation mode analysis demonstrates that  $Q_{LAM,NE}$  is stagnant for both calendaric and cyclic aging cells after its initial rise, measured during the first checkup (c). Therefore,  $Q_{LAM,NE}$  does not explain the capacity loss of all cells after the first checkup. Moreover, no significant  $Q_{LAM,NE}$  pattern in terms of temperature or aging type (cyclic or calendaric) is observed among the cells. On the other hand,  $Q_{LLI}$  analyses in panel (d) have a good correlation with SOH results. 50 °C cyclic cells have continuously increasing and superior  $Q_{LLI}$  at the end of tests (44.1 Ah on average). The calendaric aging 50 °C cells and cyclic aging 35 °C cells, which have final SOH between 85.1 % – 89.3 %, also have continuously increasing and similar amounts of  $Q_{LLI}$  at the end of experiments – on average, 25.8 Ah and 26 Ah, respectively. The calendaric aging 35 °C cells with final SOH between 91.4 % - 93.6 % have rather stagnant  $Q_{LLI}$  throughout the experiments with a final  $Q_{LLI}$  of 12.2 Ah on average. As a result, we could quantify approximately three aging groups both from SOH measurements and  $Q_{LLI}$  analysis as: 1.) 50 °C cyclic aging cells, 2.) 50 °C calendaric aging cells and 35 °C cyclic aging cells, and 3.) 35 °C calendaric aging cells. In summary, according to our results, LLI is the dominant degradation mode compared to  $LAM_{NE}$ . It is also shown that temperature is the dominant factor in LLI. Furthermore, it was evident that the LLI is more pronounced under cyclic aging at the same temperature.

Panels (e) and (f) show  $Q_{LLI}$  as a function of the square root of the number of cycles for cyclic aging cells and the square root of time for calendaric aging cells, respectively. The dashed straight lines in both panels are linear fits to checkup data generated using the MATLAB Basic Fitting tool. These lines are added to monitor the  $\sqrt{t}$  dependency of  $Q_{LLI}$ . Initially, there is a  $\sqrt{t}$  dependence of  $Q_{LLI}$  for 50 °C cyclic aging cells, which is lost with further aging after ca.  $Q_{LLI} > 15$  Ah for Cell #7 and ca.  $Q_{LLI} > 17$  Ah for Cell #8. One of the 35 °C cyclic cells, Cell #1, shows almost constant linear  $\sqrt{t}$  dependence until ca.  $Q_{LLI} > 21$  Ah except for the slight deviation in the beginning until  $Q_{LLI} > 4$  Ah. The other 35 °C cell, Cell #2, shows a significant deviation from linear fit until ca.  $Q_{LLI} > 18$  Ah, but between ca. 18 Ah – 25 Ah follows strictly  $\sqrt{t}$  dependence, and deviates from the fitted line after  $Q_{LLI} > 25$  Ah. In general, 35 °C cells have  $\sqrt{t}$  dependence longer than 50 °C cells. Under the assumption that LLI is the primary capacity loss mechanism, the deviation from  $\sqrt{t}$  trendline is observed at 90 % SOH for Cell #1, 88 % SOH for Cell #2, 92 % SOH for Cell #7, and 91 % SOH for Cell #8. The aging rate increases and the aging mechanism becomes more complex(multi-mechanism) below ca. 90 % SOH. As a result, we presume that the LLI is not governed by only  $\sqrt{t}$  dependent processes (*e.g.*, diffusion-limited growth of SEI layer), especially in the late stages of aging.

In calendaric aging cells, there is a continuous albeit fluctuating  $\sqrt{t}$  dependency of  $Q_{LLI}$  for 50 °C calendaric aging cells throughout the experiment, independent from storage SOC. On the other hand, after ca. 255 days of testing, 35 °C calendaric aging cells strongly deviate from  $\sqrt{t}$  dependency and  $Q_{LLI}$  is close to 50 °C calendaric aging cells. Until the next checkup in 300 days, the  $Q_{LLI}$  of 35 °C calendaric aging cells remains effectively constant. After that, the  $Q_{LLI}$  of 35 °C cells are increasing close to  $\sqrt{t}$  dependency until the end of experiments. Identical to 50 °C cells, no difference in the  $Q_{LLI}$  pattern is observed between different storage SOC.

For both cyclic and calendaric aging cells, the  $Q_{LLI}$  was higher at 50 °C at the end of the experiments. We presume that 50 °C aging cells continue to lose lithium inventory because of the instability of the passivation layer at elevated temperatures, which can facilitate further SEI layer growth and high temperature-induced electrolyte and electrode degradation [19,84].

#### 4.3.6 Summary

Twelve Calb cells are tested under controlled ambient temperature to investigate the individual effects of temperature and aging type (calendaric and cyclic) on overall cell aging. The comparison of SOH changes throughout periodic reference performance tests (cf. Figure 39(a)) demonstrates that during all stages of the experiment, all cells tested at 50 °C have lower SOH (higher capacity loss) than all cells tested at 35 °C, independent from aging type.

This result shows that the ambient temperature is the dominant operation condition affecting aging on the cell level, as in the case of Sinopoly cells in BESS stacks in Section 4.2. Within the cells tested at the same ambient temperature, cyclic aging cells lose more capacity than calendaric aging cells. The difference in storage SOC causes no distinctive aging pattern between calendaric aging cells tested at the same ambient temperature.

According to our model, the degradation mode analysis of cyclic and calendaric aging tests shows that LLI is the dominant degradation mode. For all cells,  $Q_{LAM,NE}$  stays almost constant after an initial increase.  $Q_{LLI}$  constantly increases for all cyclic aging and 50 °C calendaric aging cells. For cyclic aging cells, there is  $\sqrt{t}$  dependency of  $Q_{LLI}$  until ca. 10 % capacity loss and fluctuating in later stages of aging. For calendaric aging cells, 50 °C cells follow  $\sqrt{t}$  dependency with fluctuations, and 35 °C cells deviate strongly from  $\sqrt{t}$  dependency according to the first checkup results but follow  $\sqrt{t}$  dependency in the following checkups. The degradation analysis results show that, especially at later stages of aging (SOH < 90 %), LLI cannot be explained by a single  $\sqrt{t}$  dependent mechanism.

## 5 SUMMARY AND OUTLOOK

---

### 5.1 SUMMARY

This Ph.D. thesis proposes and demonstrates a methodology for investigating the aging behavior of large-format commercial LFP lithium-ion battery cells. Throughout the measurements, two commercial prismatic large-format LFP/graphite cells with the same nominal capacity (180 Ah) and nominal power (576 Wh) were used. The cells were named after their manufacturers: Sinopoly cells and Calb cells. The methodology consists of three axes: detailed initial characterization of both cells, residential BESS aging with Sinopoly cells, and single-cell calendaric and cyclic aging with Calb cells. In the beginning, the electrical and geometrical cell properties of both cell types were identified. Then, the aging characteristics of Sinopoly cells were monitored at the battery stack level under microgrid operation and the cell level under continuous cyclic at controlled temperature. Finally, individual contributions of calendaric and cyclic aging on overall cell aging are tested with Calb cells in a controlled laboratory environment.

#### 5.1.1 Detailed initial characterization

The main results of electrical, thermal, structural, and chemical characterization of Sinopoly and Calb cells can be summarized as follows:

- The 28 individual cells of each type show a significant capacity scatter, particularly pronounced in the Sinopoly cell. This scatter is problematic if the cells are used in serial battery pack configurations, where balancing units will be required.
- The electrical performance of the two cell types is similar. The charge/discharge characteristics show a weak capacity-rate effect (for investigated C-rates up to 1C) and a strong dependence on temperature (for investigated temperatures between 5 and 35 °C). This behavior is typical for lithium-ion cells.
- Both cells have a high electrical energy efficiency above 90 % of the discharge/charge cycle. The efficiency increases with increasing temperature and decreasing C-rate, with measured values up to 98 % for 35 °C / 0.1C cycles. This excellent efficiency makes the cells well-suited for renewable energy storage applications.
- The internal cell designs, analyzed after cell opening under Argon atmosphere, consist of two electrode stacks with 144 positive and 146 negative electrode sheets. It is remarkable that the electrode sheets are stacked, as would be typical for pouch cells, and not wound in a jelly roll, as is considered typical for prismatic cells [138].
- The nominal specific energy of the cells is 101 Wh/kg, which is low compared to other

high-energy lithium-ion cells. For both cells, the massive PP casing (*e.g.*, 6.2 mm for the Calb cell) has a significant contribution (approximately one-quarter) to the total weight. As the target application of the cells is stationary energy storage, the low specific energy is not problematic.

- The electrode morphologies, as investigated with LM and SEM, show small, sub-micrometer particles for LFP and large, 10-micrometer scale irregularly-shaped particles for graphite. Electrode balance analysis reveals LFP volume fractions of 38.1 % and 44.8 %, and graphite volume fractions of 59.7 % and 55.4 % for the Sinopoly and Calb cells, respectively. The LFP volume fractions are relatively low.
- Chemical analysis with EDX confirms the LFP/graphite cell chemistry. The positive electrodes contain significant amounts of carbon as conductive additives. The presence of carbon additives in the positive electrode is consistent with the observed low LFP volume fractions, contributing to the overall low specific energy.
- The electrode balances were determined with a mathematical optimization algorithm. The negative electrodes were cycled to lithium stoichiometries up to 64 % and 75 % for the Sinopoly and Calb cells, respectively. The difference is a consequence of different electrode loading but is also related to the significantly different cut-off voltages specified by the manufacturers. Therefore, a significant part (1/3 to 1/4) of the graphite capacity was unused. Furthermore, the two cell types show an anode overhang [121] of 4.9 % and 5.7 %, respectively. Reduced cycling stoichiometry and anode overhang are known strategies to reduce plating propensity and, therefore, increase cell lifetime [28,138].
- The combined empirical data and mathematical analysis resulted in a complete and self-consistent parameter set of the two cell types. These parameters are requirements for follow-up modeling and simulation studies of these cells, such as physicochemical and equivalent circuit models.

### 5.1.2 Residential BESS aging

The aging characteristics of full-scale 8 kWh commercial residential BESS (constructed with Sinopoly cells) were investigated at cell, battery, and microgrid levels. Specifically, two different battery architectures were compared, one with serially-connected cells and one with cells connected in parallel. The battery systems were operated over an extended period (ca. 2.5 years, ca. 850 equivalent full cycles). Single-cell characteristics were quantified initially and during periodic checkups. The key results of the investigations are:

- All cells show significant and continuous capacity loss. The average capacity loss after 2.5 years of battery operation was 18.6 % and 21.4 % for serial and parallel configuration cells, respectively. At the same time, the cells showed a decrease in internal resistance.

- A single cell operated with continuous full cycles showed significantly less capacity loss (factor of two) than the cells in the system. The difference is probably caused by the higher temperature of the cells in the system compared to the cell in the climate chamber. Therefore, improving the thermal management on the battery level (*e.g.*, by integrating active cooling strategies) can probably significantly improve cell lifetime.
- The difference in capacity loss between the serial and parallel battery architectures is only small and likely due to the higher and presumably more inhomogeneously distributed cell temperatures in the system with parallel architecture. Higher temperatures may result from higher ohmic losses in the current collection rails due to significantly higher currents than the serial architecture.
- Considering that the parallel system was built up by individual cells with considerable initial capacity variation, this architecture can offer a promising economic advantage of using cells from different production batches or stages of health together in the same battery stack.

### 5.1.3 Single-cell calendaric and cyclic aging

The comparison of the effect of aging type (cyclic or calendaric), temperature (35 °C or 50 °C), and storage SOC (75 % or 100 %) on overall cell aging was performed by testing twelve Calb cells under controlled ambient temperature for 1500 cycles (cyclic aging cells) or 850 days (calendaric aging cells). The main observations at the end of the experiments are the following:

- Capacity fade is the primary aging indicator for both calendaric and cyclic aging. Regardless of aging conditions, all twelve cells lost significant capacity over time.
- Cyclic aging cells tested at 35 °C lost, on average, 13 % of their initial capacity, whereas the cyclic aging cells tested at 50 °C lost, on average, 22 % of their initial capacity at the end of the experiment. 50 °C cyclic aging cells reached the “end of life” (20 % capacity loss) at ca. 1350 cycles. According to the results, 35 °C cyclic aging cells demonstrate superior capacity retention.
- All calendaric aging cells tested at 50 °C lost higher capacity (ca. 14% on average) than calendaric aging cells tested at 35 °C (ca. 8 % on average), independent of storage SOC level.
- The SOH comparison of calendaric and cyclic aging cells reveals that even calendaric aging cells at 50 °C have lower SOH than cyclic aging cells at 35 °C at the end of experiments. Thus, we conclude that ambient temperature is the determining operating condition on aging, independent of aging type (calendaric or cyclic).



- At the same temperature, cyclic aging cells lose more capacity than calendaric aging cells. No distinctive effect of storage SOC on calendaric aging is observed at both temperatures.
- The increase of internal resistance as a distinctive aging indicator is only observed after the end of life (SOH < 80%) is achieved by 50 °C cyclic aging cells.
- The investigation of SOH reduction demonstrates that 50 °C calendaric aging cells show straight linear decay with the square root of time during all checkups. It is not possible to observe any consistent linear decay pattern for 35 °C calendaric aging cells. For all cyclic aging cells, linear decay is present until ca. 400th cycle, followed by a considerable deviation.
- The energy efficiencies of 35 °C cyclic aging cells are constantly above 97 %. In the first 1000 cycles, the energy efficiencies of 50 °C cyclic aging cells are above 98 %, but after the efficiencies drop to 96 % as internal resistances of the cells increase significantly. Energy efficiencies of all calendaric aging cells are nearly constant during checkups, with minor fluctuations between 96-98 %. Coulombic efficiency is close to unity for cyclic and calendaric aging cells throughout tests.
- For all twelve cells,  $Q_{LAM,NE}$  is almost constant throughout the aging tests, and no visible pattern representing the effects of temperature or cycling type can be identified. On the other hand,  $Q_{LLI}$  plots are in good correlation with SOH results. Therefore, we presume that loss of lithium inventory rather than loss of active material at NE is the primary degradation mode of the investigated cells.
- The linear  $\sqrt{t}$  dependency of  $Q_{LLI}$  is observed until ca. 10 % capacity loss for all cyclic aging cells. For calendaric aging cells: 50 °C cells follow linear  $\sqrt{t}$  dependency with fluctuations, and 35 °C cells deviate strongly from  $\sqrt{t}$  dependency according to the first checkup results but follow  $\sqrt{t}$  dependency in the following checkups. The degradation analysis results show that, especially at later stages of aging (SOH < 90 %), LLI cannot be explained by a single  $\sqrt{t}$  dependent mechanism but a more complex (multi-mechanism) aging process.

## 5.2 CONCLUSION

The multi-level methodology for determining the aging characteristics of commercial large-format LFP lithium-ion cells is successfully demonstrated using Sinopoly and Calb cells. The initial characterization of both cells shows that the two cell types show strong similarities concerning electrical performance, internal design, cell chemistry, and differences in electrode morphology and balances. Thus, before generalizing any aging analysis methods,

the unique differences resulting from different designs and manufacturing of commercial cells must be considered.

Following the initial characterization, Sinopoly cells underwent commercial BESS aging tests. To the best of our knowledge, this is the first time that the aging of commercial large-format (180 Ah) stationary storage cells has been investigated with full-scale residential BESS under realistic operation for around 2.5 years, along with periodic reference performance tests of each cell. Moreover, two different battery stack architectures (parallel and serial) with opposite voltage and current characteristics were compared under the same load conditions. The results show that no system architecture is superior, so using parallel architecture can increase cost efficiency by allowing the use of cells with different aging histories together due to passive balancing currents.

The comparison of the capacity losses of serial and parallel system cells to a continuously cycling single Sinopoly cell at a constant 20 °C ambient temperature demonstrates that the single cell has higher capacity retention despite a higher charge/discharge current rate. According to this comparison, cell temperature is presumed to be the dominant aging parameter regardless of all other aging conditions.

Finally, the influence of individual operating conditions (temperature and SOC) and aging types (calendaric or cyclic) on overall cell aging was tested with single Calb cells. Independent of the other test conditions, all cells (calendaric or cyclic) tested at 50 °C lost more capacity than those tested at 35 °C. These results further confirm that higher temperatures accelerate aging, independent of the aging type and storage SOC. At the same temperature, cyclic aging increases capacity loss compared to calendaric aging. No distinguishable effect of storage SOC can be observed among calendaric aging cells.

The dominant effect of temperature on cell degradation must be emphasized for the economic aspect of this study. Sinopoly and Calb cells are used in stationary storage systems. The results suggest that efficient thermal management can considerably improve their commercial lifetime. Therefore, it is economically favorable for manufacturers and customers to invest in the thermal management of battery stacks. Furthermore, economically feasible stationary storage systems can be constructed with parallel stack architecture using cells with different usage histories (possibly recycled batteries) in the same battery stack without significant capacity loss disadvantages.

Overall, the long-term and multi-level aging investigation of 40 large-format (180 Ah) commercial LFP lithium-ion cells presented in this Ph.D. thesis is one of the pioneer studies in the field. As mentioned before, the majority of the aging studies in the literature are

performed with <10 Ah cells, whose aging performance may not represent the aging profile of large-format cells. Therefore, in addition to the scientific community, this Ph.D. thesis contributes to the battery industry by providing a complete aging dataset of commercial large-format cells along with suggestions about stack design and operation modes to favor long lifetime.

### **5.3 OUTLOOK**

The aging investigation method in this thesis provided consistent results validated by post-processing analyses. However, the method can be further improved in future studies. The repetition of initial geometrical and electrode microstructure analyses of the same commercial cell at different stages of aging can provide sequential information on morphological changes of active materials, such as particle size distribution and evolution of passivation layers. In parallel, EDX analysis can determine electrode and electrolyte degradation products and their total amount. Moreover, spatial differences in aging can be monitored by comparing the electrode samples from the center and the outer layers of the electrode stack.

In this study, internal resistance results are not used as a primary aging indicator, partially due to insufficient measurement resolution due to the sub-milliohm internal resistances of large-format cells. Similarly, due to the lack of measurement quality, electrochemical impedance spectroscopy (EIS) measurement results are not used. Ideally, in sub-milliohm levels, contact resistances of measurement probes must be constant for each periodic checkup throughout the experiment to be eliminated at the end of measurements, which was not possible in our experimental setup due to the limited number of available test channels. For accurate IR and EIS analysis on aging, sophisticated experimental setups must be built to perform in-situ IR and EIS measurements without replacing contacts throughout experiments.

## 6 APPENDICES

---

### 6.1 OWN PUBLICATIONS

#### 6.1.1 Journal Articles

1. M. Mayur, M. C. Yagci, S. Carelli, P. Margulies, D. Velten, and W. G. Bessler, “*Identification of stoichiometric and microstructural parameters of a lithium-ion cell with blend electrode,*” *Physical Chemistry Chemical Physics*, 21 (42), 23672–23684 (2019).
2. S. Carelli, M. Quarti, M. C. Yagci, and W. G. Bessler, “*Modeling and Experimental Validation of a High-Power Lithium-Ion Pouch Cell with LCO/NCA Blend Cathode,*” *Journal of The Electrochemical Society*, 166 (13), A2990-A3003 (2019).
3. M. C. Yagci, R. Behmann, V. Daubert, J. A. Braun, D. Velten, and W. G. Bessler, “*Electrical and Structural Characterization of Large-Format Lithium Iron Phosphate Cells Used in Home-Storage Systems,*” *Energy Technology*, 9 (6), 2000911 (2021).
4. M. C. Yagci, T. Feldmann, E. Bollin, M. Schmidt, and W. G. Bessler, “*Aging Characteristics of Stationary Lithium-Ion Battery Systems with Serial and Parallel Cell Configurations,*” *Energies*, 15 (11), 3922 (2022).
5. M. C. Yagci, O. Richter, R. Behmann, and W. G. Bessler, “*Degradation modes of large-format stationary-storage LFP-based lithium-ion cells during cyclic and calendaric aging,*” submitted to *Journal of Energy Storage* (2024).

#### 6.1.2 Conferences

1. M. C. Yagci, P. Margulies, B. Weißhar, S. Herberger, D. Velten, and W. G. Bessler, Poster presentation: “*Experimental and modeling study of a lithium-ion pouch cell with LCO/NCA blend cathode. Part 1: Parameterization by in-situ and ex-situ experiments*”, Kraftwerk Batterie, Münster, Germany (2018).
2. M. C. Yagci, P. Margulies, B. Weißhar, S. Herberger, D. Velten, and W. G. Bessler, Poster presentation: “*Cell lifetime diagnostics and system behavior of stationary LFP/graphite lithium-ion batteries*”, 19th International Meeting on Lithium Batteries (IMLB 2018), Kyoto, Japan (2018).
3. M. C. Yagci, T. Feldmann, E. Bollin, and W. G. Bessler, Oral presentation: “*Cell-Level and Stack-Level Aging of 180 Ah Stationary Storage LFP Lithium-Ion Cells Under Laboratory and Microgrid Operation*”, Electrochemical Conference on Energy and the Environment (ECEE 2019), Glasgow, United Kingdom (2019).
4. J. A. Braun, M. C. Yagci, and W. G. Bessler, Poster presentation: “*Equivalent circuit model of a 180 Ah LFP/graphite home storage cell*” Kraftwerk Batterie, Münster, Germany (2020)

## **6.2 BATTERY DATA SHEETS AND DOCUMENTATION**

In this section, the essential pages of the product brochure [139], datasheets [100,101], and material safety data sheets (MSDS) [140,141] of Sinopoly and Calb cells are presented.

## 6.2.1 Sinopoly product brochure

# Sinopoly

http://www.sinopolybattery.com

HK Head Office

Tel: (852) 3104 2803

Fax: (852) 2877 0628

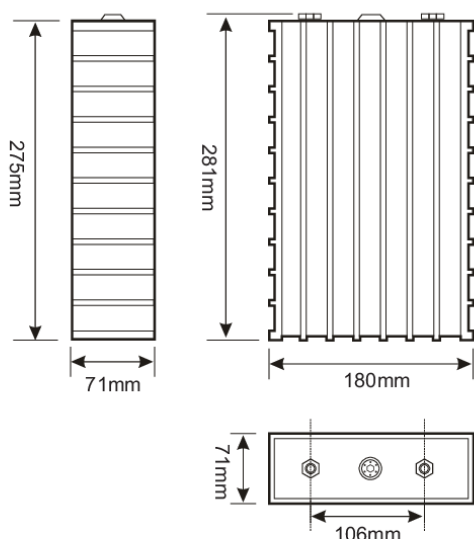
E-mail: sales@sinopolybattery.com

## 中聚锂电池性能说明 SINOPOLY LITHIUM ION BATTERY SPECIFICATIONS

### 单体电池尺寸 DIMENSIONS



型号(MODEL):SP-LFP180AHA



### 技术参数 SPECIFICATION

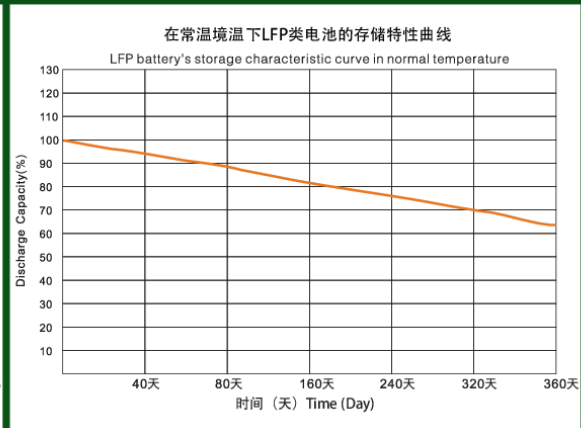
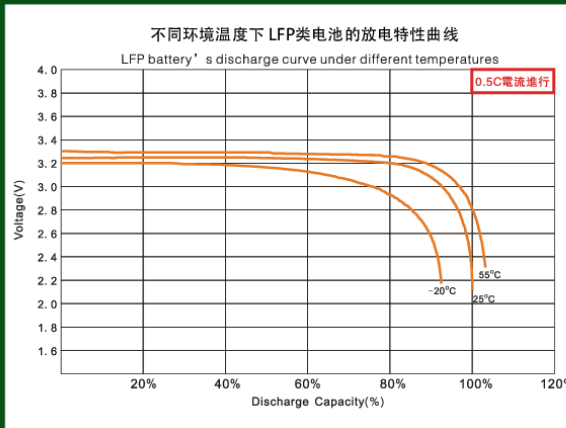
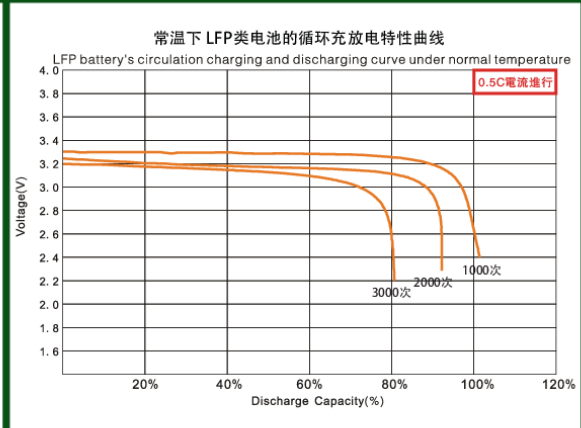
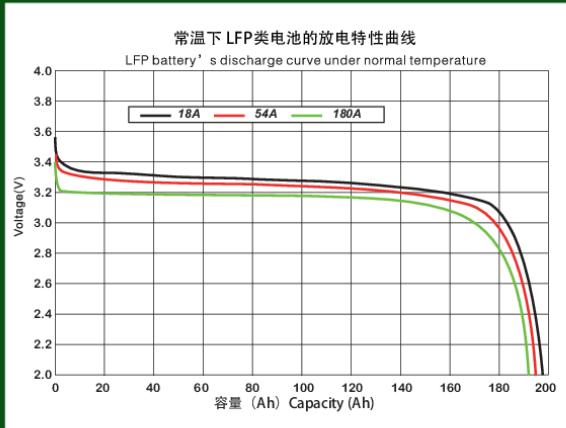
型号(MODEL):SP-LFP180AHA

标称容量 Nominal Capacity	180Ah,576Wh
标称电压 Nominal Voltage	3.2V
循环寿命 Life Cycles	80% DOD $\geq 2000$ Times
	70% DOD $\geq 3000$ Times
自放电率 Self-discharge Rate	$\leq 3\%$
重量 Weight	5.79 $\pm$ 0.1kg

	充电 Charge (模式 Mode:cc-cv)	放电 Discharge
截止电压 Cut-Off Voltage	3.8V	2.8V
标准电流 Standard Current	0.3C,54A	0.3C,54A
最大恒电流 Max Constant Current	3C,540A	3C,540A
最大脉冲电流(10秒) Max Impulse Current (10s)	3C,540A	5C,900A
工作温度 Operating Temperature	0°C ~ +70°C	-20°C ~ +70°C

# SP-LFP180AHA型电池的充放电特性

## SP-LFP180AHA CHARGE & DISCHARGE CHART



## 6.2.2 Sinopoly cell datasheet

 <b>Sinopoly</b>	<b>Product specification</b>	DOC NO.: <u>R100-QSI-008</u>
		REV. : <u>A/00</u>
		SHEET : <u>- 1 -</u> of <u>9</u>

### **Product specification for 3.2V/180Ah Lithium-ion Rechargeable Cell**

**Cell Type: SP-LFP180AhA**

**Shenzhen Sinopoly battery Co., Ltd.**



## Contents

- 1. Scope**
- 2. Cell type and explanation**
- 3. Definitions**
  - 3.1 Normal capacity
  - 3.2 Standard charging method
  - 3.3 Standard discharging method
  - 3.4 Quick charging method
  - 3.5 Quick discharging method
- 4. Cell Structure**
- 5. Cell specification**
- 6. Technical characteristic**
  - 6.1 Cell working temperature
  - 6.2 Cell testing conditions
  - 6.3 Requirement of the testing equipment
  - 6.4 Electrochemistry performance
  - 6.5 Environmental characteristics
  - 6.6 Safety characteristics
- 7. Warning and cautions in handing the Lithium-ion Cell**
- 8. Free-responsibility declaration**
- 9. Contact information**

## 1. Scope

This product specification covers the type, size, structure, electrochemistry performance, environmental characteristics, warning and caution of the SP-LFP180AhA single cell. This PS only applies to the cells that supplied by Shenzhen Sinopoly battery Co., Ltd. .

## 2. Cell type and explanation

SP LFP - 180Ah A  
 i ii iii iv v

- i : “SP” represents manufactory (Shenzhen Sinopoly battery Co., Ltd.)
- ii : “LF” represents the cathode material type of the cell is LiFeYPO<sub>4</sub>
- iii: “P” represents the structure of the single cell is prismatic
- iv: “180Ah” represents the normal capacity of the single cell is 180Ah
- v : “A” represents the cathode and anode terminal in the same direction

## 3. Definitions

### 3.1 Normal Capacity

Normal Capacity is 180.0Ah, cells shall be tested at 20±3℃, 65±20%RH, it means the capacity value of being discharged by 3-hours ratio to the cut-off voltage 2.8V, which is signed as C<sub>3</sub>, the unit is Ah.

### 3.2 Standard charging method

The cell is to be conditioned at 20±3℃, 65±20%RH, charging the battery with 1/3C<sub>3</sub>A(60.0A) constant current to 3.8V, then 3.8V constant voltage charge with current taper to 0.02C<sub>3</sub>A(3.6A).

### 3.3 Standard discharging method

Full charged cell is to be conditioned at 20±3℃, 65±20%RH, discharging the cell with 1/3C<sub>3</sub>A(60.0A) constant current to 2.8V.

### 3.4 Quick charging method

The Cell is to be conditioned at 20±3℃, 65±20%RH, charging the Cell with 3.0C<sub>3</sub>A(540.0A) constant current to 3.8V, then 3.8V constant voltage charge with current taper to 0.02C<sub>3</sub>A(3.6A).

### 3.5 Quick discharging method

Full charged cell is to be conditioned at 20±3℃, 65±20%RH, discharging the cell with 3.0C<sub>3</sub>A(540.0A) constant current to 2.8V.

## 4. Cell structure

The cell consists of the cathode electrode, anode electrode, separator, electrolyte, foil, plastic product, etc.

## 5. Cell specification

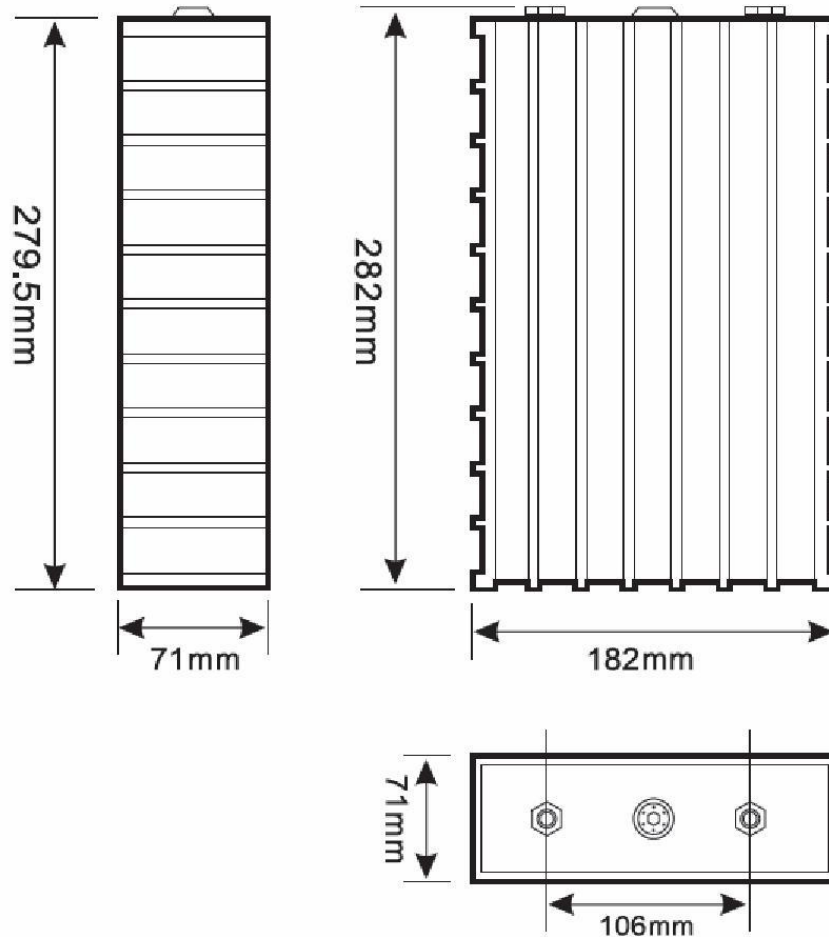
Item	Specification
Max Weight	5.7Kg



## Product specification

DOC NO.: R100-QSI-008REV. : A/00SHEET : - 4 - of 9

Cell dimension	Thickness : 71.0 mm Max Width : 182.0mm Max Length : 282.0mm Max
Normal capacity	180.0Ah@1/3C <sub>3</sub> A(60.0A)
Normal voltage	3.2 V
Charging cut-off voltage	3.8±0.05 V
Discharging cut-off voltage	2.8±0.05 V
Standard charging current	1/3C <sub>3</sub> A(60.0A)
Standard discharging current	1/3C <sub>3</sub> A(60.0A)
Max continuous charging current	3.0C <sub>3</sub> A(540.0A)
Max continuous discharging current	3.0C <sub>3</sub> A(540.0A)
Max plus discharging current	5.0C <sub>3</sub> A(900.0A)<10s
Internal resistance	≤0.8mΩ(AC Impedance, 1 000 Hz)
Shipment voltage	3.2~3.4V
Appearance	Without break, scratch, distortion, pocking, leakage and so on.

**Fig.1: Cell dimension****6. Technical request****6.1 Cell Working Temperature**Charging temperature:  $0^{\circ}\text{C} \sim 70^{\circ}\text{C}$ Discharging temperature:  $-20^{\circ}\text{C} \sim 70^{\circ}\text{C}$ **6.2 Cell Test Conditions**

Unless otherwise specified, all test should be under the following conditions:

Temperature:  $20 \pm 3^{\circ}\text{C}$ Relative Humidity:  $65 \pm 20\% \text{RH}$ Atmospheric pressure:  $86\text{kPa} \sim 106\text{kPa}$ **6.3 Requirement of The Testing Equipment**

Voltage meter: Internal resistance of the voltage tester is  $\geq 10\text{ K}\Omega/\text{V}$ .

Temperature meter: The precision is  $\geq 0.5^\circ\text{C}$ .

## 6.4 Electrochemistry Performance

No.	Items	Criterion	Testing method	Remark				
1	Discharging performance at high and low temperature	<table border="1"> <tr> <td>-20°C</td> <td>Time of discharge at -20°C should not less than 126 minutes.</td> </tr> <tr> <td>55°C</td> <td>Time of discharge at 55°C should not less than 171 minutes.</td> </tr> </table>	-20°C	Time of discharge at -20°C should not less than 126 minutes.	55°C	Time of discharge at 55°C should not less than 171 minutes.	<ul style="list-style-type: none"> <li>Cell shall be charged following the standard charging method. And then standby for 20 hours at -20°C followed by a discharge at 1/3C<sub>3</sub>A(60.0A) to 2.8V at this temperature.</li> <li>Then cell shall allowed to rise to room temperature for one hour, followed by standard charging, and then standby for 5 hours at 55°C followed by a discharge at 1/3C<sub>3</sub>A(60.0A) to 2.8V at this temperature.</li> <li>The discharge times and capacity at different temperatures shall be recorded.</li> </ul>	
-20°C	Time of discharge at -20°C should not less than 126 minutes.							
55°C	Time of discharge at 55°C should not less than 171 minutes.							
2	RT Cycle	After 2000 cycles, the residual capacity/original discharge capacity $\geq 80\%$ .	The cell is tested at 20±3°C, 65±20% relative humidity and 86kPa~106kpa. First fully charge the cell with standard charging method, then discharge the cell with standard discharging method, the time interval between charging and discharging should not less than 30mins, then repeat the steps mentioned above.					
3	RT Charge retention	Standby at RT for 28days, discharge capacity should not less than 95% of the origin discharged capacity.	The capacity of the cell is tested by fully charged and discharged with standard method. Charging the cell with standard charging method, then stored with open- circuit at RT for 28days, discharged the cell with standard discharging method.					
4	RT Charge recovery	Discharge capacity should not less than 97% of the origin discharge capacity.	The cell which had been through charge retention test is to be fully charged with standard charging method, then discharge the cell standard discharging method.					
5	55°C Charge retention	Standby at 55°C for 7days, discharge capacity should not less than 90% of the origin discharged capacity.	The capacity of the cell is tested by fully charged and discharged with standard method. Charging the cell with standard charging method, then stored with open- circuit at 55°C for 7days, discharged the cell with standard discharging method.					
6	55°C Charge recovery	Discharge	The cell which had been through charge retention test is to					



## Product specification

DOC NO.: R100-QSI-008  
 REV. : A/00  
 SHEET : - 7 - of 9

		capacity should not less than 95% of the origin discharge capacity.	be fully charged with standard charging method, then discharge the cell standard discharging method.
7	Rate performance	The discharge capacity at 3.0C <sub>3</sub> A(540.0A) should be ≥85%, the discharge time should not less than 17mintues.	The capacity of the cell is tested by fully charged and discharged with standard method. Charging the cell with standard charging method, then discharge the cell with 3.0C <sub>3</sub> A(540.0A) constant current to 2.8V.

### 6.5 Environmental Characteristics

NO.	Item	Criterion	Testing method
1	Vibration	No leakage, no fire and no explosion.	After standard fully charge, standby the cell for 4hours,and measure the voltage and impedance ,then the cell is to be subjected to simple motion with an amplitude of 3.6mm, the frequency is 16.7hertz, and return in 90min.
2	Temperature impact test	No leakage, no fire and no explosion.	The cell is fully charged with standard charging method, and then it is to be stored for four hour at a test temperature equal to -20 °C, followed by a storage for four hour at a test temperature equal to 75°C, the maximum time interval between test temperature extremes is 30s, this procedure is to be repeated for 4 times, after which all test cells are to be stored for 6 hours at ambient temperature (20±3 °C).
3	Low pressure test	The samples shall not explode or catch fire, or leak.	The fully charged cell is to be stored for 6 hours at an absolute pressure of 11.6Kpa and a temperature of 20±3°C.
4	130°C storage	The samples shall not catch fire and explode.	The fully charged cell is to be heated in gravity convection or circulating air oven, the temperature of the oven is to be raised at a rate of 5±2°C per minute to a temperature of 130±2°C and remain for 10 minutes at that temperature before the test is discontinued.
5	Constant temperature and constant humidity test	The samples shall not leak, smoke, explode. Retention capacity≥80%.	The cell is fully charged with standard charging method, the cell is to be stored for 24 hours in an oven with a constant temperature of 40±2°C and a relative humidity of 90~95%, after testing the cell should be stored for 2hours at a temperature of 20±3°C, 65±20% relative humidity and a pressure of 86kPa~106kpa.

### 6.6 Safety Characteristics

NO.	Item	Criterion	Testing method
-----	------	-----------	----------------

## 6.2.3 Sinopoly MSDS

MSDS No.: SP-20140601 Creation Date: 1 June, 2014



### MATERIAL SAFETY DATA SHEET

PRODUCT NAME: LITHIUM-ION BATTERY

Model: SP-LFP40AHA, SP-LFP60AHA(A), SP-LFP66AHA, SP-LFP90AHA, SP-LFP100AHA, SP-LFP180AHA, SP-LFP200AHA, SP-LFP300AHA, SP-LFP400AHA, SP-LFP500AHA, SP-LFP700AHA, SP-LFP1000AHA

#### 1 - IDENTIFICATION OF THE SUBSTANCE/PREPARATION AND THE COMPANY /UNDERTAKING

Identification of the substance/preparation

Product name: Lithium-Ion Battery

Use of the substance/Preparation: Battery

Company/Undertaking identification

Supplier:

Name: Jinlin Sinopoly New Energy Tech.Co., LTD.

Address: Youyi Industrial District, Jinlin Liaoyuan Economic Development Area.

Phone: + 86-437-5018328 Fax: +86-437-5018321

#### 2 – COMPOSITION/INFORMATION ON INGREDIENTS

BATTERY MODEL: SP-LFP			
Ingredient	Weight %	CAS No.	Notes
Rare earth Mo	12%	7439-98-7	----
Li <sub>2</sub> CO <sub>3</sub>	16%	554-13-2	----
Mn <sup>2+</sup>	4.4%	7439-96-5	----
Graphite	15%	7782-42-5	----
Na <sup>+</sup>	1.5%	7440-23-5	----
C	3.1%	7440-44-0	----
Fe <sup>2+</sup>	13.4%	7439-89-6	----
PE	3.3%	9002-88-4	----
Cu	15%	7440-50-8	----
Al	11.5%	7429-90-5	----
HF	1.5%	7782-41-4	----
Sr <sup>2+</sup>	3.3%	7440-24-6	----

Page 1 , total 6 pages

**3 – HAZARDS IDENTIFICATION:****3.1 Physical:**

The Lithium-Ion rechargeable batteries described in this Material Safety Data Sheet are sealed units which are not hazardous when used according to the recommendations of the manufacturer.

Under normal conditions of use, the solid electrode materials and liquid electrolyte they contain are non-reactive provided the battery integrity is maintained and seals remain intact. There is Risk of fire only in cases of abuse (mechanical, thermal, electrical), which leads to the activation of the safety valve and/or the rupture of the battery container. Electrolyte leakage, electrode materials reaction with moisture/water or battery vent/fire may follow, depending upon the circumstances.

In case of excessive internal pressure and/or temperature Sinopoly Battery batteries are fitted with a safety vent for protection and/or rupture of the cell case.

**3.2 Chemical**

Classification of dangerous substances contained into the product as per directive 67/548/EEC

CAS NO	Chemical Symbol	Melting point	Boiling point	Classification			Safety advices (2)
				Exposure limit	Indication of danger	Special risk (1)	
12190-79-3	LiFePO4	> 1000 °C	N/A			R 22 R 43	S2 S22 S24 S26 S36 S37 S43 S45
EC: 96-49-1 DMC: 616-38-6 DEC: 105-58-8 EA: 141-78-6	Organic solvents (DC-DMC DEC-EA)	EC: 38 °C DMC: 4 °C DEC: -43 °C EA: -84 °C	EC: 243 °C DMC: 90 °C DEC: 127 °C EA: 77 °C	None established OSHA	Flammable	R21 R22 R41 R42/43	S2 S24 S26 S36 S37 S45
21324-40-3	LiPF 6	N/A (decomposes at 160 °C)	N/A	None established OSHA		R14 R21 R22 R41 R43	S2 S8 S22 S24 S26 S36 S37 S45

**3.2.1 – Nature of Special risks:**

R14 Reacts with water.

R 21 Harmful in contact with skin.

R22 Harmful if swallowed.

R41 Risk of serious damage to the eye.

R42/43 May cause sensitization by inhalation and skin contact.

R43 May cause sensitization by skin contact.

**3.2.2 – Safety advices:**

S 2 Keep out of reach from children.

S 8 Keep away from moisture.

S 22 Do not breathe dust.

S 24 Avoid contact with skin.


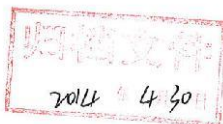
S26 In case of contact with eyes, rinse immediately with plenty of water and seek medical attention.

S36 Wear suitable gloves.

S45 In case of incident, seek medical attention



## 6.2.4 Calb cell datasheet

 <p>中航锂电(洛阳)有限公司 CHINA AVIATION LITHIUM BATTERY (LUOYANG) CO., LTD.</p>	<p>产品规格书 Specification</p>	<p>版本号 Version Number: D/0 发行日期 Issue Date: 2014-5-1</p>
<h1>产品规格书 Product Specification</h1> <p>方形锂离子电池 Prismatic lithium Ion Battery</p> <p>型号: CA180F I Model: CA180F I</p> <p>中航锂电(洛阳)有限公司 China Aviation Lithium Battery (Luoyang) Co., Ltd.</p> 		

1. 适用范围 Scope

本产品规格书描述了中航锂电生产的 CA180F I 可充电磷酸铁锂电池的产品性能指标、技术要求及安全注意事项。

This specification covers the performance indexes, technical requirements and safety issue of the CA180F I rechargeable lithium iron phosphate cell manufactured by CALB.

2. 产品类型 Product Type

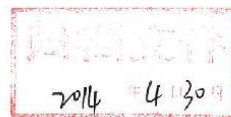
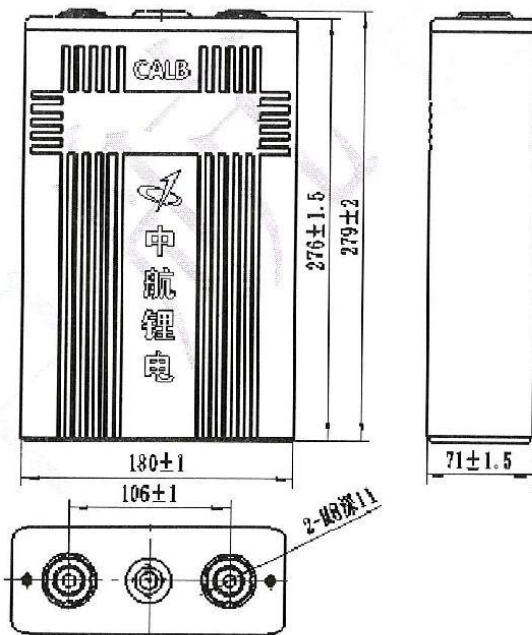
2.1 产品名称: 磷酸铁锂电池

Product Name: Lithium iron phosphate cell

2.2 型号规格: CA180F I

Specification: CA180F I

3. 单体电池尺寸 Cell Dimensions





# 产品规格书 Specification

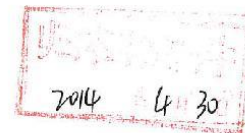
项目 Items	描述 Description	尺寸 (mm) Dimensions (mm)
L	长度 Length	180 ± 1
W	宽度 Width	71 ± 1.5
H	高度 Height	279 ± 2

## 4. 产品性能 Product Performance

### 4.1 技术参数 Technical Parameters

序号 NO.	项目 Items	参数说明 Parameter	备注 Remarks
1	额定容量 Nominal Capacity	180Ah	标准放电 Standard Discharge
2	最小容量 Minimal Capacity	180Ah	标准放电 Standard Discharge
3	工作电压 Work Voltage	2.5~3.65V	
4	内阻 (Ac. 1kHz) Internal Resistance (Ac. 1kHz)	0.1~0.5mΩ	新电池、30%SOC Fresh Cell、30%SOC
5	充电时间 Charging Time	标准充电 Standard Charge	~4h  ~1h 参考值 Reference Value
		快速充电 Fast Charge	
6	推荐SOC使用窗口 Recommended SOC Window	SOC : 10%~90%	
7	工作温度 Operating Temperature	充电温度 Charging Temperature	0~45°C 参考第 4.2 节 Refer to section 4.2
		放电温度 Discharging Temperature	-20~55°C 参考第 4.4 节 Refer to section 4.4
8	电池重量 Weight	约5.6kg About 5.6kg	
9	壳体材料 Shell Material	塑料 Plastic	

### 4.2 充电模式 Charging Model



序号 NO.	参数 Parameter	规格 Values	备注 Remarks
4.2.1	标准充电模式 Standard Charging Model	室温下, 以54A恒流持续充电至单体电池电压3.65V, 然后在3.65V下恒压持续充电直至电流下限 $\leq 9\pm 0.9A$ At room temperature, charged to 3.65V at a constant current of 54A, and then, charged continuously with constant voltage of 3.65V until the current was not more than $9\pm 0.9A$ .	
4.2.2	标准充电温度 Standard Charging Temperature	25 $\pm$ 2 $^{\circ}C$	电池温度 Cell Temperature
4.2.3	绝对充电温度 Absolute Charging Temperature	0~45 $^{\circ}C$	无论电池处在何种充电模式, 一旦发现电池温度超过绝对充电温度范围, 即停止充电 No matter what the charging model is, once the temperature of the cell is above the absolute charging temperature, charging should be stopped.
4.2.4	绝对充电电压 Absolute Charging Voltage	最大3.8V Maximum 3.8V	无论电池处在何种充电模式包括脉冲充电状态, 一旦发现电池电压超过绝对充电电压范围, 即停止充电 No matter what the charging model is, including pulse charging, once the voltage of the cell is above the absolute charging voltage, charging should be stopped.

#### 4.2.5 不同温度下充电电流限制 Charging Current Limit at Different Temperature

电池温度范围 Cell temperature range	<0 $^{\circ}C$	0-5 $^{\circ}C$	5-10 $^{\circ}C$	10-45 $^{\circ}C$	>45 $^{\circ}C$
允许最大充电电流 Maximum charging current allowed	0C	0.1C	0.5C	1.0C	0C

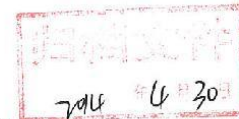
#### 4.3 允许最大脉冲充电电流 Maximum pulse charging current allowed

产品使用过程中, 再生制动过程的脉冲电流对电池具有充电效果。不同温度条件下的允许最大脉冲充电电流和持续时间必须严格遵守下表所列的所有充电状态以及电池温度等条件。违反下列充电条件可能会造成电池永久性的损坏并进而免除中航锂电的产品质量责任。

During the process of product being used, pulse current created in regenerative braking can recharge the battery. Maximum charging current allowed and the pulse duration in different temperature conditions must strictly observe the conditions listed in the following table. Violating the described conditions may cause permanent damage to the battery and thus is exempt from the responsibility of CALB for product quality.

不同 SOC 和温度条件下, 允许最大脉冲充电电流和持续时间如下表所示:

In different SOC and temperature conditions, the maximum values of charging current allowed and the pulse



duration are shown in the following table:

SOC	电池温度 Cell Temperature				
	≤-5℃	-5~0℃	0~10℃	10~23℃	23~50℃
>90%	不允许 Not allowed	不允许 Not allowed	不允许 Not allowed	1C/5s	1C/10s
>80%	不允许 Not allowed	不允许 Not allowed	1C/5s	1C/10s	1.5C/10s
>70%	不允许 Not allowed	1C/5s	1C/10s	1.5C/10s	2C/10s
≤70%	不允许 Not allowed	1C/10s	1.5C/10s	2C/10s	2C/10s

每次制动充电后, 电池需要有段休眠时期, 时间应等于或长于脉冲充电持续时间。休眠时期内, 电池可以处于放电状态, 也可以处于零电流不工作状态, 但在休眠时期内, 不允许电池再次发生制动充电现象。

After each brake charging, the battery needs to rest for certain time, which should be equal to or longer than the duration of the pulse charging. During the rest, the battery can be in the discharged state, or in a non-working state. But in the rest period, the battery is not allowed to pulse recharge again.

#### 4.4 放电模式 Discharging Model

归档文件  
2014 年 4 月 30 日

序号 NO.	参数 Parameter	产品规格 Specifications	备注 Remarks
4.4.1	标准放电模式 Standard Discharging Model	室温下, 以54A恒流持续放电至单体电池最小2.5V At room temperature, discharged to 2.5V at a constant current of 54A.	
4.4.2	最大持续放电电流 Maximum Constant Discharging Current	180A	
4.4.3	最大脉冲放电电流 (长脉冲) Maximum Pulse Discharging Current (Long Pulse)	360A	最长时间为3min Maximum duration: 3min
4.4.4	最大脉冲放电电流 (短脉冲) Maximum Pulse Discharging Current (Short Pulse)	540A	电池温度低于50℃, 且最长放电时间为10s When battery temperature is below 50℃, the maximum discharge can last 10s
4.4.5	标准放电温度 Standard Discharging Temperature	25±2℃	电池温度 Cell Temperature
4.4.6	绝对放电温度 Absolute Discharging Temperature	-20~55℃	无论电池处在何种放电模式, 一旦发现电池温度超过绝对放电温度范围



即停止放电

No matter what the discharging model is, once the temperature of the cell is above the absolute discharging temperature, discharging should be stopped.

## 4.5 电性能 Electrical Properties

### 4.5.1 测试条件 Test Conditions

除另有规定外，试验应在温度为： $25 \pm 5^\circ\text{C}$ ，相对湿度为：25%~85%，大气压力为：86KPa~106KPa 的环境中进行。

Unless otherwise specified, all the experiments should be carried out under ambient temperature:  $25 \pm 5^\circ\text{C}$ , relative humidity: 25%~85% and atmospheric pressure: 86KPa~106KPa.

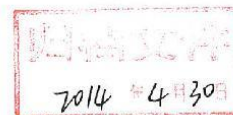
### 4.5.2 测量仪表与设备要求 Requirements of Measuring Instruments and Facilities

检验测试的所有仪表、设备（包括监控和监视试验参数的试验设备和仪器）应按国家有关计量检定规程或有关标准经检定或计量合格，并在有效期内。所有测试仪表、设备应具有足够的精度和稳定性，其精度应高于被测指标精度一个数量级或误差小于被测参数允许误差的二分之一。

All of the measuring instruments and facilities (include the equipments which monitor the test parameters) should be verified and calibrated qualified by relevant Chinese Calibration Regulation or certain standards within the valid date. All the test instruments and equipments should have adequate precision and stability and the precision should be an order higher than the tested indicators or the tolerance should be less than one third of the tested parameters.

### 4.5.3 性能指标 Performance Criterion

序号 NO.	项目 Items	技术要求 Technical Requirements	测试方法及步骤 Test Methods
1	外观 Appearance	电池应无破损、漏液、油污等缺陷，标识清楚。 No damage, leakage, oil contamination. Legibly marked.	目测法 Visual Inspection



附录 Appendix:

1. 单体电池常温放电典型曲线图

A typical curve of single cell discharged at room temperature.

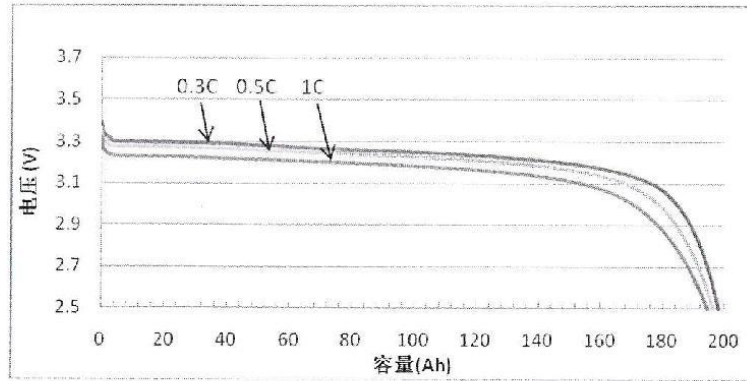


图 1. CA180F I 常温放电曲线

Graph1. Discharge curves of CA180F I at room temperature

2. 单体电池不同温度 0.3C 放电典型曲线图

A typical curve of single cell discharged with 0.3C at different temperature.

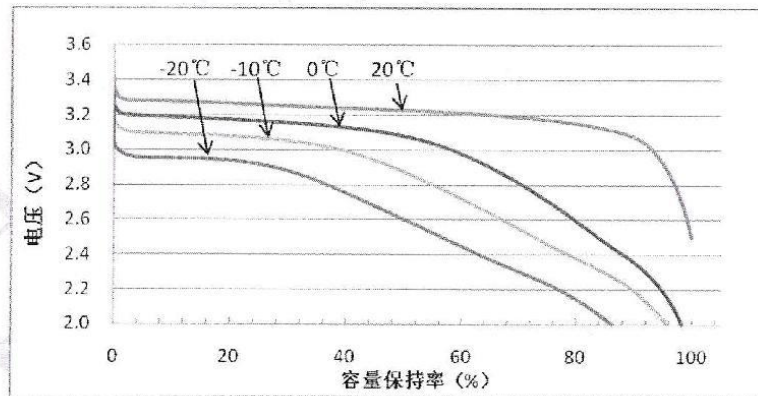


图 2. CA180F I 不同温度放电曲线

Graph2. Discharge curves of CA180F I at different temperatures

3. 单体电池立体效果图

3D effect picture of the cell

7046 04 30

## 6.2.5 Calb cell MSDS

14-DCNY-1

# PONY

Pony Testing International Group

Report No.: I03053011116D~1 Date: 03.31.2014 Page 1 of 10

## Material Safety Data Sheet

According to ISO11014:2009 & GB16483-2008

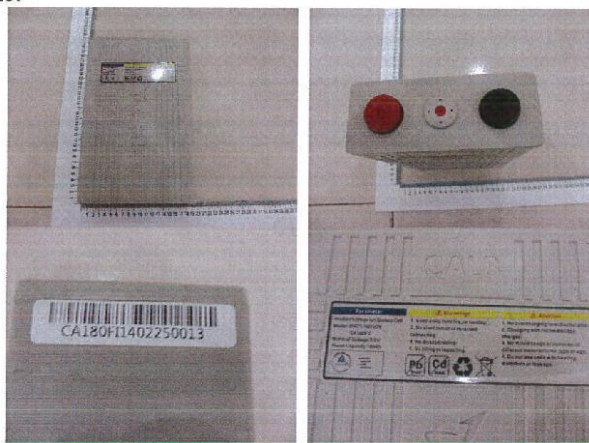
### Section 1 - Chemical Product and Company Identification

#### Chemical product identification

**Sample Description:** Lithium-ion Battery

**Sample Model:** CA180FI

**Sample Photo:**



Authenticate the photo on original report only

#### Company identification

**Manufacturer:** China Aviation Lithium Battery Co., Ltd.

**Address:** No.66, Binhe Road, High & New Tech Development Zone, Luoyang, Henan, China.

**Tel:** 0379-60697386

**Fax:** 0379-60697339

**Post code:** 471003

#### Further Information obtainable from

**Emergency telephone:** 0379-60697386

**E-mail:** zhaoyanyan@calb.cn

**PONY 谱尼测试**  
Pony Testing International Group

www.ponytest.com

Hotline 400-819-5688

Add: 北京市朝阳区苏州街19号  
与盈大厦

Tel: (010) 82618116

上海市徐汇区科平路66号  
35号楼4层

(021) 64851909

深圳市南山区创业路中兴  
工业城6栋1层

(0755) 26350996

青岛市城阳区株洲路100  
号6层

(0532) 88105866

Add: 天津市南开区红桥区藏宝  
大厦10层

Tel: (022) 27369750

宁波市高新区新明路150号  
二期1号楼1层

(0574) 87736499

广州市海珠区敦和路149号  
光铁科技园3号楼7层

(020) 89224310





Pony Testing International Group

Report No. : I03053011116D~1 Date: 03.31.2014 Page 3 of 10

Chemical Composition	CAS No.	EC#	Weight (%)
Lithium Iron Phosphate	15365-14-7	---	31
Graphite	7782-42-5	231-955-3	18
Copper	7440-50-8	231-159-6	12
Aluminum	7429-90-5	231-072-3	8
Lithium Hexafluorophosphate	21324-40-3	244-334-7	4
Carbonate	---	---	8
Polypropylene	9003-07-0	---	19

#### Section 4 - First Aid Measures

##### Description of first aid measures

**General information** No special measures required.

##### After eye contact

Flush eyes with plenty of water for several minutes while holding eyelids open. Get medical attention if irritation persists.

##### After skin contact

Remove contaminated clothing and shoes. Immediately wash with water and soap and rinse thoroughly. Wash clothing and shoes before reuse. If irritation occurs, get medical attention.

##### After inhalation

Remove victim to fresh area. Administer artificial respiration if breathing is difficult. Seek medical attention.

##### After swallowing

Do not induce vomiting. Get medical attention.

##### Information for doctor:

##### Indication of any immediate medical attention and special treatment needed

No further relevant information available.

#### Section 5 - Fire Fighting Measures

**Flammability:** Not available.

**Extinguishing media**

**Suitable extinguishing agents**

**PONY 谱尼测试**  
Pony Testing International Group

www.ponytest.com

Hotline 400-819-5688

Add: 北京市海淀区苏州街19号 与盈智大厦  
Tel: (010) 82518116

上海市松江区车亭公路880号  
35号楼11层  
Tel: (021) 61861999

深圳南山区创业路中兴  
工业城B栋1层  
Tel: (0755) 26050906

青岛市崂山区株洲路190  
号6层  
Tel: (0532) 93706866

Add: 天津市南开区红桥区福安  
大厦10层  
Tel: (022) 27360730

宁波市高新区新晖路150号  
二期1号楼4层  
Tel: (0574) 8736499

广州海珠区敦和路189号  
海珠科技园2号楼7层  
Tel: (020) 89224310

## 7 REFERENCES

---

1. UNFCCC. Secretariat. *Report of the Conference of the Parties on its twenty-first session, held in Paris from 30 November to 11 December 2015.: Part two: Action taken by the Conference of the Parties at its twenty-first session*. Decisions adopted by the Conference of the Parties, 2016. Available online: <https://unfccc.int/documents/9097> (accessed on 7 May 2024).
2. Intergovernmental Panel on Climate Change. *Global warming of 1.5 °C: Summary for Policymakers*, 2018. Available online: [https://www.ipcc.ch/site/assets/uploads/sites/2/2018/07/SR15\\_SPM\\_version\\_stand\\_alone\\_LR.pdf](https://www.ipcc.ch/site/assets/uploads/sites/2/2018/07/SR15_SPM_version_stand_alone_LR.pdf) (accessed on 7 May 2024).
3. Organisation for Economic Co-operation and Development. *How Green is Household Behaviour?: Sustainable Choices in a Time of Interlocking Crises*, Paris. Available online: [https://www.oecd-ilibrary.org/environment/how-green-is-household-behaviour\\_2bbbbb663-en](https://www.oecd-ilibrary.org/environment/how-green-is-household-behaviour_2bbbbb663-en) (accessed on 7 May 2024).
4. International Energy Agency. Solar PV power capacity in the Net Zero Scenario, 2015-2030. Available online: [www.iea.org/data-and-statistics/charts/solar-pv-power-capacity-in-the-net-zero-scenario-2015-2030](http://www.iea.org/data-and-statistics/charts/solar-pv-power-capacity-in-the-net-zero-scenario-2015-2030) (accessed on 7 May 2024).
5. Bloomberg Finance L.P. *Scaling the residential energy storage market*, 2023. Available online: <https://assets.bbhub.io/professional/sites/24/Scaling-the-Residential-Energy-Storage-Market.pdf> (accessed on 7 May 2024).
6. Figgner, J.; Hecht, C.; Haberschusz, D.; Bors, J.; Spreuer, K.G.; Kairies, K.-P.; Stenzel, P.; Sauer, D.U. *The development of battery storage systems in Germany: A market review (status 2023)*, 2022. Available online: <http://arxiv.org/pdf/2203.06762v3> (accessed on 7 May 2024).
7. Kebede, A.A.; Kalogiannis, T.; van Mierlo, J.; Berecibar, M. A comprehensive review of stationary energy storage devices for large scale renewable energy sources grid integration. *Renew. Sustain. Energy Rev.* **2022**, *159*, 112213, doi:10.1016/j.rser.2022.112213.
8. Kairies, K.-P.; Figgner, J.; Haberschusz, D.; Wessels, O.; Tepe, B.; Sauer, D.U. Market and technology development of PV home storage systems in Germany. *J. Energy Storage* **2019**, *23*, 416–424, doi:10.1016/j.est.2019.02.023.
9. Figgner, J.; Stenzel, P.; Kairies, K.-P.; Linßen, J.; Haberschusz, D.; Wessels, O.; Angenendt, G.; Robinius, M.; Stolten, D.; Sauer, D.U. The development of stationary battery storage systems in Germany – A market review. *J. Energy Storage* **2020**, *29*, 101153, doi:10.1016/j.est.2019.101153.

10. Müller, M.; Viernstein, L.; Truong, C.N.; Eiting, A.; Hesse, H.C.; Witzmann, R.; Jossen, A. Evaluation of grid-level adaptability for stationary battery energy storage system applications in Europe. *J. Energy Storage* **2017**, *9*, 1–11, doi:10.1016/j.est.2016.11.005.
11. Hesse, H.; Schimpe, M.; Kucevic, D.; Jossen, A. Lithium-Ion Battery Storage for the Grid—A Review of Stationary Battery Storage System Design Tailored for Applications in Modern Power Grids. *Energies* **2017**, *10*, 2107, doi:10.3390/en10122107.
12. Ziegler, M.S.; Trancik, J.E. Re-examining rates of lithium-ion battery technology improvement and cost decline. *Energy & Environmental Science* **2021**, *14*, 1635–1651, doi:10.1039/d0ee02681f.
13. Zhang, W.-J. Structure and performance of LiFePO<sub>4</sub> cathode materials: A review. *J. Power Sources* **2011**, *196*, 2962–2970, doi:10.1016/j.jpowsour.2010.11.113.
14. Li, Z.; Zhang, D.; Yang, F. Developments of lithium-ion batteries and challenges of LiFePO<sub>4</sub> as one promising cathode material. *J Mater Sci* **2009**, *44*, 2435–2443, doi:10.1007/s10853-009-3316-z.
15. Hesse, H.; Martins, R.; Musilek, P.; Naumann, M.; Truong, C.; Jossen, A. Economic Optimization of Component Sizing for Residential Battery Storage Systems. *Energies* **2017**, *10*, 835, doi:10.3390/en10070835.
16. Ecker, M.; Nieto, N.; Käbitz, S.; Schmalstieg, J.; Blanke, H.; Warnecke, A.; Sauer, D.U. Calendar and cycle life study of Li(NiMnCo)O<sub>2</sub> -based 18650 lithium-ion batteries. *J. Power Sources* **2014**, *248*, 839–851, doi:10.1016/j.jpowsour.2013.09.143.
17. Omar, N.; Monem, M.A.; Firouz, Y.; Salminen, J.; Smekens, J.; Hegazy, O.; Gaulous, H.; Mulder, G.; Van den Bossche, P.; Coosemans, T.; et al. Lithium iron phosphate based battery – Assessment of the aging parameters and development of cycle life model. *Appl. Energy* **2014**, *113*, 1575–1585, doi:10.1016/j.apenergy.2013.09.003.
18. Sarasketa-Zabala, E.; Gandiaga, I.; Rodriguez-Martinez, L.M.; Villarreal, I. Calendar ageing analysis of a LiFePO<sub>4</sub>/graphite cell with dynamic model validations: Towards realistic lifetime predictions. *J. Power Sources* **2014**, *272*, 45–57, doi:10.1016/j.jpowsour.2014.08.051.
19. Wang, J.; Liu, P.; Hicks-Garner, J.; Sherman, E.; Soukiazian, S.; Verbrugge, M.; Tataria, H.; Musser, J.; Finamore, P. Cycle-life model for graphite-LiFePO<sub>4</sub> cells. *J. Power Sources* **2011**, *196*, 3942–3948, doi:10.1016/j.jpowsour.2010.11.134.
20. Fu, R.; Choe, S.-Y.; Agubra, V.; Fergus, J. Development of a physics-based degradation model for lithium ion polymer batteries considering side reactions. *J. Power Sources* **2015**, *278*, 506–521, doi:10.1016/j.jpowsour.2014.12.059.
21. Watanabe, S.; Kinoshita, M.; Nakura, K. Capacity fade of LiNi<sub>(1-x-y)</sub>Co<sub>x</sub>Al<sub>y</sub>O<sub>2</sub> cathode for lithium-ion batteries during accelerated calendar and cycle life test. I. Comparison

- analysis between  $\text{LiNi}_{(1-x-y)}\text{Co}_x\text{Al}_y\text{O}_2$  and  $\text{LiCoO}_2$  cathodes in cylindrical lithium-ion cells during long term storage test. *J. Power Sources* **2014**, *247*, 412–422, doi:10.1016/j.jpowsour.2013.08.079.
22. Leonardi, S.G.; Aloisio, D.; Brunaccini, G.; Stassi, A.; Ferraro, M.; Antonucci, V.; Sergi, F. Investigation on the ageing mechanism for a lithium-ion cell under accelerated tests: The case of primary frequency regulation service. *J. Energy Storage* **2021**, *41*, 102904, doi:10.1016/j.est.2021.102904.
  23. Abraham, D.P.; Reynolds, E.M.; Sammann, E.; Jansen, A.N.; Dees, D.W. Aging characteristics of high-power lithium-ion cells with  $\text{LiNi}_{0.8}\text{Co}_{0.15}\text{Al}_{0.05}\text{O}_2$  and  $\text{Li}_{4/3}\text{Ti}_{5/3}\text{O}_4$  electrodes. *Electrochim. Acta* **2005**, *51*, 502–510, doi:10.1016/j.electacta.2005.05.008.
  24. Palacín, M.R. Understanding ageing in Li-ion batteries: a chemical issue. *Chem. Soc. Rev.* **2018**, *47*, 4924–4933, doi:10.1039/c7cs00889a.
  25. Vetter, J.; Novák, P.; Wagner, M.R.; Veit, C.; Möller, K.-C.; Besenhard, J.O.; Winter, M.; Wohlfahrt-Mehrens, M.; Vogler, C.; Hammouche, A. Ageing mechanisms in lithium-ion batteries. *J. Power Sources* **2005**, *147*, 269–281, doi:10.1016/j.jpowsour.2005.01.006.
  26. Alipour, M.; Ziebert, C.; Conte, F.V.; Kizilel, R. A Review on Temperature-Dependent Electrochemical Properties, Aging, and Performance of Lithium-Ion Cells. *Batteries* **2020**, *6*, 35, doi:10.3390/batteries6030035.
  27. Kupper, C.; Weißhar, B.; Reißmann, S.; Bessler, W.G. End-of-Life Prediction of a Lithium-Ion Battery Cell Based on Mechanistic Aging Models of the Graphite Electrode. *J. Electrochem. Soc.* **2018**, *165*, A3468-A3480, doi:10.1149/2.0941814jes.
  28. Carelli, S.; Bessler, W.G. Prediction of Reversible Lithium Plating with a Pseudo-3D Lithium-Ion Battery Model. *J. Electrochem. Soc.* **2020**, *167*, 100515, doi:10.1149/1945-7111/ab95c8.
  29. Reniers, J.M.; Mulder, G.; Howey, D.A. Review and Performance Comparison of Mechanical-Chemical Degradation Models for Lithium-Ion Batteries. *J. Electrochem. Soc.* **2019**, *166*, A3189-A3200, doi:10.1149/2.0281914jes.
  30. Hoffmann, L.; Grathwol, J.-K.; Haselrieder, W.; Leithoff, R.; Jansen, T.; Dilger, K.; Dröder, K.; Kwade, A.; Kurrat, M. Capacity Distribution of Large Lithium-Ion Battery Pouch Cells in Context with Pilot Production Processes. *Energy Technol.* **2020**, *8*, 1900196, doi:10.1002/ente.201900196.
  31. Dubarry, M.; Liaw, B.Y.; Chen, M.-S.; Chyan, S.-S.; Han, K.-C.; Sie, W.-T.; Wu, S.-H. Identifying battery aging mechanisms in large format Li ion cells. *J. Power Sources* **2011**, *196*, 3420–3425, doi:10.1016/j.jpowsour.2010.07.029.
  32. Grandjean, T.; Barai, A.; Hosseinzadeh, E.; Guo, Y.; McGordon, A.; Marco, J. Large format lithium ion pouch cell full thermal characterisation for improved electric vehicle

- thermal management. *J. Power Sources* **2017**, *359*, 215–225, doi:10.1016/j.jpowsour.2017.05.016.
33. Theinglim, K.; Poramapojana, P. *Effect of Tab Cooling on Large-Format Lithium-Ion Pouch Cells: SAE Technical Paper 2019-01-2261*, 2019. Available online: <https://doi.org/10.4271/2019-01-2261> (accessed on 7 May 2024).
  34. Youssef, R.; He, J.; Akbarzadeh, M.; Jagemont, J.; Sutter, L.D.; Berecibar, M.; van Mierlo, J. Investigation of Thermal Behavior of Large Lithium-Ion Prismatic Cell in Natural Air Convection. In *9th International Conference on Renewable Energy Research and Application (ICRERA)*, Glasgow, United Kingdom, 27/09 - 30/09/2020; IEEE, 2020; pp 43–47, ISBN 978-1-7281-7369-6.
  35. Shi, W.; Hu, X.; Wang, J.; Jiang, J.; Zhang, Y.; Yip, T. Analysis of Thermal Aging Paths for Large-Format LiFePO<sub>4</sub>/Graphite Battery. *Electrochim. Acta* **2016**, *196*, 13–23, doi:10.1016/j.electacta.2016.02.161.
  36. Ouyang, M.; Feng, X.; Han, X.; Lu, L.; Li, Z.; He, X. A dynamic capacity degradation model and its applications considering varying load for a large format Li-ion battery. *Appl. Energy* **2016**, *165*, 48–59, doi:10.1016/j.apenergy.2015.12.063.
  37. Li, J.; Song, Y.L. Preparation and Performance of 100Ah Li-Ion Battery with LiFePO<sub>4</sub> as Cathode Material. *AMR* **2012**, *463-464*, 753–759, doi:10.4028/www.scientific.net/AMR.463-464.753.
  38. Bacci, M.L.; Cheli, F.; Sabbioni, E.; Tarsitano, D.; Vignati, M. Aging models for high capacity LiFePO<sub>4</sub> cells. In *2017 International Conference of Electrical and Electronic Technologies for Automotive*, Torino, Italy, 15/06 - 16/06/2017; IEEE, 15/2017; pp 1–6, ISBN 978-88-87237-26-9.
  39. Panchal, S.; Rashid, M.; Long, F.; Mathew, M.; Fraser, R.; Fowler, M. *Degradation Testing and Modeling of 200 Ah LiFePO<sub>4</sub> Battery: SAE Technical Paper 2018-01-0441*, 2018. Available online: <https://doi.org/10.4271/2018-01-0441> (accessed on 7 May 2024).
  40. Berecibar, M.; Garmendia, M.; Gandiaga, I.; Crego, J.; Villarreal, I. State of health estimation algorithm of LiFePO<sub>4</sub> battery packs based on differential voltage curves for battery management system application. *Energy* **2016**, *103*, 784–796, doi:10.1016/j.energy.2016.02.163.
  41. Mingant, R.; Bernard, J.; Sauvant-Moynot, V. Novel state-of-health diagnostic method for Li-ion battery in service. *Appl. Energy* **2016**, *183*, 390–398, doi:10.1016/j.apenergy.2016.08.118.
  42. Yagci, M.C.; Behmann, R.; Daubert, V.; Braun, J.A.; Velten, D.; Bessler, W.G. Electrical and Structural Characterization of Large-Format Lithium Iron Phosphate Cells Used in

- Home-Storage Systems. *Energy Technol.* **2021**, *9*, 2000911, doi:10.1002/ente.202000911.
43. Yagci, M.C.; Feldmann, T.; Bollin, E.; Schmidt, M.; Bessler, W.G. Aging Characteristics of Stationary Lithium-Ion Battery Systems with Serial and Parallel Cell Configurations. *Energies* **2022**, *15*, 3922, doi:10.3390/en15113922.
  44. Dubarry, M.; Truchot, C.; Liaw, B.Y. Synthesize battery degradation modes via a diagnostic and prognostic model. *J. Power Sources* **2012**, *219*, 204–216, doi:10.1016/j.jpowsour.2012.07.016.
  45. Dubarry, M.; Beck, D. Perspective on Mechanistic Modeling of Li-Ion Batteries. *Acc. Mater. Res.* **2022**, *3*, 843–853, doi:10.1021/accountsmr.2c00082.
  46. Pillot, C. The Rechargeable Battery Market and Main Trends 2018-2030. Available online: [https://rechargebatteries.org/wp-content/uploads/2019/02/Keynote\\_2\\_AVICENNE\\_Christophe-Pillot.pdf](https://rechargebatteries.org/wp-content/uploads/2019/02/Keynote_2_AVICENNE_Christophe-Pillot.pdf) (accessed on 7 May 2024).
  47. Goodenough, J.B. How we made the Li-ion rechargeable battery. *Nat Electron* **2018**, *1*, 204, doi:10.1038/s41928-018-0048-6.
  48. Scrosati, B.; Garche, J. Lithium batteries: Status, prospects and future. *J. Power Sources* **2010**, *195*, 2419–2430, doi:10.1016/j.jpowsour.2009.11.048.
  49. Tarascon, J.M.; Armand, M. Issues and challenges facing rechargeable lithium batteries. *Nature* **2001**, *414*, 359–367, doi:10.1038/35104644.
  50. Reddy, T. *Linden's Handbook of Batteries*, 4th Edition; McGraw-Hill Education: New York, USA, 2010, ISBN 9780071624190.
  51. Hannan, M.A.; Wali, S.B.; Ker, P.J.; Rahman, M.A.; Mansor, M.; Ramachandaramurthy, V.K.; Muttaqi, K.M.; Mahlia, T.; Dong, Z.Y. Battery energy-storage system: A review of technologies, optimization objectives, constraints, approaches, and outstanding issues. *Journal of Energy Storage* **2021**, *42*, 103023, doi:10.1016/j.est.2021.103023.
  52. U.S. Department of Energy, EERE. *Energy Storage Technology and Cost Characterization Report*, 2019. Available online: [https://www.energy.gov/sites/default/files/2019/07/f65/Storage%20Cost%20and%20Performance%20Characterization%20Report\\_Final.pdf](https://www.energy.gov/sites/default/files/2019/07/f65/Storage%20Cost%20and%20Performance%20Characterization%20Report_Final.pdf) (accessed on 7 May 2024).
  53. Dongol, D.; Feldmann, T.; Bollin, E. An Overview to the concept of Smart Coupling and Battery Management for Grid connected Photovoltaic System. *Journal of Electronic Science and Technology* **2015**, *13*, 367–372, doi:10.11989/JEST.1674-862X.505243.
  54. Wood Mackenzie. *Can LFP technology retain its battery market share?*, 2020. Available online: <https://www.woodmac.com/reports/power-markets-can-lfp-technology-retain-its-battery-market-share-428028/> (accessed on November 2023).

55. Nitta, N.; Wu, F.; Lee, J.T.; Yushin, G. Li-ion battery materials: Present and future. *Materials Today* **2015**, *18*, 252–264, doi:10.1016/j.mattod.2014.10.040.
56. Armand, M.; Axmann, P.; Bresser, D.; Copley, M.; Edström, K.; Ekberg, C.; Guyomard, D.; Lestriez, B.; Novák, P.; Petranikova, M.; et al. Lithium-ion batteries – Current state of the art and anticipated developments. *J. Power Sources* **2020**, *479*, 228708, doi:10.1016/j.jpowsour.2020.228708.
57. Mizushima, K.; Jones, P.; Wiseman, P.; Goodenough, J.  $\text{Li}_x\text{CoO}_2$  ( $0 < x \leq 1$ ): A new cathode material for batteries of high energy density. *Solid State Ionics* **1981**, *3-4*, 171–174, doi:10.1016/0167-2738(81)90077-1.
58. Padhi, A.K. Phospho-olivines as Positive-Electrode Materials for Rechargeable Lithium Batteries. *J. Electrochem. Soc.* **1997**, *144*, 1188–1194, doi:10.1149/1.1837571.
59. Lee, H.; Yanilmaz, M.; Toprakci, O.; Fu, K.; Zhang, X. A review of recent developments in membrane separators for rechargeable lithium-ion batteries. *Energy & Environmental Science* **2014**, *7*, 3857–3886, doi:10.1039/C4EE01432D.
60. Chueh, W.C.; El Gabaly, F.; Sugar, J.D.; Bartelt, N.C.; McDaniel, A.H.; Fenton, K.R.; Zavadil, K.R.; Tyliczszak, T.; Lai, W.; McCarty, K.F. Intercalation pathway in many-particle  $\text{LiFePO}_4$  electrode revealed by nanoscale state-of-charge mapping. *Nano Lett.* **2013**, *13*, 866–872, doi:10.1021/nl3031899.
61. Park, M.; Zhang, X.; Chung, M.; Less, G.B.; Sastry, A.M. A review of conduction phenomena in Li-ion batteries. *J. Power Sources* **2010**, *195*, 7904–7929, doi:10.1016/j.jpowsour.2010.06.060.
62. Delacourt, C.; Wurm, C.; Laffont, L.; Leriche, J.-B.; Masquelier, C. Electrochemical and electrical properties of Nb- and/or C-containing  $\text{LiFePO}_4$  composites. *Solid State Ionics* **2006**, *177*, 333–341, doi:10.1016/j.ssi.2005.11.003.
63. Andre, D.; Kim, S.-J.; Lamp, P.; Lux, S.F.; Maglia, F.; Paschos, O.; Stiaszny, B. Future generations of cathode materials: an automotive industry perspective. *J. Mater. Chem. A* **2015**, *3*, 6709–6732, doi:10.1039/C5TA00361J.
64. Hill, D.M. *McMicken Battery Energy Storage System Event Technical Analysis and Recommendations*, 2020. Available online: <https://coaching.typepad.com/files/mcmicken.pdf> (accessed on 7 May 2024).
65. Irfan, U. How Lithium Ion Batteries Grounded the Dreamliner. Available online: <https://www.scientificamerican.com/article/how-lithium-ion-batteries-grounded-the-dreamliner/> (accessed on 29 February 2024).
66. NBC5 Chicago. LA-to-Frankfurt Lufthansa Flight Diverted to O'Hare After Laptop Fire. Available online: <https://www.nbcchicago.com/news/local/la-to-frankfurt-lufthansa-flight-diverted-to-ohare-after-laptop-fire/3031117/> (accessed on 29 February 2024).

67. Van Campenhout, C.; Jaiswal, R. Ship carrying nearly 3,000 cars ablaze off Dutch coast, crew member dead. Available online: <https://www.reuters.com/world/europe/one-dead-cargo-ship-fire-electric-car-suspected-source-dutch-coastguard-2023-07-26/> (accessed on 29 February 2024).
68. Deutsche Welle. Samsung stops selling Galaxy Note 7. Available online: <https://www.dw.com/en/samsung-halts-sales-of-galaxy-note-7-on-battery-problems/a-19522280> (accessed on 29 February 2024).
69. Wang, Q.; Ping, P.; Zhao, X.; Chu, G.; Sun, J.; Chen, C. Thermal runaway caused fire and explosion of lithium ion battery. *J. Power Sources* **2012**, *208*, 210–224, doi:10.1016/j.jpowsour.2012.02.038.
70. Sun, G.; Sui, T.; Song, B.; Zheng, H.; Lu, L.; Korsunsky, A.M. On the fragmentation of active material secondary particles in lithium ion battery cathodes induced by charge cycling. *Extreme Mechanics Letters* **2016**, *9*, 449–458, doi:10.1016/j.eml.2016.03.018.
71. Wang, D.; Wu, X.; Wang, Z.; Chen, L. Cracking causing cyclic instability of LiFePO<sub>4</sub> cathode material. *J. Power Sources* **2005**, *140*, 125–128, doi:10.1016/j.jpowsour.2004.06.059.
72. Gabrisch, H.; Wilcox, J.; Doeff, M.M. TEM Study of Fracturing in Spherical and Plate-like LiFePO<sub>4</sub> Particles. *Electrochem. Solid-State Lett.* **2008**, *11*, A25, doi:10.1149/1.2826746.
73. Mukhopadhyay, A.; Sheldon, B.W. Deformation and stress in electrode materials for Li-ion batteries. *Prog. Mater. Sci.* **2014**, *63*, 58–116, doi:10.1016/j.pmatsci.2014.02.001.
74. Ren, D.; Xie, L.; Wang, L.; He, X. A practical approach to predict volume deformation of lithium-ion batteries from crystal structure changes of electrode materials. *Int J Energy Res* **2021**, *45*, 7732–7740, doi:10.1002/er.6355.
75. Zhang, Y.; Wang, C.-Y.; Tang, X. Cycling degradation of an automotive LiFePO<sub>4</sub> lithium-ion battery. *J. Power Sources* **2011**, *196*, 1513–1520, doi:10.1016/j.jpowsour.2010.08.070.
76. Liu, P.; Wang, J.; Hicks-Garner, J.; Sherman, E.; Soukiazian, S.; Verbrugge, M.; Tataria, H.; Musser, J.; Finamore, P. Aging Mechanisms of LiFePO<sub>4</sub> Batteries Deduced by Electrochemical and Structural Analyses. *J. Electrochem. Soc.* **2010**, *157*, A499, doi:10.1149/1.3294790.
77. Safari, M.; Delacourt, C. Modeling of a Commercial Graphite/LiFePO<sub>4</sub> Cell. *J. Electrochem. Soc.* **2011**, *158*, A562, doi:10.1149/1.3567007.
78. Grolleau, S.; Delaille, A.; Gualous, H.; Gyan, P.; Revel, R.; Bernard, J.; Redondo-Iglesias, E.; Peter, J. Calendar aging of commercial graphite/LiFePO<sub>4</sub> cell – Predicting capacity fade under time dependent storage conditions. *J. Power Sources* **2014**, *255*, 450–458, doi:10.1016/j.jpowsour.2013.11.098.



79. Lewerenz, M.; Münnix, J.; Schmalstieg, J.; Käbitz, S.; Knips, M.; Sauer, D.U. Systematic aging of commercial LiFePO<sub>4</sub>/Graphite cylindrical cells including a theory explaining rise of capacity during aging. *J. Power Sources* **2017**, *345*, 254–263, doi:10.1016/j.jpowsour.2017.01.133.
80. Kassem, M.; Bernard, J.; Revel, R.; Pélissier, S.; Duclaud, F.; Delacourt, C. Calendar aging of a graphite/LiFePO<sub>4</sub> cell. *J. Power Sources* **2012**, *208*, 296–305, doi:10.1016/j.jpowsour.2012.02.068.
81. Naumann, M.; Spingler, F.B.; Jossen, A. Analysis and modeling of cycle aging of a commercial LiFePO<sub>4</sub>/graphite cell. *J. Power Sources* **2020**, *451*, 227666, doi:10.1016/j.jpowsour.2019.227666.
82. Safari, M.; Delacourt, C. Aging of a Commercial Graphite/LiFePO<sub>4</sub> Cell. *J. Electrochem. Soc.* **2011**, *158*, A1123, doi:10.1149/1.3614529.
83. Amine, K.; Liu, J.; Belharouak, I. High-temperature storage and cycling of C-LiFePO<sub>4</sub>/graphite Li-ion cells. *Electrochemistry Communications* **2005**, *7*, 669–673, doi:10.1016/j.elecom.2005.04.018.
84. Tan, L.; Zhang, L.; Sun, Q.; Shen, M.; Qu, Q.; Zheng, H. Capacity loss induced by lithium deposition at graphite anode for LiFePO<sub>4</sub>/graphite cell cycling at different temperatures. *Electrochim. Acta* **2013**, *111*, 802–808, doi:10.1016/j.electacta.2013.08.074.
85. Dubarry, M.; Qin, N.; Brooker, P. Calendar aging of commercial Li-ion cells of different chemistries – A review. *Curr. Opin. Electrochem.* **2018**, *9*, 106–113, doi:10.1016/j.coelec.2018.05.023.
86. Groot, J.; Swierczynski, M.; Stan, A.I.; Kær, S.K. On the complex ageing characteristics of high-power LiFePO<sub>4</sub>/graphite battery cells cycled with high charge and discharge currents. *J. Power Sources* **2015**, *286*, 475–487, doi:10.1016/j.jpowsour.2015.04.001.
87. Wikner, E.; Thiringer, T. Extending Battery Lifetime by Avoiding High SOC. *Applied Sciences* **2018**, *8*, 1825, doi:10.3390/app8101825.
88. Dubarry, M.; Truchot, C.; Liaw, B.Y. Cell degradation in commercial LiFePO<sub>4</sub> cells with high-power and high-energy designs. *J. Power Sources* **2014**, *258*, 408–419, doi:10.1016/j.jpowsour.2014.02.052.
89. Birkl, C.R.; Roberts, M.R.; McTurk, E.; Bruce, P.G.; Howey, D.A. Degradation diagnostics for lithium ion cells. *J. Power Sources* **2017**, *341*, 373–386, doi:10.1016/j.jpowsour.2016.12.011.
90. Uddin, K.; Perera, S.; Widanage, W.; Somerville, L.; Marco, J. Characterising Lithium-Ion Battery Degradation through the Identification and Tracking of Electrochemical Battery Model Parameters. *Batteries* **2016**, *2*, 13, doi:10.3390/batteries2020013.

91. Fath, J.P.; Dragicevic, D.; Bittel, L.; Nuhic, A.; Sieg, J.; Hahn, S.; Alsheimer, L.; Spier, B.; Wetzel, T. Quantification of aging mechanisms and inhomogeneity in cycled lithium-ion cells by differential voltage analysis. *J. Energy Storage* **2019**, *25*, 100813, doi:10.1016/j.est.2019.100813.
92. Zhi, X.; Liang, G.; Wang, L.; Ou, X.; Zhang, J.; Cui, J. The cycling performance of LiFePO<sub>4</sub>/C cathode materials. *J. Power Sources* **2009**, *189*, 779–782, doi:10.1016/j.jpowsour.2008.07.082.
93. Sieg, J.; Storch, M.; Fath, J.; Nuhic, A.; Bandlow, J.; Spier, B.; Sauer, D.U. Local degradation and differential voltage analysis of aged lithium-ion pouch cells. *J. Energy Storage* **2020**, *30*, 101582, doi:10.1016/j.est.2020.101582.
94. Verma, P.; Maire, P.; Novák, P. A review of the features and analyses of the solid electrolyte interphase in Li-ion batteries. *Electrochim. Acta* **2010**, *55*, 6332–6341, doi:10.1016/j.electacta.2010.05.072.
95. Heiskanen, S.K.; Kim, J.; Lucht, B.L. Generation and Evolution of the Solid Electrolyte Interphase of Lithium-Ion Batteries. *Joule* **2019**, *3*, 2322–2333, doi:10.1016/j.joule.2019.08.018.
96. Bloom, I.; Cole, B.; Sohn, J.; Jones, S.; Polzin, E.; Battaglia, V.; Henriksen, G.; Motloch, C.; Richardson, R.; Unkelhaeuser, T.; et al. An accelerated calendar and cycle life study of Li-ion cells. *J. Power Sources* **2001**, *101*, 238–247, doi:10.1016/S0378-7753(01)00783-2.
97. Mayur, M.; Yagci, M.C.; Carelli, S.; Margulies, P.; Velten, D.; Bessler, W.G. Identification of stoichiometric and microstructural parameters of a lithium-ion cell with blend electrode. *Phys. Chem. Chem. Phys.* **2019**, *21*, 23672–23684, doi:10.1039/C9CP04262H.
98. Keil, P.; Jossen, A. Calendar Aging of NCA Lithium-Ion Batteries Investigated by Differential Voltage Analysis and Coulomb Tracking. *J. Electrochem. Soc.* **2017**, *164*, A6066–A6074, doi:10.1149/2.0091701jes.
99. Dreyer, W.; Jamnik, J.; Guhlke, C.; Huth, R.; Moškon, J.; Gaberšček, M. The thermodynamic origin of hysteresis in insertion batteries. *Nat Mater* **2010**, *9*, 448–453, doi:10.1038/nmat2730.
100. Shenzhen Sinopoly Battery Co., Ltd. *Product specification for 3.2V/180Ah Lithium-ion Rechargeable Cell SP-LFP180AhA*, China, 2014.
101. China Aviation Lithium Battery Co., Ltd. *CA 180FI Product Specification: Prismatic lithium Ion Battery*, China, 2014.
102. Chen, J.; Wang, X.; Ma, Z.; Shao, G. Effects of yttrium ion doping on electrochemical performance of LiFePO<sub>4</sub>/C cathodes for lithium-ion battery. *Ionics* **2015**, *21*, 2701–2708, doi:10.1007/s11581-015-1467-2.

103. Yagci, M.C.; Richter, O.; Behmann, R.; Bessler, W.G. Degradation modes of large-format stationary-storage LFP-based lithium-ion cells during cyclic and calendaric aging (in preparation) **2024**.
104. Farmann, A.; Sauer, D.U. A study on the dependency of the open-circuit voltage on temperature and actual aging state of lithium-ion batteries. *J. Power Sources* **2017**, *347*, 1–13, doi:10.1016/j.jpowsour.2017.01.098.
105. Ovejas, V.J.; Cuadras, A. Effects of cycling on lithium-ion battery hysteresis and overvoltage. *Sci. Rep.* **2019**, *9*, 14875, doi:10.1038/s41598-019-51474-5.
106. Roscher, M.A.; Bohlen, O.; Vetter, J. OCV Hysteresis in Li-Ion Batteries including Two-Phase Transition Materials. *International Journal of Electrochemistry* **2011**, *2011*, 1–6, doi:10.4061/2011/984320.
107. Daubert, V. Strukturelle und chemische Analyse der Komponenten von geöffneten Lithium-Ionen-Batteriezellen. Bachelor's Thesis; Offenburg University of Applied Sciences, Offenburg, Germany, 2020.
108. Behmann, R. Probenpräparation und mikroskopische Untersuchung von Elektrodenmaterialien von Lithium-Ionen-Batterien. Bachelor's Thesis; Offenburg University of Applied Sciences, Offenburg, Germany, 2020.
109. Dongol, D.; Feldmann, T.; Schmidt, M.; Bollin, E. A MPC Based Peak Shaving Application for a Household with Photovoltaic Battery System. *Smart Cities, Green Technologies and Intelligent Transport Systems. SMARTGREENS 2018, VEHITS 2018. Communications in Computer and Information Science* **2019**, *992*, 44–66, doi:10.1007/978-3-030-26633-2\_3.
110. Dongol, D.; Feldmann, T.; Schmidt, M.; Bollin, E. A model predictive control based peak shaving application of battery for a household with photovoltaic system in a rural distribution grid. *Sustainable Energy, Grids and Networks* **2018**, *16*, 1–13, doi:10.1016/j.segan.2018.05.001.
111. Richter, O. Determination of aging parameters of cycled lithium-ion battery cells by differential voltage analysis. Seminar paper; Offenburg University of Applied Sciences, Offenburg, Germany, 2022.
112. Verbrugge, M.; Baker, D.; Koch, B.; Xiao, X.; Gu, W. Thermodynamic Model for Substitutional Materials: Application to Lithiated Graphite, Spinel Manganese Oxide, Iron Phosphate, and Layered Nickel-Manganese-Cobalt Oxide. *J. Electrochem. Soc.* **2017**, *164*, E3243-E3253, doi:10.1149/2.0341708jes.
113. Viswanathan, V.V.; Choi, D.; Wang, D.; Xu, W.; Towne, S.; Williford, R.E.; Zhang, J.-G.; Liu, J.; Yang, Z. Effect of entropy change of lithium intercalation in cathodes and anodes on

- Li-ion battery thermal management. *J. Power Sources* **2010**, *195*, 3720–3729, doi:10.1016/j.jpowsour.2009.11.103.
114. Smekens, J.; Paulsen, J.; Yang, W.; Omar, N.; Deconinck, J.; Hubin, A.; van Mierlo, J. A Modified Multiphysics model for Lithium-Ion batteries with a  $\text{Li}_x\text{Ni}_{1/3}\text{Mn}_{1/3}\text{Co}_{1/3}\text{O}_2$  electrode. *Electrochim. Acta* **2015**, *174*, 615–624, doi:10.1016/j.electacta.2015.06.015.
115. Reynier, Y.; Yazami, R.; Fultz, B. The entropy and enthalpy of lithium intercalation into graphite. *J. Power Sources* **2003**, *119-121*, 850–855, doi:10.1016/S0378-7753(03)00285-4.
116. Atkins, P.W.; Paula, J. de. *Atkins' physical chemistry*, 8th ed.; W.H. Freeman: New York, 2006, ISBN 0-7167-8759-8.
117. Newman, J.; Thomas-Alyea, K.E. *Electrochemical Systems*, 3rd ed.; John Wiley & Sons: Hoboken, New Jersey, USA, 2004, ISBN 9780471477563.
118. Hall, F.; Touzri, J.; Wußler, S.; Buqa, H.; Bessler, W.G. Experimental investigation of the thermal and cycling behavior of a lithium titanate-based lithium-ion pouch cell. *J. Energy Storage* **2018**, *17*, 109–117, doi:10.1016/j.est.2018.02.012.
119. Hall, F.; Wußler, S.; Buqa, H.; Bessler, W.G. Asymmetry of Discharge/Charge Curves of Lithium-Ion Battery Intercalation Electrodes. *J. Phys. Chem. C* **2016**, *120*, 23407–23414, doi:10.1021/acs.jpcc.6b07949.
120. Bandhauer, T.M.; Garimella, S.; Fuller, T.F. A Critical Review of Thermal Issues in Lithium-Ion Batteries. *J. Electrochem. Soc.* **2011**, *158*, R1, doi:10.1149/1.3515880.
121. Fath, J.P.; Alsheimer, L.; Storch, M.; Stadler, J.; Bandlow, J.; Hahn, S.; Riedel, R.; Wetzels, T. The influence of the anode overhang effect on the capacity of lithium-ion cells – a 0D-modeling approach. *J. Energy Storage* **2020**, *29*, 101344, doi:10.1016/j.est.2020.101344.
122. Bewlay, S.L.; Konstantinov, K.; Wang, G.X.; Dou, S.X.; Liu, H.K. Conductivity improvements to spray-produced  $\text{LiFePO}_4$  by addition of a carbon source. *Materials Letters* **2004**, *58*, 1788–1791, doi:10.1016/j.matlet.2003.11.008.
123. Doyle, M.; Fuller, T.F.; Newman, J. Modeling of Galvanostatic Charge and Discharge of the Lithium/Polymer/Insertion Cell. *J. Electrochem. Soc.* **1993**, *140*, 1526–1533, doi:10.1149/1.2221597.
124. Carelli, S.; Quarti, M.; Yagci, M.C.; Bessler, W.G. Modeling and Experimental Validation of a High-Power Lithium-Ion Pouch Cell with LCO/NCA Blend Cathode. *J. Electrochem. Soc.* **2019**, *166*, A2990-A3003, doi:10.1149/2.0301913jes.
125. Seaman, A.; Dao, T.-S.; McPhee, J. A Survey of Mathematics-Based Equivalent-Circuit and Electrochemical Battery Models for Hybrid and Electric Vehicle Simulation. *J. Power Sources* **2014**, *256*, 410–423, doi:10.1016/j.jpowsour.2014.01.057.

126. Lin, Z.; Liu, T.; Ai, X.; Liang, C. Aligning academia and industry for unified battery performance metrics. *Nat Comms* **2018**, *9*, 5262, doi:10.1038/s41467-018-07599-8.
127. Haynes, W.M.; Lide, D.R.; Bruno, T.J. *CRC Handbook of Chemistry and Physics: A Ready-Reference Book of Chemical and Physical Data: 2013-2014*, 94th edition; CRC press: Boca Raton (Fla.), London, New York, 2013, ISBN 9781466571143.
128. Streltsov, V.A.; Belokoneva, E.L.; Tsirelson, V.G.; Hansen, N.K. Multipole analysis of the electron density in triphylite, LiFePO<sub>4</sub>, using X-ray diffraction data. *Acta Cryst.* **1993**, *49*, 147–153, doi:10.1107/S0108768192004701.
129. Weißhar, B.; Bessler, W.G. Model-based lifetime prediction of an LFP/graphite lithium-ion battery in a stationary photovoltaic battery system. *J. Energy Storage* **2017**, *14*, 179–191, doi:10.1016/j.est.2017.10.002.
130. Uddin, K.; Moore, A.D.; Barai, A.; Marco, J. The effects of high frequency current ripple on electric vehicle battery performance. *Appl. Energy* **2016**, *178*, 142–154, doi:10.1016/j.apenergy.2016.06.033.
131. Korth Pereira Ferraz, P.; Kowal, J. A Comparative Study on the Influence of DC/DC-Converter Induced High Frequency Current Ripple on Lithium-Ion Batteries. *Sustainability* **2019**, *11*, 6050, doi:10.3390/su11216050.
132. Breucker, S. de; Engelen, K.; D'hulst, R.; Driesen, J. Impact of current ripple on Li-ion battery ageing. *2013 World Electric Vehicle Symposium and Exhibition (EVS27)* **2013**, 1–9, doi:10.1109/EVS.2013.6914791.
133. Beh, H.Z.Z.; Covic, G.A.; Boys, J.T. Effects of pulse and DC charging on lithium iron phosphate (LiFePO<sub>4</sub>) batteries. *2013 IEEE Energy Conversion Congress and Exposition* **2013**, 315–320, doi:10.1109/ECCE.2013.6646717.
134. Bessman, A.; Soares, R.; Wallmark, O.; Svens, P.; Lindbergh, G. Aging effects of AC harmonics on lithium-ion cells. *J. Energy Storage* **2019**, *21*, 741–749, doi:10.1016/j.est.2018.12.016.
135. Steinstraeter, M.; Gandlgruber, J.; Everken, J.; Lienkamp, M. Influence of pulse width modulated auxiliary consumers on battery aging in electric vehicles. *J. Energy Storage* **2022**, *48*, 104009, doi:10.1016/j.est.2022.104009.
136. Attia, P.M.; Bills, A.; Brosa Planella, F.; Dechent, P.; dos Reis, G.; Dubarry, M.; Gasper, P.; Gilchrist, R.; Greenbank, S.; Howey, D.; et al. Review—“Knees” in Lithium-Ion Battery Aging Trajectories. *J. Electrochem. Soc.* **2022**, *169*, 60517, doi:10.1149/1945-7111/ac6d13.
137. Wang, J.; Liu, P.; Hicks-Garner, J.; Sherman, E.; Soukiazian, S.; Verbrugge, M.; Tataria, H.; Musser, J.; Finamore, P. Cycle-life model for graphite-LiFePO<sub>4</sub> cells. *J. Power Sources* **2011**, *196*, 3942–3948, doi:10.1016/j.jpowsour.2010.11.134.

138. Korthauer, R. *Lithium-Ion Batteries: Basics and Applications*; Springer Berlin Heidelberg: Berlin, Heidelberg, 2018, ISBN 978-3-662-53069-6.
139. Shenzhen Sinopoly Battery Co., Ltd. *SP-LFP180AhA Product Brochure*, 2014.
140. Shenzhen Sinopoly Battery Co., Ltd. *SP-LFP180AhA Material Safety Data Sheet*, 2014.
141. Pony Testing International Group. *Calb CA180FI MSDS Report*, China, 2014.

